



Libraries and Learning Services

University of Auckland Research Repository, ResearchSpace

Copyright Statement

The digital copy of this thesis is protected by the Copyright Act 1994 (New Zealand).

This thesis may be consulted by you, provided you comply with the provisions of the Act and the following conditions of use:

- Any use you make of these documents or images must be for research or private study purposes only, and you may not make them available to any other person.
- Authors control the copyright of their thesis. You will recognize the author's right to be identified as the author of this thesis, and due acknowledgement will be made to the author where appropriate.
- You will obtain the author's permission before publishing any material from their thesis.

General copyright and disclaimer

In addition to the above conditions, authors give their consent for the digital copy of their work to be used subject to the conditions specified on the [Library Thesis Consent Form](#) and [Deposit Licence](#).

AGE-RELATED MECHANICAL CHANGES TO THE LUNG: A MULTI-SCALE MODELLING APPROACH

Karthik Subramaniam

Supervised by
Professor Merryn H. Tawhai
Dr. Haribalan Kumar

A thesis submitted in fulfilment of the requirements for
the degree of Doctor of Philosophy in Bioengineering

Auckland Bioengineering Institute
The University of Auckland
2017

Co-Authorship Form

This form is to accompany the submission of any PhD that contains published or unpublished co-authored work. **Please include one copy of this form for each co-authored work.** Completed forms should be included in all copies of your thesis submitted for examination and library deposit (including digital deposit), following your thesis Acknowledgements. Co-authored works may be included in a thesis if the candidate has written all or the majority of the text and had their contribution confirmed by all co-authors as not less than 65%.

Please indicate the chapter/section/pages of this thesis that are extracted from a co-authored work and give the title and publication details or details of submission of the co-authored work.	
The dependence of multiple metrics of lung tissue density on age and BMI	
Submitted to Journal of Applied Physiology	
Nature of contribution by PhD candidate	Design, programming, statistical analysis, writing
Extent of contribution by PhD candidate (%)	90%

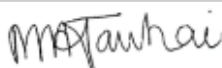
CO-AUTHORS

Name	Nature of Contribution
Dr. A Clark	Experimental design, supervision, analysis
Prof. E.A. Hoffman	Imaging, writing feedback
Prof. M.Tawhai	Experimental design, analysis, supervision

Certification by Co-Authors

The undersigned hereby certify that:

- ❖ the above statement correctly reflects the nature and extent of the PhD candidate's contribution to this work, and the nature of the contribution of each of the co-authors; and
- ❖ that the candidate wrote all or the majority of the text.

Name	Signature	Date
Dr. A Clark		20/08/2016
Prof. E.A. Hoffman		20/08/2016
Prof. M. Tawhai		20/08/2016

Co-Authorship Form

This form is to accompany the submission of any PhD that contains published or unpublished co-authored work. **Please include one copy of this form for each co-authored work.** Completed forms should be included in all copies of your thesis submitted for examination and library deposit (including digital deposit), following your thesis Acknowledgements. Co-authored works may be included in a thesis if the candidate has written all or the majority of the text and had their contribution confirmed by all co-authors as not less than 65%.

Please indicate the chapter/section/pages of this thesis that are extracted from a co-authored work and give the title and publication details or details of submission of the co-authored work.

Evidence for age-dependent air-space enlargement contributing to loss of lung tissue elastic recoil and increased shear modulus in older age
 Submitted to Journal of Applied Physiology

Nature of contribution by PhD candidate	Experimental design, modeling, writing
---	--

Extent of contribution by PhD candidate (%)	85%
---	-----

CO-AUTHORS

Name	Nature of Contribution
Dr. H. Kumar	Supervision, experimental design, simulation, writing
Prof. M. Tawhai	Supervising, analysis, writing

Certification by Co-Authors

The undersigned hereby certify that:

- ❖ the above statement correctly reflects the nature and extent of the PhD candidate's contribution to this work, and the nature of the contribution of each of the co-authors; and
- ❖ that the candidate wrote all or the majority of the text.

Name	Signature	Date
Dr. H. Kumar		20/08/2016
Prof. M. Tawhai		20/08/2016

Co-Authorship Form

This form is to accompany the submission of any PhD that contains published or unpublished co-authored work. **Please include one copy of this form for each co-authored work.** Completed forms should be included in all copies of your thesis submitted for examination and library deposit (including digital deposit), following your thesis Acknowledgements. Co-authored works may be included in a thesis if the candidate has written all or the majority of the text and had their contribution confirmed by all co-authors as not less than 65%.

Please indicate the chapter/section/pages of this thesis that are extracted from a co-authored work and give the title and publication details or details of submission of the co-authored work.	
The Impact of Age-Related Changes on Lung Mechanics: Linking Pressure-Volume and Parenchymal Properties to Tissue Deformation Submitted to Journal of Biomechanics and Modeling in Mechanobiology	
Nature of contribution by PhD candidate	Modeling, simulation, testing, writing
Extent of contribution by PhD candidate (%)	90%

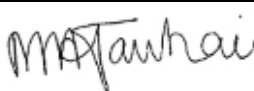
CO-AUTHORS

Name	Nature of Contribution
Dr. H Kumar	Supervision, simulation, analysis
Dr. A Clark	Supervision, analysis
Prof. E.A. Hoffman	Imaging
Prof. M. Tawhai	Supervision, writing

Certification by Co-Authors

The undersigned hereby certify that:

- ❖ the above statement correctly reflects the nature and extent of the PhD candidate's contribution to this work, and the nature of the contribution of each of the co-authors; and
- ❖ that the candidate wrote all or the majority of the text.

Name	Signature	Date
Dr. H. Kumar		20/08/2016
Dr. A Clark		20/08/2016
Prof. E.A.Hoffman		20/08/2016
Prof. M. Tawhai		20/08/2016

way for the universe to know itself. -- Carl Sagan.
The cosmos is within us. We are made of star-stuff.
We are

I would like to express my gratitude to Prof. Merryn Tawhai, Dr. Hari Kumar, and Dr. Alys Clark for their help and support during my PhD journey. I found my time at the Auckland Bio-engineering Institute enlightening and fulfilling, and this would not have been possible without their guidance and advice. I would also like to thank the members of the lung group – Dr. Kerry Hedges, Dr. Kelly Burrowes, Wendy Kang, Mahyar Osanlouy, Hamed Minaei, Dr. Barbara Breen, and Dr. Joshua Lee. In addition, I would like to thank my colleagues Dr. Mabelle Lin, Xiani Yan, Dr. Vicky Wang, Alex Wilson, Claas Seelhoff, and Dr. Prasad Babarenda Gamage for their valuable assistance and advice. Finally, I would like to thank my mum, dad, Aravind, Gowri, Snuffles, Snowball, my grandparents, and Ryoko for their love and support.

ABSTRACT

As a normal part of mature ageing lung tissue undergoes microstructural changes such as alveolar airspace enlargement, redistribution of collagen and elastin, a decrease in tissue elastic recoil, and an increase in interstitial fibrosis. Such changes, however, are also common early indicators of pulmonary disease. Old-age lungs are also expected to show a reduction in overall density, in addition to structural changes to alveoli and ducts. While these changes are common in pulmonary diseases such as emphysema, there is variation in how localised these phenomena are, and the mechanisms by which they occur, leading to heterogeneity in the pattern of degeneration of the parenchyma. Linking these age-related microstructural changes to mechanical changes at the whole-organ scale has proven difficult, and current understanding of the complex interactions between lung tissue structure and function is poor. This is largely due to the lung's behaviour on a whole-organ scale bearing little resemblance to its micromechanical behaviour.

To date, models of lung tissue mechanics have focused on the general case of the young healthy lung, and have yet to address the healthy ageing lung. Pulmonary function tests are commonly used to assess lung health, but are often unable to distinguish between early signs of pathology and normal age-related changes. Difficulty in distinguishing between early signs of pathology and normal ageing extends to imaging as well. Therefore, developing models that link microstructural changes to the mechanical behaviour of the ageing lung could be of great value in reducing misdiagnosis in the elderly, as well as improving and customising therapies

such as radiation treatment, where an understanding of the organ's mechanics is essential.

This thesis presents multi-scale biophysical models that can elucidate structure-function soft tissue mechanics relationships in the healthy young and old adult lung, and proposes methodologies to make models more 'subject-specific', with the aim that these frameworks aid in the development of clinical diagnostic tools. Biophysical models are developed to analyse the roles played by morphometric alveolar changes and the redistribution of load-bearing elements in duct/alveoli structures, both of which occur as a result of ageing. Heterogeneity in young and old lungs is studied using two different image analysis algorithms. Results show no significant difference in mean lung density (MLD) with respect to age at end expiration, however, at end inspiration the young cohort shows higher MLD. Gradients of tissue deformation along the gravitational axis show no significant difference between young and older cohorts. The two measurements of heterogeneity – fractal dimension and quadtree decomposition – show no correlation with age, however both metrics show strong correlations with body mass index (BMI). Alveolar-duct models are then used to address the effects of age-related alveolar morphometric changes and redistribution of collagen and elastin on elastic recoil and bulk modulus at a microstructural scale. Results support published data that suggest that airspace enlargement in old age contributes to loss of tissue elastic recoil. Results further show that redistribution of elastic proteins away from the alveolar duct walls to the septae can decrease tissue elastic recoil. Finally, a methodology for linking pulmonary function test pressure-volume data and tissue material test data to lung tissue mechanics is introduced. The effects of old age on soft-tissue deformation due to gravity are simulated using finite element models that are parameterised using this method.

SYMBOLS

L	Length	m, mm, μm
It	MDCT tube current-time product	mAs
BMI	Body mass index	kg/m^2
G	Shear modulus	
P	Pressure	Pa, cmH ₂ O
ρ	Density	g/cm^3
λ	Stretch ratio	
σ	Stress	Pa, cmH ₂ O

ABBREVIATIONS

FRC	Functional Residual Capacity
TLC	Total Lung Capacity
PFT	Pulmonary Function Test
COPD	Chronic Obstructive Pulmonary Disease
TV	Tidal Volume
VC	Vital Capacity
FVC	Forced Vital Capacity
FEV ₁	Forced Expiration Volume in 1 second
CT	Computed Tomography
MDCT	Multi-Detector Computed Tomography
BMI	Body Mass Index
V/Q	Ventilation-Perfusion Ratio
HRCT	High-Resolution Computed Tomography
MLD	Mean Lung Density
HU	Hounsfield Unit
FD	Fractal Dimension
QtD	Quadtree Decomposition
EE	End Expiration
EI	End Inspiration
ARDS	Acute Respiratory Distress Syndrome

CONTENTS

Symbols and Abbreviations	i
1. Introduction	1
1.1 The Ageing Lung	1
1.2 Age-Related Changes to Lung Parenchyma and Tissue Mechanics	2
1.3 The Impact of Obesity on the Lung	4
1.4 Clinical Methods to Examine the Lung	5
1.5 Computational Models of Lung Tissue Mechanics	8
1.6 Thesis Motivation	11
1.7 Thesis Summary	12
2. The Dependence of Multiple Metrics of Lung Tissue Density on Age and BMI	17
2.1 Introduction	17
2.2 Methods	19
2.2.1 Subject Data	19
2.2.2 Densitometry	23
2.2.3 Heterogeneity Analysis	24
2.3 Results	31
2.4 Discussion	44
2.4.1 Study Limitations	50
3. Evidence for Age-Dependent Air-Space Enlargement Contributing to Loss of Lung Tissue Elastic Recoil and Increased Shear Modulus in Older Age	51
3.1 Introduction	51

3.2 Methods	55
3.2.1 Model Geometries	55
3.2.2 Material Properties	59
3.2.3 Simulation of Material Deformation	61
3.3 Results	63
3.4 Discussion	73
3.4.1 Study Limitations	78
4. The Impact of Age-Related Changes on Lung Mechanics: Linking Pressure-Volume and Parenchymal Properties to Tissue Deformation	83
4.1 Introduction	83
4.2 Methods	85
4.2.1 Subject Data	85
4.2.2 Parameterization of the SEDF	88
4.2.3 Finite Element Models and Simulation	94
4.2.4 Sensitivity to Parameters	96
4.2.5 Grouping Analysis	98
4.3 Results	99
4.4 Discussion	108
4.4.1 Study Limitations	111
5. Conclusions and Future Work	113
References	117
Appendix A	
Appendix B	
Appendix C	

CHAPTER 1

INTRODUCTION

1.1 The Ageing Lung

During the 20th century human life expectancy increased at an unprecedented rate. In the United States the average human life expectancy rose from 47 years in 1900 to 77 in 2001 (6, 48). The proportion of the population over the age of 65 is expected to reach 20% by the year 2020 in the developed world (83). These dramatic changes in population demographics have had, and continue to have, a major impact on health care systems, both clinically and financially. In addition to accounting for a larger proportion of patients overall, older-age patients also generally require a longer recovery time in hospital. Thus, the basic physiological changes associated with ageing are of major clinical significance. It has also been observed that age-related changes to the functioning of the respiratory system can impair a patient's ability to recover from relatively common diseases, particularly those associated with the respiratory tract and heart failure (49, 50).

Several changes in structure and function are associated with the 'older' lung - alveolar ducts widen and alveoli tend to become more 'shallow' (72). These changes to the microstructural topology are likely to be related to changes in the distributions (rather than content) of elastin and collagen at the microstructural level (71, 109). There is also an associated loss of lung tissue elastic recoil which translates to increased static lung compliance, and an increase in the individual's functional

residual capacity (FRC, the air volume in the lung at the end of normal expiration) (63, 115). Decrease in the strength of respiratory muscles contributes to decreased driving pressure for expiratory airflow, and the loss of tissue elastic recoil means that airway closure can occur at much higher lung volumes than in young adults. In older age, the space between the vertebrae decreases and spinal curvature can increase, which affects the chest wall configuration and chest wall compliance. Together, these changes - which describe the average trajectory of the respiratory system during normal ageing - act in combination to alter the respiratory system mechanics and are most marked after the age of 50 (48, 49).

1.2 Age-Related Changes to Lung Parenchyma and Tissue Mechanics

In the human respiratory system it is difficult to distinguish between the changes that occur purely as a result of ageing and changes that are brought on by exposure to the environment, lifestyle, or even disease. The effects on the elderly caused by environmental factors such as air pollutants and cigarette smoke have been documented in a host of studies (3, 4, 47), however discriminating between these effects and the normal expected signs of ageing is difficult. Therefore, quantifying and modelling the impact of expected age-related changes in the lung could be hugely beneficial to clinical advances in the diagnosis of respiratory disease in older patients.

Experimental models using senescence accelerated mice (SAM) show a marked increase in alveolar duct size during ageing (112). This phenomenon is notably homogeneous throughout the lung. Also, cellular infiltrates in the alveoli are not present, suggesting the enlargement does not occur due to inflammation, as is the

case with emphysema (44). Verbeken et al. (72) note that alveolar dimensions do indeed change with age in humans (the ducts increasing in diameter and alveoli becoming shallower), and - consistent with studies in SAM - that this change is markedly homogeneous compared to the irregular distribution of enlarged airspaces and alveolar wall breakdown observed in the emphysematous lung. This implies that heterogeneity of lung parenchyma is an important factor in distinguishing between the healthy older lung and possible pathology. Kurozumi et al. (44) found that the ratio of lung weight to body weight does not change with age, and that a reduction in alveolar recoil pressure can be observed. The pressure-volume curve of the older lung shows a shift to the left and up (i.e. a loss of elastic recoil), similar to that observed in studies of senile hyperinflation.

Morphometric studies show decreasing airspace wall area per unit of lung volume with mature human ageing. This trend appears to start at the age of 30, and continues linearly throughout life, resulting in a 25% to 30% reduction in surface area by the age of 80-90 (57, 107). These changes in the ageing lung, when imaged, can be seen to differ from emphysema in that there is a lack of alveolar wall breakdown. However, it is interesting to note that they are both associated with similar changes to the mechanical properties of the lung tissue: mainly a loss of elastic recoil. Mercer and Crapo (71) and Toshima et al. (109) discuss in detail the distributions of collagen and elastin at a microstructural scale, and the role that protein fibres play in acting as stress-bearing components in alveoli.

In studying 20-60 year olds, Turner et al. (111) observed a reduction in static elastic recoil pressure of approximately 200 Pa (~ 2 cmH₂O) per decade from the age of 20 years, with the static pressure-volume curve shifting to the left and having a steeper

slope (80) with advancing age. Janssens et al. (49) and Niewoehner et al. (80) also report similar trends in age-related decline in tissue elastic recoil. It was suggested by Verbeken et al. (72, 73) that the changes in old-age parenchyma that were previously labelled 'senile emphysema' be classified differently from emphysema, due to the lack of alveolar wall breakdown and inflammation, and instead be termed 'senile lung'.

1.3 The Impact of Obesity on the Lung

Obesity is the most common metabolic disease worldwide, and its prevalence continues to increase (29, 59, 83). Obesity is defined as 'abnormal or excessive fat accumulation that may impair health' (83), and is often measured in terms of body mass index (BMI). A BMI of 20 – 24 kg/m² is considered healthy, and a BMI greater than 30 kg/m² is classified as obese. The associated increase in cardiovascular disease and diabetes with obesity creates a major economic burden for the health sector. Compared to the age-related conditions mentioned above there has been relatively little focus on the effect that obesity has on the respiratory system. However, its effects on pulmonary function and inflammation have been noted, and there is evidence to suggest that obesity increases the severity and morbidity of lung disease (69). Obesity has been linked to chronic obstructive pulmonary disease (COPD), asthma, obstructive sleep apnoea, pulmonary embolic disease, as well as aspiration pneumonia (69).

It has been suggested that an increase in body weight leads to overall degradation of pulmonary function (68, 110), particularly with respect to respiratory system mechanics. Studies have noted an inverse relationship between BMI and forced expiratory volume in one second (FEV₁) (10). This is significant, as FEV₁ is used as

a first-line test of general respiratory health, and a wide range of conditions cause abnormal FEV₁ results (41, 79, 91). These include cardiovascular disease, stroke, and lung cancer (17, 31). Studies of BMI correlation with lung function have also shown that subjects who lose weight tend to improve their respiratory performance (11), indicating that the reduction in respiratory mechanics efficiency is at least partially recoverable (77, 120).

It has been suggested that the negative effects of weight gain on lung function are more pronounced in men than in women, probably due to characteristic differences in fat distribution. In men, fat tends to accumulate in the abdomen, and this contributes to impaired mechanical performance of the diaphragm (13, 89). The increased abdominal fat can restrict the diaphragm's range of motion, and this restricted lung expansion can change pressure-volume characteristics. This can lead to increased airway closure and reduced ventilation in the peripheral alveoli, resulting in a deviation from ideal ventilation-perfusion (V/Q) matching and even arterial hypoxemia. These effects are particularly pronounced in the supine position, and therefore have important implications with regard to patients recovering in hospital and those on mechanical ventilation (14). Forced vital capacity (FVC) is reduced and the work of breathing is increased. This can lead to the need to increase ventilation, and thus panting (78, 108).

1.4 Clinical Methods to Examine the Lung

Pulmonary function tests (PFTs) provide a non-invasive means of assessing general lung health, and can be used to acquire information about lung capacity, flow rates, gas exchange, and pressure-volume characteristics. Typical quantities that are measured clinically include total lung capacity (TLC), functional residual capacity

(FRC), tidal volume (VT), vital capacity (VC), forced vital capacity (FVC), and forced expiratory volume in one second (FEV₁). Spirometry and plethysmography are two of the most common methods of lung function testing. Spirometry is the most commonly used technique for assessing lung function, and is particularly helpful in detecting airway obstruction. Initially, the subject's resting tidal volumes (i.e. normal breathing) are recorded. Following this, the subject is asked to inhale to maximum capacity, and then exhale completely, but in a passive manner. This test, known as unforced VC, can aid in detecting the presence of airway obstruction, and should last several seconds for normal adults. If there is significant airway obstruction, the exhalation period can be considerably longer. Forced VC is measured by asking the subject to inhale to maximum volume, then exhale forcefully for at least 6 seconds. In cases where significant obstruction is present the passive VC is likely to exceed the forced VC due to compression of the airways within the thorax when the forced expiration is performed. The volume exhaled after each second is also used as an important indicator in assessing lung health, and these are denoted FEV₁, FEV₃, and so on.

The technique of plethysmography uses Boyle's law which states that under isothermal conditions, for a closed container the pressure times the volume is constant (12, 16, 25, 121). Thus, the changes in thoracic volume that accompany inspiration or expiration can be acquired by measuring changes in a constant-volume chamber. It is also possible to use a constant-pressure plethysmograph, and measure the airflow in and out of a constant-pressure chamber. The subject sits in a box and breathes through a mouthpiece that is connected to a tube.

Changes in FEV₁ and FVC are expected as a consequence of normal ageing, however these changes can also indicate pathology. FEV₁ and FVC increase up to the age of approximately 20 in females and 27 in males. FEV₁ then declines at a rate of between 20 - 38 ml per annum (49). The ratio FEV₁/FVC is also used as an indicator of pulmonary health. This decreases from approximately 80% (or higher) in young adults to approximately 70% by the age of 70.

Normal age-related changes to gross lung structure have been well documented, however, the appearance and densitometry of lung tissue as seen in thoracic imaging of the normal older non-smoker have been described in relatively few studies. Using density as a measure Well et al. (117) showed a decrease in soft-tissue density between the ages of 20 and 70 of approximately 50 Hounsfield units (HU) or 0.05 g/cm³. Well et al. also noted that there was no statistically significant increase in mean lung volumes with increasing age for adult subjects (normalized mean lung volumes also did not show an increase with increasing age). Mean lung volumes were also noted to not change with increasing BMI. Copley et al. (18), in their study of mean lung density and 'complexity', also noted a lower mean lung density in older subjects (>75 years) compared to their younger cohort (<55 years).

The 'complexity' referred to by Copley et al. is similar to non-uniformity of parenchymal tissue, or heterogeneity, caused by destruction of alveolar walls. Increased heterogeneity is considered an indicator of many forms of pulmonary disease, therefore early detection of heterogeneity is of great interest. Such changes occur on a microscopic scale, and computerized methods are required for detection. Automated image-processing algorithms are increasingly being used on high resolution chest CT imaging for identifying lung pathology that has age-related

prevalence. Oelsner et al. (81) reported that emphysema is a common ‘incidental’ finding on CT occurring among smokers and non-smokers, and that the degree of emphysema as seen on CT can rarely be inferred by external respiratory airflow tests. Oelsner et al. found that emphysema on CT was associated with a significant increase in mortality due to respiratory diseases and lung cancer. They note that prior studies predominantly focus on smokers with 10 or more pack-years, a demographic that comprises only 30% of the older population. With declining rates of smoking, there is therefore a need to establish the expected degree of alveolar wall breakdown in the healthy older individual. Understanding and quantifying age-related (and lifestyle- and environment-related) differences between young and old patients who are non-smokers, and developing automated techniques for detecting abnormal image features, is becoming increasingly important for the early detection of pulmonary disease.

1.5 Computational Models of Lung Tissue Mechanics

Micromechanical analysis provides a tool by which changes to alveolar geometry and the redistribution of proteins can be understood. Such models have been employed previously to investigate various phenomena that are associated with pathological alveoli. For example, Gefen et al. (36) developed a model to compare stress distributions between normal and emphysematous parenchyma, while Chen et al. (15) used modelling to investigate stress in the alveolar walls that is caused by acute respiratory distress syndrome (ARDS). These studies focused only on the micro-scale, whereas Denny and Schroter used micromechanical models in several studies (21-24) to simulate general deformations and calculate elastic moduli for composites of alveoli, thereby demonstrating how microstructural simulation could be

used to link to larger scale continuum models. Suki and Bates (100) discussed the inevitability of lung mechanics models being highly complex and multi-scale by nature. They emphasised the necessity for alveolar models to combine the interactions of elastin, collagen, cells, and water, so that this combined behaviour can be translated to the whole lung as an emergent phenomenon. Suki and Bates highlight that changes in lung mechanics is a key common factor among a large number of pulmonary diseases. Through the use of spring network models they simulated alveolar wall breakdown similar to that seen in emphysema and compared their results to CT imaging. They concluded that if network links were eliminated based on the mechanical forces they carried (rather than purely randomly), the resultant pattern of parenchymal destruction closely matched that seen in emphysema.

Models of whole-lung mechanics (33, 61, 114) treat the lung tissue as a continuum, using a constitutive law to relate stress and strain. In the last 15 years predictive models of lung tissue mechanics have gained prominence particularly in the application of tumour motion tracking for radiation therapy (26, 70). In these models tissue deformation occurs in response to gravity or shape change. Tawhai et al. (104) used a finite element (FE) analysis to investigate deformation of lung soft tissue in human lungs with constant shape. Surface pressures and gravity-induced tissue deformation were simulated using their model, and the deformed tissue's resultant density distribution was validated through image analysis of thoracic CT imaging. Tawhai et al. reported a more uniform density distribution in the prone position as compared with the supine position. Their simulations of tissue deformation in the supine position compared well with supine tissue deformation as seen in CT imaging. Hyatt et al. (8) employed the FE method to investigate the effect

the placement and weight of the heart had on regional deformation of lung tissue in dogs. They concluded that the heart significantly contributed to altering regional tissue deformation of the lung, especially at higher lung inflation volumes. Both studies, those of Tawhai et al. and Hyatt et al., assumed lung inflation to be isotropic. In reality this is unlikely to be the case, however the degree of isotropy in lung expansion has yet to be defined conclusively, to the author's knowledge. Lee et al. (60) used FE analysis to examine the effect of the heart and interlobular fissures on regional behaviour of lung tissue. They concluded that in general the regional behaviour of the lung from the apex to the base was largely uniform.

Soft-tissue mechanical characteristics change as a normal part of ageing, as well as due to pathology e.g. fibrosis, nodules, and so on. Current models (including those discussed above) are limited in their ability to account for age-related or pathological changes to tissue properties. This is largely due to two factors: 1) the models treat lung parenchyma as a continuous homogeneous material, and 2) the lung models do not incorporate a mechanism by which the material representing lung parenchyma can readily be changed to reflect different material properties e.g. large changes in stiffness or shear modulus.

As the behaviour of these mechanics models is ultimately governed by their constitutive laws, the choice of constitutive equation and its parameterisation are key. While Denny and Schroter demonstrated how a connection from micro-scale analysis to a tissue material law could be made, to date there is no published constitutive law using this or similar methods that is data driven at the micro-scale and validated at the tissue or organ scale. The ability to simulate material behaviour in microstructural models and use these as inputs to whole-lung tissue mechanics

models would provide unique insight into the mechanisms by which changes at the alveolar level translate to alterations in whole lung function.

1.6 Thesis Motivation

Linking age-related changes in the lung's mechanical behaviour at a whole-organ scale to microscopic changes (i.e. changes in alveolar geometry and re-distribution of proteins) has proven difficult, and current understanding of the complex interactions between lung tissue structure and function is poor. This is largely due to the lung's behaviour on a whole-organ scale bearing little resemblance to its micromechanical behaviour (i.e. the interaction of individual proteins, fluids, collagen, elastin, and fibres). Through the use of micromechanical models this thesis seeks to highlight the roles played by morphometric changes and the redistribution of load-bearing elements in duct/alveoli structures, both of which occur as a result of ageing.

It has been suggested that most pulmonary diseases result in altered lung tissue mechanics (99, 100) via different mechanisms. The ageing lung also experiences changes to its mechanical behaviour as a normal part of healthy ageing. Pulmonary function tests, however, are often unable to distinguish between early signs of pathology and normal age-related changes. Therefore, developing models of the mechanical behaviour of the ageing lung could be of use in reducing misdiagnosis in the elderly, as well as improving and customising therapies such as radiation treatment, where an understanding of the organ's mechanics is essential. For these models to be more 'subject-specific' or 'demographic-specific' (in our case, with respect to age), it is necessary that the models' material properties be easily configured using real experimental data. To date, models of lung tissue mechanics have focused on the general case of the young healthy lung, and have yet to

address the healthy ageing lung. We elucidate the differences in externally-observed characteristics between young and old lungs, and identify how underlying material properties change with age to produce altered lung function.

Difficulty in distinguishing between early signs of pathology and normal ageing extends to imaging as well as to PFTs. Old-age lungs are expected to show a reduction in overall density, as well as structural changes to alveoli and ducts. While these changes are also common in pulmonary diseases (such as emphysema), there is variation in how localised these phenomena are, and the mechanisms by which they occur. This leads to differences in the pattern of degeneration of the parenchyma, a key metric of which is the heterogeneity of lung tissue density. Quantifying the expected heterogeneity in normal (young and old) lungs, and identifying how this metric changes with the onset of disease could be important for the early detection of pulmonary disease, before identification by the human eye (on radiological images) is possible. Statistical techniques have previously been used to investigate the heterogeneity of lung tissue, such as the coefficient of variation and fractal dimension. These metrics do provide a single-value measure of 'statistical variation', however they do not encode information regarding the spatial distribution of 'abnormalities', and the relative difference between the 'abnormality' and its surrounding 'normal' tissue. We employ a novel computational algorithm, used on lung CT for the first time, to create a metric of tissue heterogeneity that takes into account regional variations in tissue density.

1.7 Thesis Summary

This thesis presents a multi-scale approach to modelling the impact of mechanical changes that occur in the human lung as a result of ageing. Chapters 2-4 present a

series of model and image-based studies of lung tissue mechanics that comprise the bulk of the original research that was completed for this thesis. Material from each chapter has been submitted as a journal manuscript (abstracts from these are given in Appendix C).

Chapter 2 - 'The Dependence of Multiple Metrics of Lung Tissue Density on Age and BMI', using volumetric CT imaging, presents several techniques for image analysis and feature extraction that were developed for this thesis. For the first time, gender- and BMI- matched pairs of human subjects in two age cohorts were analysed for tissue density distributions and heterogeneity. The aim of this chapter was to use an objective quantitative assessment to determine whether never-smoking young and old subjects with no significant prior respiratory disease have differences in tissue density distribution and tissue heterogeneity in supine volumetric CT. In contrast to previous studies, no age-related differences in the lung tissue distribution were found. The same algorithms were then applied to determine differences based on subject BMI. The results show comparisons based on age and BMI, and highlight the effects that ageing and excessive body fat can have on indices for analysis of lung soft-tissue structure. The density distribution analysis also provides a vehicle for validating the full-lung mechanics model that is presented in subsequent chapters- subjects were imaged in the supine position, so the output of the lung mechanics model is directly comparable to the imaging. Appendix A contains two published conference papers that detail the methodology of the heterogeneity analysis used in the chapter. Material from this chapter has been submitted as a manuscript to the Journal of Applied Physiology as 'The dependence of multiple metrics of lung tissue density on age and BMI; K. Subramaniam, A. R. Clark, E.A Hoffman, M.H. Tawhai'. The manuscript has been provisionally accepted pending major revisions.

Chapter 3 – Evidence for Age-Dependent Air-Space Enlargement Contributing to Loss of Lung Tissue Elastic Recoil and Increased Shear Modulus in Older Age' presents configurable microstructural models of alveolar tissue, including alveoli and alveolar ducts. The aim of this study was to determine whether lung tissue-level stress-strain behaviour is sensitive to the geometric changes to the lung's microstructure that typically accompany ageing. In addition, non-uniformity in the distribution of the tissue's stress bearing components was also considered. This is the first study to apply a micro-mechanical analysis to understand age-dependent differences in soft tissue mechanics behaviour of the lung. Finite element models were constructed to represent the geometries of young- and old-age alveolar ducts surrounded by alveoli. Using these models, 'tissue block' pressure-volume characteristics and material behaviour were simulated. The results from this study highlight – for the first time - the differences in functional behaviour between young and old alveolar tissue due to age-related morphometric changes: that alveolar airspace enlargement can decrease the elastic recoil of the lung tissue, and that this can occur in the absence of any change to the elastic properties of the individual alveolar walls. This outcome is a novel finding that should stimulate discussion and new experiments to understand the mechanisms that contribute to loss of elastic recoil in the older lung. Material from this chapter has been submitted as a manuscript to the Journal of Applied Physiology as 'Evidence for age-dependent air-space enlargement contributing to loss of lung tissue elastic recoil and increased shear modulus in older age; K. Subramaniam, H. Kumar, M.H. Tawhai'. The manuscript has been provisionally accepted pending major revisions.

Chapter 4 - 'The Impact of Age-Related Changes on Lung Mechanics: Linking Pressure-Volume and Parenchymal Properties to Tissue Deformation' presents a

methodology that was developed for this thesis for parameterising the full-lung mechanics model, based on inputs from experimental data such as pressure-volume data (that can be readily acquired from pulmonary function tests (PFTs)) and shear modulus data (data that can be acquired from materials-testing experiments on excised or *in vivo* lung tissue). The aim of this study was to determine whether minimal information that is readily measurable from the intact lung can be used to parameterise a phenomenological model for the material behaviour of lung tissue, using a general optimisation process. This allows the lung mechanics model to be highly configurable, as the methodology presented in this chapter provides great flexibility and range in the types of experimental data that can be used as inputs. In this study, porcine pressure-volume data and pressure-dependent shear moduli acquired from experiments on excised human tissue were used as inputs into the optimisation method. Simulations of tissue inflation and gravitational deformation of a finite element model (using finite elasticity theory and the optimised material law) were then compared to volumetric CT imaging at multiple inflation pressures. Results showed that the implemented process provides good prediction of lung tissue deformation under gravity loading, and exploratory simulations suggest that the model can be configured for young- and old-age tissue mechanics simulation. Material from this chapter has been submitted to the Journal of Biomechanics and Modeling in Mechanobiology as 'The Impact of Age-Related Changes on Lung Mechanics: Linking Pressure-Volume and Parenchymal Properties to Tissue Deformation; K. Subramaniam, H. Kumar, A. Clark, E.A Hoffman, M.H. Tawhai'.

CHAPTER 2

THE DEPENDENCE OF MULTIPLE METRICS OF LUNG TISSUE DENSITY ON AGE AND BMI

2.1 Introduction

Understanding the normal radiological appearance of the older lung and its relationship to lung function is important for discriminating lung disease from normal senescence. During mature ageing the lung undergoes microstructural changes that affect its mechanical (30, 65, 119) and gas exchange function (73). This includes alveolar 'airspace enlargement' (57, 107), which reduces the gas exchange surface area and is associated with a loss of tissue elastic recoil (63, 72). This senescent microstructural remodelling differs from the pathologic destruction of the alveoli that defines pulmonary emphysema (44, 112) (a component of chronic obstructive pulmonary disease, COPD, which has age-related prevalence). While the normal age-related changes in gross lung structure on pathology and their functional consequences have been well documented, the computed tomography (CT) appearance and densitometry of lung tissue in the normal older non-smoker have been described in relatively few studies. Similarly, the effect of increased body weight on respiratory function has been studied (68, 69, 110), whereas the association between BMI and metrics of lung tissue density remains unclear. BMI has been reported to differ by approximately 2 kg/m^2 in young (20-30 years) and

older (>50 years) adults (32), therefore any comparison of lung appearance in these age groups should consider the potential contribution of BMI.

Automated quantitative methods are increasingly being used on high resolution chest computed tomography (CT) for identifying lung pathology. CT studies using a simple measure of the lung tissue - the mean lung density (MLD) - have suggested a decrease in MLD of approximately 50 HU (0.05 g/cm^3) between 20 and 70 years of age (117). This implies an increase in air volume, which may be the result of normal alveolar airspace enlargement (57, 107) or pathologic destruction of the alveolar walls. More detailed subjective assessments have suggested an increase in tissue and airway abnormalities in older age. Copley et al. (18) compared the presence and extent of CT features on prone imaging from subjects with no known respiratory disease, aged > 75 years and < 55 years. They noted limited predominantly subpleural basal reticular pattern in the majority of the older group but none in the younger group, and more frequent incidence of cysts, bronchial dilation and wall thickening in the older subjects. Similarly, Winter et al. (118) reported a higher prevalence of abnormal scans in subjects aged > 65 years in comparison to subjects aged < 50 years. They suggested that parenchymal bands, interlobular septal thickening and lung nodules may represent normal lung ageing. In a subgroup of never smokers from the Copley et al. (18) study, they found that the lung tissue of the younger cohort had a larger fractal dimension (FD) than the older subjects, suggesting an 'increased complexity' in lung tissue in comparison to the older group.

A limitation of previous studies is the reliance on imaging that is acquired as part of routine clinical diagnosis or screening. Clinical protocols do not explicitly control the lung volume during imaging; instead patients are instructed to maximally inhale or

exhale followed by a breath-hold. Inter-subject variability in lung volumes could introduce error into the comparison of lung densitometry between subject groups, potentially influencing study interpretation.

Age-related changes to the lung are most marked over the age of 50 years (48, 49). The main purpose of this chapter is to determine whether these changes to the lung manifest as quantifiable differences in metrics of lung tissue density in older (> 60 years) and younger (< 30 years) non-smoking adults who have normal lung function and no radiological abnormalities on CT. Based on prior studies of age related changes in lung parenchyma it was hypothesized that lung complexity would decrease with age. Both the older and younger cohorts in this study consist of subjects with a range of BMIs, so that the association between BMI and tissue density can be assessed. Several different metrics of lung tissue density are quantified, to assess mean tissue density, its distribution within the chest wall, and heterogeneity. The dependence of these metrics on both age and BMI are considered.

2.2 Methods

2.2.1 Subject Data

Imaging and pulmonary function test data were acquired retrospectively from the University of Iowa Comprehensive Lung Imaging Center. Subjects were selected from a previous study of healthy volunteers with normal lung function (under NIH Grants R01-HL-064368 and R01-EB-005823) (40, 64, 103). The University of Iowa Institutional Review Board and Radiation Safety Committees approved the study and subsequent use of the data, and all subjects gave informed consent. The data

comprised volumetric multi-detector row computed tomography (MDCT) imaging, pulmonary function tests (PFTs), and radiology reports. Imaging was acquired in the supine posture at end expiration (EE, volume-controlled at 55% vital capacity), and end inspiration (EI, at 80% vital capacity). MDCT scan parameters were 120 kV, 100 mAs, and a pitch of 1.2. Subject data was acquired during the years 2004-2011, and all data were acquired in the same centre under the same imaging protocols with regular scanning calibration. Each volumetric image set contained 500-800 images, with a distance between slices of 0.50 mm, and a reconstruction matrix of 512×512 pixels.

All subjects in the imaging study who were 60 years of age or older were considered for inclusion (33 subjects). Subjects were excluded on the basis of ever smoking, previous lung disease or lung injury, PFTs that did not meet American Thoracic Society (ATS) criteria for normal lung function (12, 121), or radiologist-identified parenchymal abnormalities. Two female subjects were excluded to maintain equal numbers of males and females (the females who were the closest match to the males were retained). The >60 years cohort in this study then comprised 4 male and 4 female subjects, with mean age 70.8 ± 9.2 years, and mean Body Mass Index (BMI) of 27.1 ± 4.4 kg/m² (range 21 – 32 kg/m²). A further 8 subjects aged 30 years or younger who met the same exclusion criteria were selected from the database, to gender and BMI-match the older cohort. The entire dataset consisted of several hundred subjects. Matching was done manually – the main reason for this was that only subjects with no abnormalities identified by a radiologist (on the chest CT) were chosen for analysis. For the older subjects this eliminated a large proportion of the subjects. The less than 30 years group were aged 24.5 ± 4.7 years, with mean BMI of 26.9 ± 3.9 kg/m². Table 2.1 summarizes the subject physiological data that are

relevant to the current study. Upright lung volumes (from plethysmography) were not significantly different between the groups ($p=0.497$ and 0.460 for FRC and TLC, respectively). FEV₁, FVC, and their ratio were all significantly smaller in the >60 years group compared with the <30 years group (see Table 2.1).

Table 2.1: Subject demographics, including lung air volumes and capacities measured using seated body box plethysmography. Values are given as means, with standard deviation in brackets. Significance for the paired t-test at the 5% level is indicated by *.

	Subjects aged < 30 years	Subjects aged > 60 years	p-value (paired t-test)
Age	24.5 (4.7)	70.8 (9.2)	
BMI	26.9 (4.2)	27.1 (4.7)	0.35
Functional residual capacity, FRC (L)	2.92 (0.90)	2.70 (0.69)	0.49
Total lung capacity, TLC (L)	6.44 (1.51)	6.11 (1.05)	0.46
Forced expired volume in 1 second, FEV₁ (L)	4.48 (1.54)	2.90 (0.83)	0.023*
Forced, vital capacity, FVC (L)	5.30 (1.49)	3.61 (0.98)	0.018*
FEV₁/FVC	0.83 (0.04)	0.80 (0.05)	0.25
FEV₁ % Predicted	116.98 (23.97)	123.18 (10.97)	0.51

The lungs, major airways, and blood vessels were automatically segmented from the volumetric imaging for each subject, using custom-written software (PASS: the Pulmonary Analysis Software Suite, University of Iowa (45)). All pre-processing of images was done as part of this study. Further image analysis was performed using MATLAB (version 2010a, The MathWorks Inc.). The segmented images were used to subtract 'non-tissue' structures from the raw images (large airways, large blood vessels). An erosion filter was then used to perform a 'peel' function on the resultant images. This operation was performed along the jagged boundary of the segmented lung parenchyma where any residual non-lung-tissue pixels were removed, effectively shrinking the region of interest by 2-3 pixels. The filter was applied to all of the images, along the craniocaudal axis. Figure 2.1 shows one slice of a volumetric CT image with its corresponding lung mask image.

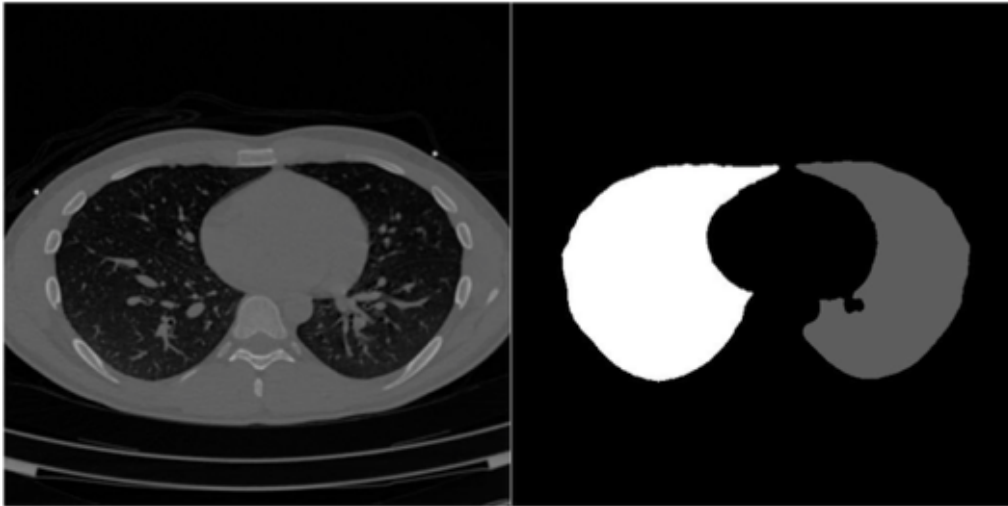


Figure 2.1: A volumetric CT image (left) and its corresponding mask image (right), generated using PASS. The CT image corresponds to a slice orthogonal to the craniocaudal axis. The mask image is used to isolate only the lung soft-tissue.

Supine EE and EI total lung volumes (V_{EE} and V_{EI} , respectively) were calculated from the reconstructed images (Table 2.2). The maximum distance along the mediolateral axis (total lung ‘width’) and the minimum distance along the craniocaudal axis (lung ‘height’) were measured directly on the images using caliper measurement tools in PASS.

2.2.2 Densitometry

The tissue density (ρ , in g/cm^3) was calculated from the Hounsfield Unit (HU) at each voxel using

$$\rho = \frac{HU}{1000} + 1 \quad (2.1)$$

ρ was evaluated at three different scales of interest: 1. at the whole organ level by its mean value for each age group; 2. by its spatial variation along the craniocaudal, mediolateral, and dorsoventral (i.e. gravitational) axes; and 3. by assessment of its heterogeneity.

The mean lung density (MLD) and its standard deviation were calculated for each subject using intensity values from every voxel within the filtered images (including all CT slices). To quantify the spatial distribution of ρ , a custom-written MATLAB program was used to calculate the mean $\rho \pm \text{SD}$ within 5 mm sections of tissue that were oriented perpendicular to the three axes.

2.2.3 Heterogeneity Analysis

Several methods exist for quantifying pulmonary heterogeneity, however the values reported are dependent on image resolution, and they do not take into account the spatial distribution of heterogeneity (9, 38). Heterogeneity in ρ was therefore quantified using two different methods: 1. the fractal dimension (FD) for ρ , calculated by fitting a straight line to the relationship between coefficient of variation (CoV) and sampling window size (9, 38); and 2. Quadtree Decomposition (QtD) (27, 67, 90, 95) which accounts for the spatial clustering of tissue with similar ρ .

The fractal dimension (FD) is calculated as 1 minus the gradient of the log-log plot of coefficient of variation (CoV) against sample window size. The CoV is a measure of the standard deviation (SD) relative to the mean of the intensities in an image, or sampling window. As such it directly quantifies the variability of ρ with respect to the MLD. The CoV can be calculated for any sized sampling window.

An alternative method for quantifying heterogeneity that has the potential to resolve issues with lack of spatial resolution in typical metrics of heterogeneity and their dependence on image resolution is Quadtree Decomposition (QtD). The QtD method reflects the spatial distribution of image intensities. The method has not previously been applied to lungs. The QtD is a commonly used algorithm in computer science and image processing, for applications such as data partitioning and texture analysis (90). The technique works in a 2-dimensional image-space by recursively partitioning an image into quadrants until all the pixels in each quadrant are considered similar, based on some comparison. The range of intensities within each quadrant is evaluated, and if the range is less than a user-defined threshold then the pixels in

the quadrant are considered homogeneous. The quadrant is considered to be heterogeneous if the range of pixels is greater than the user-defined threshold, and hence the quadrant is divided into four sub-quadrants. This process is performed recursively until the image has been reduced to the minimum number of homogeneous quadrants. Figure 2.2 shows a masked lung CT image along with the resultant image after applying the QtD algorithm.

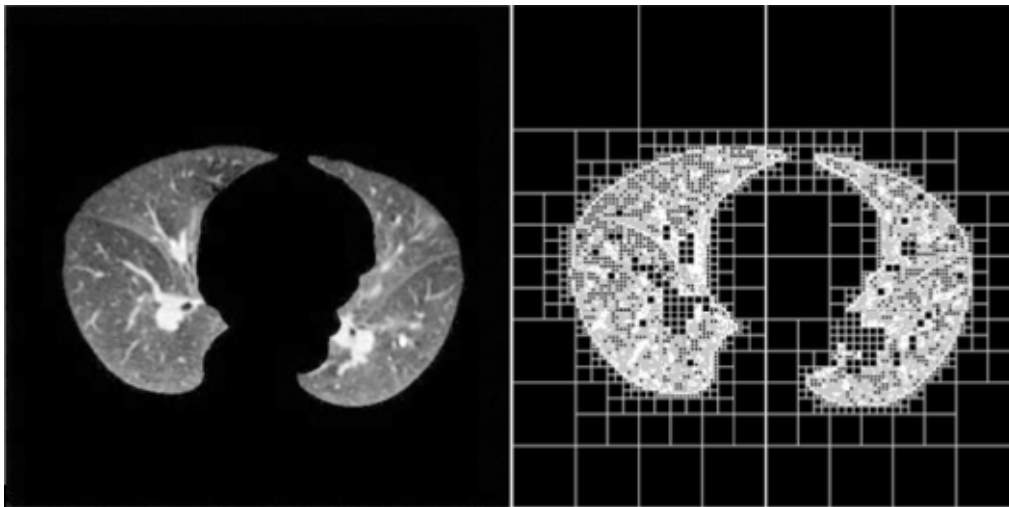


Figure 2.2: A masked lung CT image (left) and its resultant QtD image (right). The image on the left is achieved by applying the mask from Figure 2.1. The QtD image illustrates how boxes reduce in size in regions of increased tissue complexity (increased heterogeneity).

To demonstrate the advantages of the QtD algorithm, consider the example images shown in Figure 2.3. The proportion of grey to black is the same in both images, but divided into different sized squares. The CoV is identical for the two images (when taking the region of interest to be the entire image), however the QtD method gives different heterogeneity values as a greater number of sub-quadrants are required for the right-hand-side image.

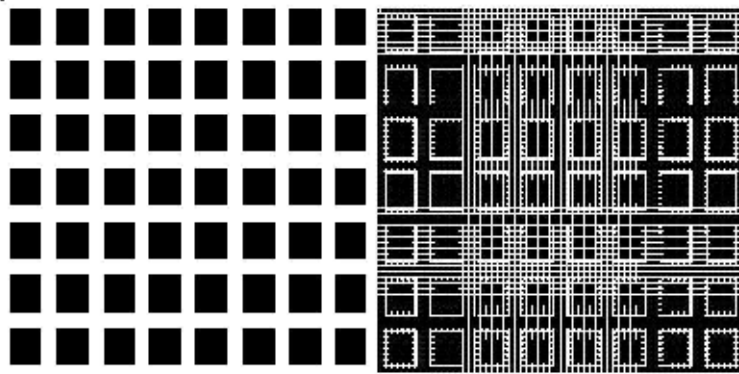


Figure 2.3: A simple schematic illustrating the difference between the input and output of the coefficient of variation (CoV) and the Quadtree decomposition (QtD) for two sample images. The CoV is identical in both cases since both images have 50% black squares and 50% grey squares. QtD gives different values (4 blocks for the left-hand image, and 64 for the right) because it groups ‘like’ regions together. The QtD method recursively divides the image into quadrants, until each quadrant bounds a block of pixels that have similar intensity. The more heterogeneous the image, the larger the number of QtD quadrants that will be required.

Figure 2.4 further illustrates the differences between the FD and QtD methods. Figure 2.4a shows a uniform grid, analogous to an end inspiration lung volume where parenchyma can be considered maximally stretched and relatively uniform. In Figure 2.4c the grid is ‘compressed’ in the vertical direction, and is analogous to the end expiratory lung volume where parenchymal density distribution is greatly influenced by gravity, and considerable deformation of the spongy tissue takes place. Figure 2.5 shows the calculation of a FD for the illustrative examples. The uniform grid from Figure 2.4(a) results in lower CoV values overall than the gradient grid from Figure 2.4(c), but the slope is steeper and therefore the FD is higher. Figures 2.4b and 2.4d illustrate the application of a quadtree decomposition on the

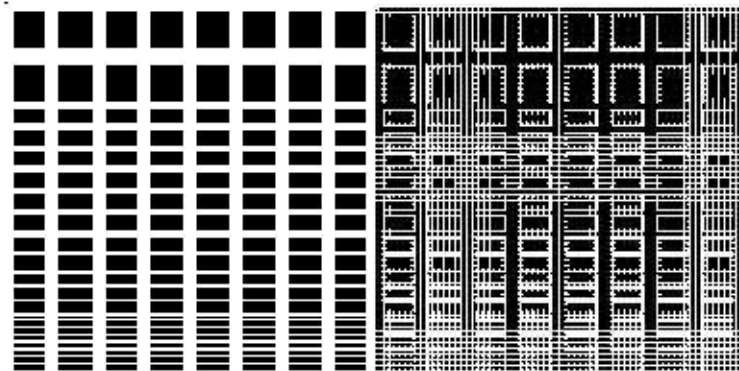
sample images. The uniform grid decomposes to a QtD metric of 0.074, whereas the gradient grid decomposes to 0.136. These simple examples suggest that FD values calculated for end-inspiratory images would be higher than end-expiratory; and QtD metrics would be the opposite (highest for end-expiratory images).

In the FD calculation in the current work the CoV was calculated for sampling window sizes ranging from 1x1 pixels to 8x8 pixels. A threshold range of 100 HU was used for the QtD method. To allow comparison between subjects and between image slices within a subject, the number of boxes for each image's decomposition was normalised by the total area of lung tissue in the image slice. The QtD algorithm was programmed to exclude regions of high HU (corresponding to blood) to eliminate edge effects between vessels and lung tissue. The range of the number of boxes created in this manner was from 10,000 to 20,000, so the boxes outside the lung tissue area were not removed as the quantity was negligible in comparison.



(a)

(b)



(c)

(d)

Figure 2.4: Simple schematic to illustrate the Quadtree Decomposition (QtD) and Fractal Dimension (FD) methods. The image in (a) is divided into equal sized blocks that decompose to the grid on the image in (b), with QtD Metric = 0.074. The image in (c) has a gradient in block size that decomposes to the grid in (d), with QtD Metric = 0.136.

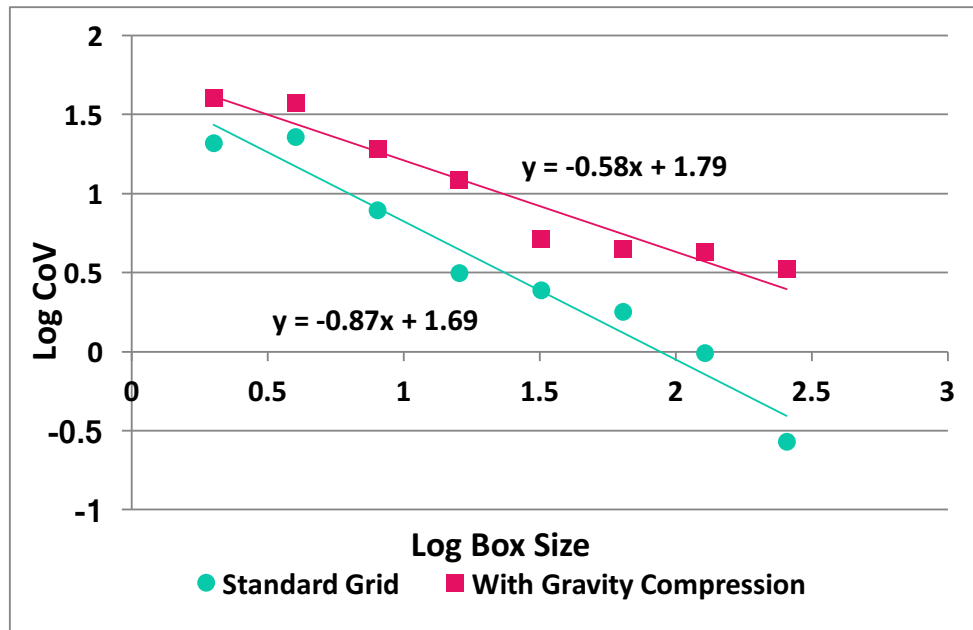


Figure 2.5: Calculation of a FD for the illustrative examples in Figure 2.4. The figure shows the log-log plot of CoV against box size for the images in Figure 2.4(a) and (c). The uniform grid from Figure 2.4(a) has lower CoV values overall than the gradient grid from 2.4(c), but the slope is steeper and therefore the FD is higher.

The two heterogeneity assessment methods were implemented in custom written MATLAB code. Each analysis method was applied to three image slices that were positioned at 25%, 50%, and 75% of the distance along the craniocaudal axis, where 0% was defined as the location of the dome of the diaphragm, and 100% was the most apical point of the lung. Results present the mean of values calculated for all three image slices. FD and QtD were compared by age, lung volume (EE and EI), and BMI. The positions of the slices chosen are illustrated in Figure 2.6.

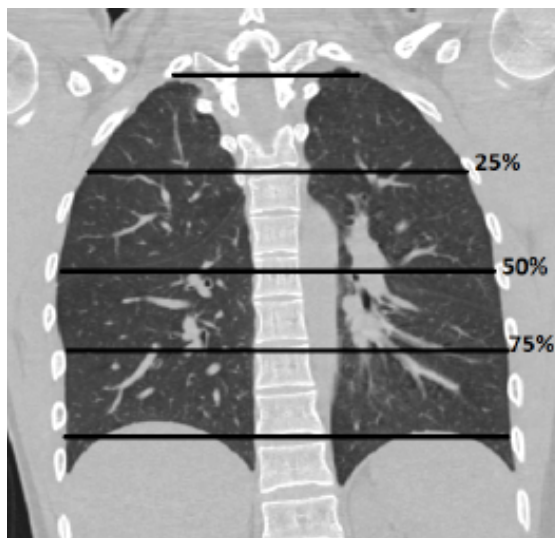


Figure 2.6: The positions of the three slices chosen for the QtD analysis.

The heterogeneity values reported in the results for this chapter were calculated when the Quadtree decomposition was performed on MDCT images of size 512x512, however different imaging modalities have different typical resolutions. For this algorithm to be used with other imaging methods, we need to understand how resolution affects the calculated heterogeneity metric. To simulate the effect of scaling an image to a different resolution, the 512x512 images were reduced to 256x256, 128x128, and 64x64 pixels, after which they were scaled up to 512x512 again, in order to produce a blurred image (presumably with lower heterogeneity). The QtD metric was calculated at each 'resolution'.

The Quadtree technique was used with the condition that boxes were divided if the pixel intensity range was greater than 100 Hounsfield Units (approximately 10% of the full intensity range of the image excluding high-frequency noise). Boxes were excluded from decomposition if the pixel intensity range within a box was less than 100 Hounsfield Units, or the pixels had high intensity values associated with blood or

other tissue. To determine how the threshold influences the calculation of heterogeneity, the threshold was increased as a proportion of the full intensity range of the image, and plotted against the resultant QtD values.

2.3 Results

Table 2.2 lists lung air volumes and dimensions calculated from volumetric imaging at EE and EI. The only significant difference between the two age groups was a smaller change in lung volume from upright functional residual capacity (FRC, as measured in PFTs) to supine EE volume in the older compared with younger subjects ($p=0.04$). The EE and EI air volumes (V_{EE} and V_{EI} , respectively) and the dimensions along each of the three axes were not significantly different between the two groups. The MLD (Table 2.3) was significantly smaller at EE in the > 60 years group ($p = 0.008$), but was not different at EI.

Figures 2.7(a-c) illustrate the distribution of ρ in three orthogonal axes at the two imaged lung volumes. ρ is shown normalized by the respective mean MLD for the volume and cohort. The dependent variable in these figures is shown on the x-axis, and the independent variable (percentage of distance along axis) is on the y-axis. The craniocaudal (Figure 2.7a) distribution at EI is very similar for both age groups: ρ is close to MLD between approximately 10 – 80 % distance, it increases by 30% in the most apical 20% (by distance) of the lung, and decreases by 20% in the most basal 10% (tissue largely within the costodiaphragmatic recess). The EE distribution for the < 30 years group is similar to the EI distributions, except for the lack of increase in ρ from 80-100% distance (apical). The EE distribution in the > 60 years

group is noticeably different from the other curves. There is an approximately linear decrease in tissue density of approximately 30% from 5-90% distance from the base, and a small increase in density in the remaining 10% of lung height.

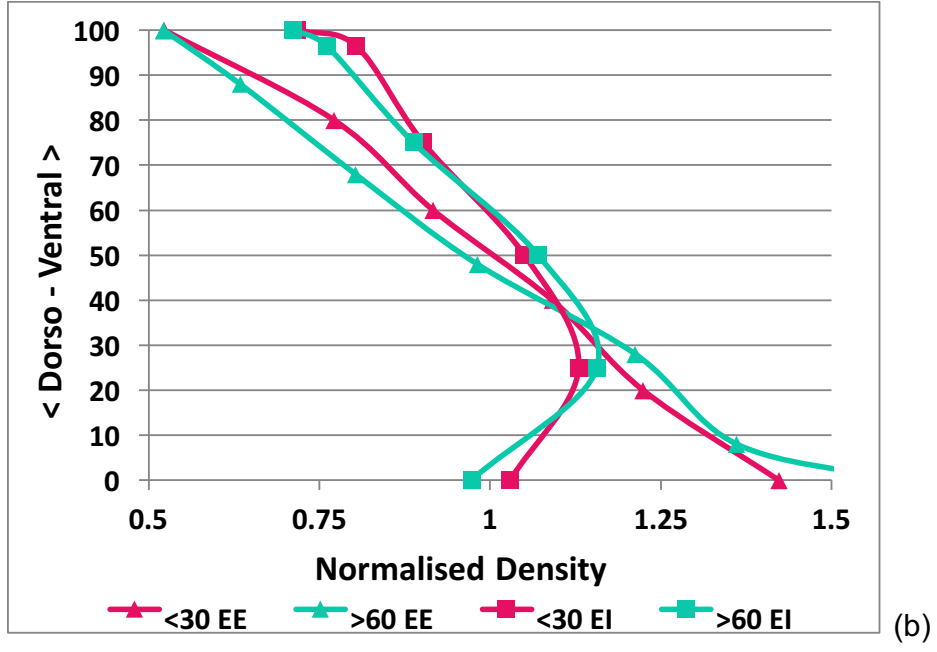
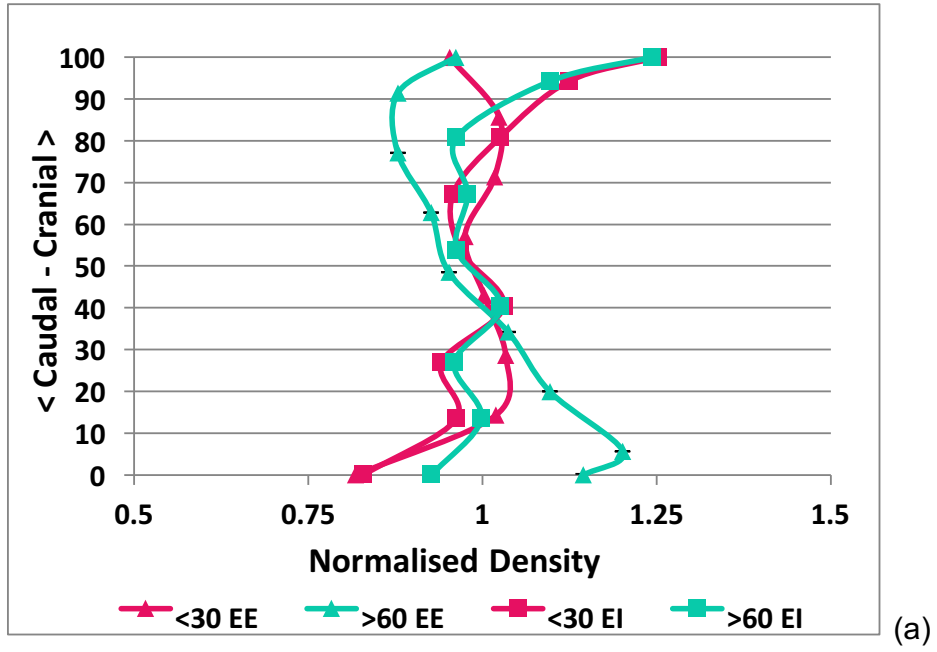
Table 2.2: Lung volumes and dimensions from volumetric MDCT imaging. End expiratory and end inspiratory lung air volumes are given from volumetric image reconstruction (supine) by subtraction of tissue and blood volumes. Values are given as means, with standard deviation in brackets. Significance for the paired t-test at the 5% level is indicated by *.

	Subjects aged < 30 years	Subjects aged > 60 years	p-value (paired t-test)
End expiratory air volume (V_{EE}) supine, from MDCT (L)	2.10 (0.54)	2.48 (0.50)	0.15
End inspiratory air volume (V_{EI}) supine, from MDCT (L)	5.27 (1.14)	4.98 (1.16)	0.43
Difference in supine V_{EE} from upright FRC (L)	-0.81 (0.72)	-0.22 (0.35)	0.04*
Difference in supine V_{EI} from upright TLC (L)	-1.17 (0.66)	-1.13 (0.29)	0.90
Lung craniocaudal height at end expiration (mm)	160(15)	154 (19)	0.14
Lung craniocaudal height at end inspiration (mm)	201(17)	199 (21)	0.73
Lung mediolateral width at end expiration (mm)	260 (19)	260 (30)	0.93
Lung mediolateral width at end inspiration (mm)	283 (23)	280 (35)	0.68

Table 2.3: Densitometric values from volumetric MDCT imaging. Values are given as means, with standard deviation in brackets. Significance for the paired t-test at the 5% level is indicated by *.

	Subjects < 30 years	Subjects > 60 years	p-value (paired t-test)
Mean lung density (MLD, g/cm³) and lung attenuation at end expiration (EE)	0.26 (0.033) -742 (33)	0.22 (0.026) -784 (26)	0.01*
Mean lung density (MLD, g/cm³) and lung attenuation at end inspiration (EI)	0.12 (0.008) -883 (8)	0.12 (0.011) -885 (11)	0.81

The dorsoventral axis aligns with the direction of gravity during supine imaging. The EI and EE distributions of ρ both show a gravitational influence for both age groups (Figure 2.7b), with ρ decreasing with increased distance along the dorsoventral axis. There are no obvious differences between the ρ distributions for the two age groups at the respective volumes. That is, for both age groups at end expiration the normalized ρ decreases approximately linearly (over a range of $\pm 50\%$ from the mean) with increasing distance over the entire range, whereas at end inspiration the normalized ρ decreases approximately linearly from 30-100% distance and increases in the most dependent 30% of the lung (by distance).



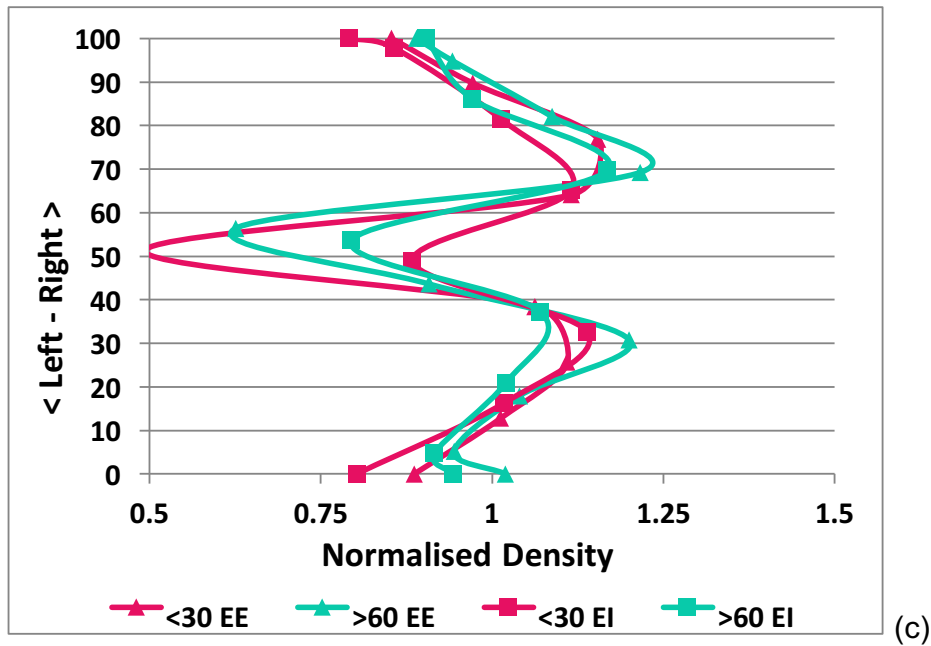


Figure 2.7: (*This page and preceding*). (a) Craniocaudal (top), (b) dorsoventral (middle) and (c) mediolateral (bottom) distributions of lung tissue density in subjects aged <30 and >60 years of age, at EE and EI volumes. Note that the dependent variable (density in a 5 mm section of tissue normalised by MLD) is graphed on the horizontal axis, and the independent variable (distance to tissue section normalised by total distance) is graphed on the vertical axis such that the density values correspond to the lung orientation in the insert images. The scatter of the results was not significant, and therefore error bars are not shown. The patterns of density distribution amongst the subjects were consistent.

The mediolateral axis is shown running from the left lateral surface (0%) to the mediastinum (~50-60%) to the right lateral surface (100%). The distribution for each volume and age group is similar (Figure 2.7c): ρ increases with distance from the lateral surface (of either lung) to approximately 30% of the distance into the lung (i.e. ~60% of the distance into a single lung), and then decreases to the medial surface.

The mean FDs at end inspiration (expiration) were 0.43 ± 0.088 (0.15 ± 0.064) and 0.41 ± 0.11 (0.15 ± 0.045) for the younger and older groups, respectively. There was no significant difference in FD between the two age groups at either volume ($p = 0.62$ and 0.89 for EI and EE, respectively). In contrast, the FDs at the two volumes were significantly different in both age groups ($p < 0.0001$ for subjects < 30 and subjects > 60 , respectively). The relationships between FD and age at each volume are shown in Figure 2.8.

The number of boxes per unit area calculated using Quadtree decomposition (QtD) was not significantly different between the two age cohorts for either of the two lung volumes, and there was no trend for QtD with age (Figure 2.9). QtD at end inspiration (expiration) was 0.24 ± 0.035 (0.35 ± 0.073) for the younger group and 0.24 ± 0.049 (0.33 ± 0.066) for the older group, with $p = 1.0$ and $p = 0.70$ for EI and EE, respectively. QtD was significantly different at the two lung volumes in both age groups ($p = 0.0021$ and 0.0040 , for subjects < 30 and subjects > 60 , respectively).

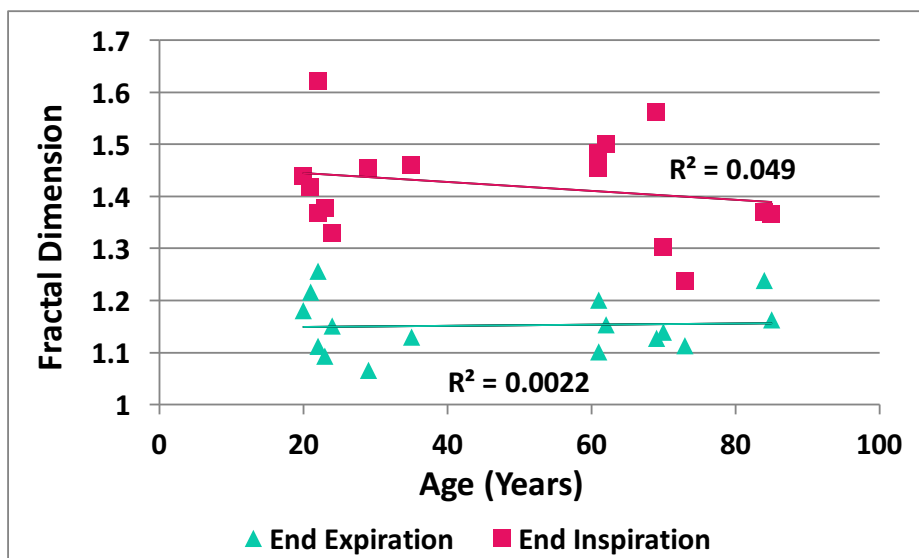


Figure 2.8: The relationship between fractal dimension and age for EE and EI inflation volumes. No significant relationship was found between the two age groups at either volume.

When all subjects from the two groups were pooled, MLD at EE, but not EI, was proportional to BMI, although this was a relatively weak relationship (with an R^2 of 0.16 for EE and 0.079 for EI). FD and QtD both show significant relationships with BMI (Figures 2.10 and 2.11 for FD and QtD, respectively). FD decreased with increasing BMI, at both EE and EI; and QtD increased with increasing BMI. R^2 values of >0.6 indicate relatively strong relationships between FD or QtD and BMI, for all but FD at EI ($R^2 = 0.19$).

To confirm that the location of images selected for analysis did not unduly impact the results, QtD was compared for the three image locations, calculated using images located 25%, 50%, and 75% of the distance along the craniocaudal axis (Table 2.4). The EI and EE QtD values at each image location were significantly different from each other ($p < 0.01$ for all three locations). QtD tended to be largest in the 25% image, but was not significantly different from the other two image locations. This

analysis was repeated using additional axial images and using reconstructed images from other planes (results not shown). The trends were the same therefore to minimize the analysis time only three image locations were used.

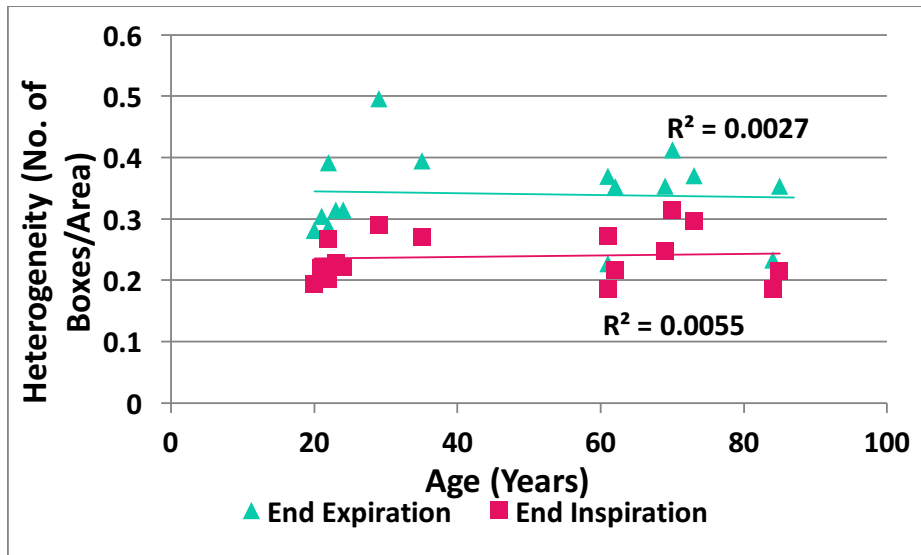


Figure 2.9: The relationship between QtD heterogeneity and age for EE and EI inflation volumes. No significant relationship was found between the two age groups at either volume.

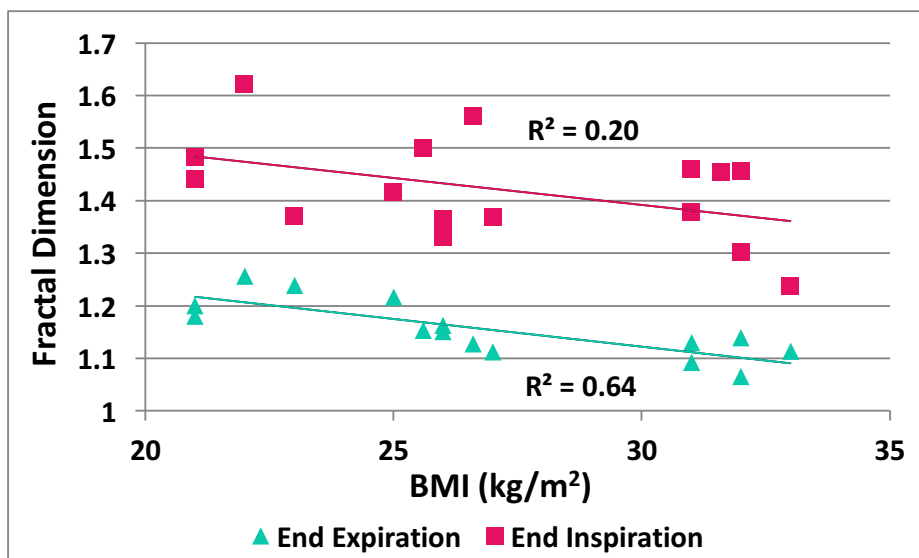


Figure 2.10: The relationship between fractal dimension and BMI for EE and EI inflation volumes, for pooled data from both age groups. The EI data results in higher FD values. FD decreases with increasing BMI at both lung volumes, but the data spread for EI is relatively large and the correlation is weak.

Table 2.4: Statistics for the three slice locations for QtD measurements. The QtDs of the three slice locations were not significantly different from each other, within each volume. Between End Expiration and End Inspiration, the p-values for corresponding slice locations all proved significantly different from each other i.e. at 25%, 50%, and 75% $p_{QtD_EE-EI} < 0.0001$.

End Expiration	Slice 1: 25%	Slice 2: 50%	Slice 3: 75%
Mean	0.37	0.34	0.34
S.D.	0.08	0.07	0.06
Slice 1-2	p = 0.26		
Slice 1-3	p = 0.23		
Slice 2-3	p = 1.00		
End Inspiration	Slice 1: 25%	Slice 2: 50%	Slice 3: 75%
Mean	0.25	0.23	0.23
S.D.	0.04	0.03	0.03
Slice 1-2	p = 0.12		
Slice 1-3	p = 0.12		
Slice 2-3	p = 1.00		

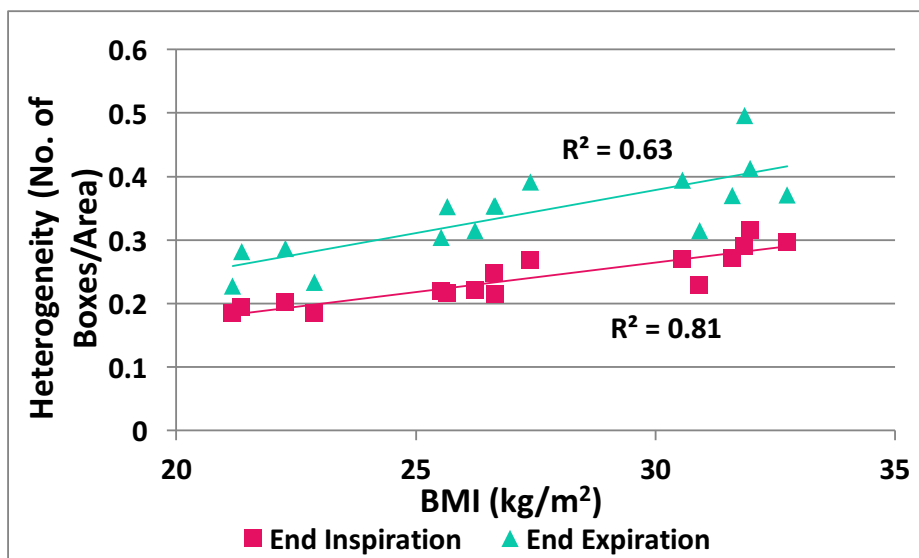


Figure 2.11: The relationship between QtD heterogeneity and BMI for EE and EI inflation volumes, for pooled data from both age groups. The QtD at EE is higher than at EI. Both lung volumes show trends of increased heterogeneity with BMI.

Figure 2.12 shows QtD plotted against image ‘resolution’ to which an original image of size 512x512 was scaled. The number of boxes per area reduced with image scaling/blurring, which is consistent with expectations for this decomposition method. The consistent relationship between image resolution and QtD in Figure 2.12 suggests the possibility of calibrating the heterogeneity metric for different imaging modalities with different characteristic resolution, allowing for improved comparison of heterogeneity between modalities.

Figure 2.13 shows that increasing the threshold range for QtD decreases the QtD metric towards zero. As expected, QtD reduces dramatically if the threshold is too broad. A consistent relationship such as this might allow for calibration between different studies that use different threshold values for the QtD method.

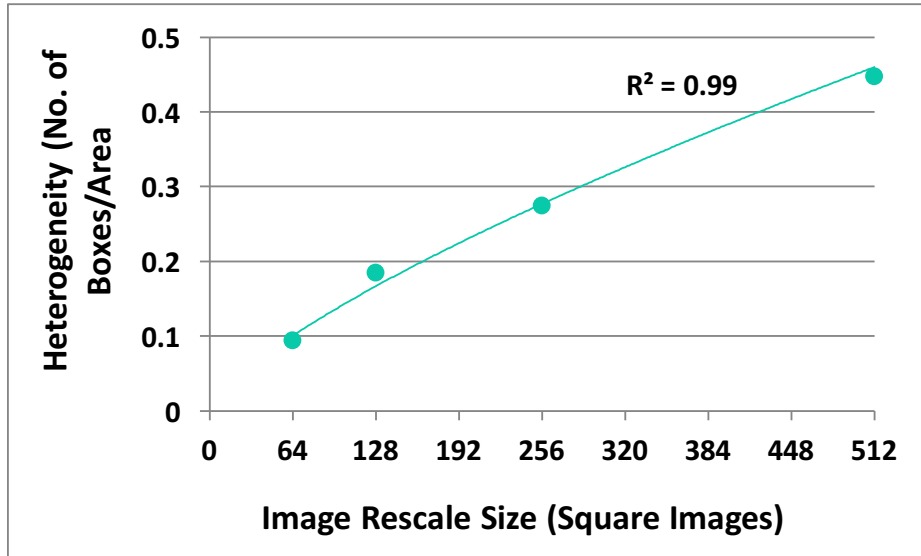


Figure 2.12: The effect of reducing and then enlarging (i.e. blurring) images on QtD. The heterogeneity metric reduces with lower image resolution.

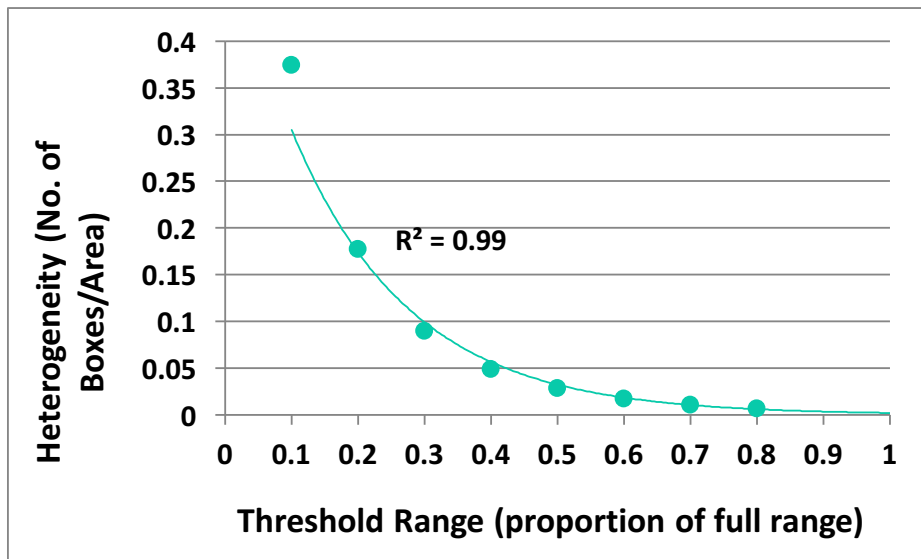


Figure 2.13: The effect of changing the threshold window used for decomposition during the decomposition process.

2.4 Discussion

The lung undergoes changes to its tissue microstructure with age that are reflected in an age-related decline in most standard measurements of lung function. Studies based on subjective assessments of thoracic CT agree that the older lung has airway and/or tissue appearances that would be considered abnormal if present in the younger adult lung. What has not been clear is whether there are subtle age-related changes to the CT appearance of the lung tissue that could be detected using quantitative methods. The current study used an objective quantitative assessment to determine whether never-smoking younger (< 35 years) and older (> 60 years) subjects with no significant prior respiratory disease have differences in tissue density distribution and tissue heterogeneity on supine volumetric CT. In contrast to previous studies no age-related differences in the lung tissue were found. However, strong relationships were observed between BMI and metrics for tissue heterogeneity.

The two age groups that were selected for comparison differ by more than 45 years. The younger group represents early maturity, at an age at which lung function has peaked or has entered the early stage of decline (119) The older group is well into the age at which significant lung tissue remodelling is expected to have occurred (119). Static (breath-hold) volumes in the upright and supine postures did not differ with age, whereas dynamic volumes (from forced spirometry) were significantly smaller in the older subjects. The lack of difference in static volumes along with the smaller dynamic volumes in the older subjects indicates age-related differences in the lung tissue and/or airway mechanics. Percent predicted FEV₁ was high in both groups (117% and 123% for younger and older, respectively), but not significantly

different between them ($p = 0.51$). FEV_1/FVC was not significantly different with age ($p = 0.25$); that is, the ratio for the younger group was the same as predicted (83% compared with 81%, $p = 0.19$), whereas the older group was larger than predicted (80% compared with 68%, $p = 0.0003$). The high percent predicted FEV_1 and relatively high FEV_1/FVC in the older group are consistent with the older subjects representing a healthy sub-group of elderly with no airflow limitation.

The MLD at EI did not differ with age, whereas MLD was 0.04 g/cm^3 smaller in the older group at EE. Well et al. (117) showed a decrease in lung attenuation from approximately -840 HU at 20 years of age to approximately -890 HU at 90 years of age which is presumably associated with increased airspace enlargement. Our mean lung attenuations of -883 and -885 HU for the younger and older group, respectively, correspond to their fitted relationship between attenuation and age at around 80 years of age. Genevois et al. (37) showed a mean attenuation across men and women aged 21-73 years of -866 HU, and like our study did not find a significant decrease in attenuation with age. That is, the EI lung attenuation in this was lower than the average attenuation in these previous studies. However, the images in this study were obtained from volume controlled imaging whereas participants both previous studies were encouraged to breath maximally, rather than to a controlled volume.

Static elastic recoil of the lung decreases at a rate of about $0.1\text{-}0.2 \text{ cmH}_2\text{O/year}$. Deformation of the lung tissue within its semi-rigid 'container' could therefore be expected to be different with age. Elastic recoil was not measured directly in these subjects, however the smaller FEV_1 and FVC (and elevated residual volume, not shown here) in comparison to the younger subjects suggests a change in tissue

and/or airway mechanics with age that is consistent with other studies (49). It is therefore reasonable to assume that the loss of tissue elastic recoil would also be consistent with previous studies. If hyperinflation was significant in the older group, then the tissue density gradient would be expected to be smaller. Conversely, in the absence of significant chest wall remodelling in older age, loss of elastic recoil (i.e. increased tissue compliance) could result in a larger tissue density gradient, or appear as increased air trapping due to airway closure. However the distribution of tissue density (Figure 2.7b) in the gravitational direction (the dorso-ventral axis) was not noticeably different between the two age groups at either lung volume, and nor was there any difference in the distribution medio-laterally. Figure 2.7a shows similarity in the craniocaudal density distribution at EI but not EE. For the younger subjects at both lung volumes and the older subjects at EI, the density was relatively constant through the middle 10-90% of lung height (base to apex). For the older subjects at EE, a gradient in density was observed over the same height range, with lowest density in the lung apices. Variation from these trends in the most apical and basal 10% of tissue is probably because this represents relatively small volumes of tissue, and the basal tissue is adjacent to the diaphragm (or in the recess) so could experience some motion during imaging.

Two metrics of lung tissue heterogeneity were calculated: a fractal dimension (FD), and the number of boxes by Quadtree decomposition divided by lung area (QtD). The FD was larger at EI than EE, and the opposite relationship with volume was found for QtD. Figures 2.4 and 2.5 provide an explanation for how FD and QtD are affected by characteristic changes to the distribution of lung tissue density with lung volume change. At EI the tissue density is expected to be less dense and more uniformly distributed than at EE; at EE the greater density of the lung tissue means

that it experiences greater deformation due to gravity, and therefore develops a distinct gravitational gradient (as in Figure 2.7b, and represented by the pattern in Figure 2.4c). Although the coefficient of variation (CoV) is largest for the pattern with a gradient (Figure 2.4), the FD (calculated as the magnitude of the slope of the log-log plot of COV against box size in Figure 2.5) is smaller than for the more uniform case. Quadtree decomposition divides the uniform pattern in Figure 2.4a into fewer boxes than the pattern with a gravitational gradient (Figure 2.4c), thus implying higher heterogeneity when the gravitational gradient is present. QtD calculated for the uniform pattern is lower than for the pattern with a gradient. QtD is therefore smallest when the tissue is most uniform, at EI.

Neither FD nor QtD differed with age in our study. This contrasts with Copley et al. (18) who found a higher fractal dimension in the lung tissue of younger (< 55 years) compared with older (> 75 years) subjects. There are several methodological differences between the two studies. Copley et al. (18) analysed prone imaging whereas our study used supine volumetric images. Gravitational tissue deformation is less pronounced in the prone posture (84, 86), which is similar to the reduction in gravitational deformation in the lung at EI. While both age groups in Copley et al. were older than in the current study (39.4 ± 7.5 and 80.9 ± 4.2 years, compared with 24.5 ± 4.7 and 70.8 ± 9.2 years), the difference in age was similar. If the change in MLD with age is linear with time (as suggested by Well et al (117)), then it is not likely that this would contribute to the difference in study outcomes; on the other hand, if changes in MLD accelerate in older age then this could result in differences between the two studies. Copley et al. examined selected regions of interest at five thoracic levels on bands of tissue 25 pixels wide and more than 15 pixels from the lung/pleural interface. Our analysis was applied to images at three locations, and

included all non-airway and non-vessel pixels in the images. The heterogeneity metrics did not differ between image location, despite the images being sampled in regions that have different proportions of airway and blood vessel to alveolar tissue. It is therefore unlikely that the different study outcomes are due to erroneous inclusion of airways and vessels in the analysis. The method for calculation of a fractal dimension differs between the two studies. Copley et al. used a topological analysis of the image 'surface', whereas the current study used a more simple calculation. While the different methods would give different quantitative results, it is not likely that they would have other systematic differences.

In contrast to the absence of an age effect on tissue heterogeneity, there was a strong relationship between BMI and the two heterogeneity metrics: with increasing BMI, FD decreased and QtD increased. Increased adipose tissue with BMI has been suggested to attenuate signal in thoracic CT (46), however this would not be expected to affect the heterogeneity in the image. A number of techniques have been suggested for increasing signal strength in obese patients (75), however these guidelines are generally recommended for those with a BMI greater than 40 (well above the highest BMIs used in this study). In general, if the patient can fit into the scanner, the quality of imaging is unlikely to be greatly reduced (113). If the same radiation dose is used as for a thinner patient, then signal attenuation may occur, although in general this results in reduced contrast overall, and this effect was not seen in our images. Thus, either signal attenuation was minor, or the radiation dose was increased to compensate for abdominal fat and create better contrast. Noise in the form of quantum mottle (46, 75) was not present in our images, and neither was truncation noise. A heterogeneity analysis on the darker areas surrounding the lung parenchymal tissue was done to check if there was specular noise causing more

heterogeneity, however no heterogeneity was found in these 'blank' regions. Specular (high intensity) noise was also removed as part of the segmentation and filtering pre-processing steps, and would therefore have played no part in the QtD algorithm. In addition, a histogram analysis was done on all images to ensure that their histograms were similar and occupied the same range of intensities.

MLD at EE, but not EI, was proportional to BMI. MLD depends on the amount of air in the lung and the amount of tissue (including inflammation) and blood in the parenchyma and small vessels, therefore MLD could increase with BMI (at EE) due to a lower proportion of air in the lung during imaging, or in the presence of inflammation, or because of larger blood volume. If the former, then the FD and QtD trends with BMI could be reflecting the relationship to imaged lung volume seen in Figures 2.10 and 2.11 for EE and EI. If inflammation was present this would increase MLD, but for it to affect QtD and FD would require that inflammation was heterogeneously distributed in proportion to BMI, for which there is no evidence. MLD could also increase with BMI because of larger blood volume. As lung volume decreases, the stretch on the pulmonary capillaries also decreases. This increases capillary sheet 'height', reduces pulmonary vascular resistance, and contributes to increased pulmonary blood volume. It is possible that there was a small decrease in lung volume with increased BMI that lowered the pulmonary vascular resistance and therefore allowed for a greater pulmonary blood volume. We say 'possible' because we don't know the volume that the lung would have been at a lower BMI in any individual, therefore we cannot say with certainty that higher BMI is associated with lower lung volume in this cohort. The role of increased blood volume remains speculative, and it is not yet clear how this would contribute to increased heterogeneity. Finally, there was a trend in our subjects for females to have lower

BMI. Some of the apparent relationship between BMI and heterogeneity could therefore be associated with gender differences. Larger numbers of subjects would be required to assess this.

2.4.1 Study Limitations

A relatively small number of subjects was used for the current study (8 in each age group). The number of subjects was constrained by access to volume-controlled imaging from healthy non-smoking subjects. Data are available for more subjects in the younger age group, but not the older group. To increase the study numbers the current methods could be tested on clinical imaging, however as this would not be volume controlled the variability of heterogeneity metrics within each age group would be expected to be larger.

Unlike previous studies we excluded subjects with radiologist-identified abnormalities. Considering that the presence of some airway and tissue abnormalities is considered 'normal' for the older lung, it is possible that we selected 'super-normal' subjects that are not representative of the typical older subject. Further study would be required to evaluate whether there are differences between the older subjects used here, and older subjects identified with mild abnormalities.

CHAPTER 3

EVIDENCE FOR AGE-DEPENDENT AIR-SPACE ENLARGEMENT CONTRIBUTING TO LOSS OF LUNG TISSUE ELASTIC RECOIL AND INCREASED SHEAR MODULUS IN OLDER AGE

3.1 Introduction

During ageing the lung undergoes microstructural changes that affect its mechanical (30, 65, 111) and gas exchange function (73). This includes alveolar ‘airspace enlargement’ (57, 107), which reduces the gas exchange surface area and is associated with a loss of lung elastic recoil pressure (63, 72). This senescent microstructural remodelling differs from the pathologic destruction of the alveoli that defines pulmonary emphysema (44, 112) (a component of chronic obstructive pulmonary disease, COPD, which has age-related prevalence). While many of the microstructural changes that accompany senescence are well documented (19, 56, 72, 98), how they contribute to the emergence of age-related decline in lung elastic properties at the macroscopic level remains unclear.

The elastic recoil pressure of the lung (which is of equal magnitude to transpulmonary pressure) decreases – on average – with age. Janssens et al. (49)

report a rate of almost 198 Pa (2 cmH₂O) per decade between the ages of 25 and 60 years, while Niewoehner et al. (80) report a rate of approximately 120 Pa (1.2 cmH₂O) per decade for the same age range. While the lung elastic recoil pressure decreases, other volume-independent elastic moduli (the bulk and shear moduli) increase with age (55). Experimental studies suggest that the total lung contents of collagen and elastin do not change during ageing (58), but their distribution in the alveolar wall changes and collagen becomes more stable with age, with an increase in intermolecular cross-links (111). Some studies have also suggested a slight thinning of alveolar walls and a reduction in the density of capillaries (19). Loss of elastic recoil pressure is also associated with airspace enlargement: morphometric studies have shown a marked dilation of respiratory bronchioles and alveolar ducts and a shallowing of alveoli in older age (111); studies on senescence-accelerated mice (SAM mice) (44, 112) also support this, showing a significant increase in duct size with age that occurs homogeneously throughout the lung tissue and without alveolar wall destruction or inflammation. Mercer and Crapo (71) and Toshima et al. (109) have described the distribution and structure of collagen and elastin at a microscopic scale, highlighting the differences in composition of proteins in the alveolar mouth regions, compared with the septal walls. Toshima et al. also discussed the stress-bearing characteristics of protein fibres at a microstructural level. However, exactly how changes to the distribution of constituent proteins and/or airspace enlargement translate to a decrease in lung elastic recoil pressure and an increase in bulk and shear moduli is not clear.

Micromechanical analysis at the scale of the alveolar walls and composites of alveoli provides a tool by which these mechanisms can be understood. Such models have previously been employed in physiological studies to investigate various phenomena

that affect parenchymal tissue at a microstructural scale (15, 20-24, 36, 51, 97), although they generally do not consider age affects. Suki and Bartolák-Suki (98) considered the mechanics of the ageing lung using multiscale models that include the contribution and proportion of elastic fibres (collagen and elastin) and their interaction via the proteoglycan matrix. They focused on the contribution of extra-cellular matrix stiffening with age to changes in total parenchymal stiffness, rather than the contribution of alveolar geometry per se. Gefen et al. (36) developed a model for analysing the stress distribution in the alveolar septa of normal and emphysematous lungs using data from experiments conducted on human lung tissue (97). They concluded that this approach was useful in understanding the stress distributions experienced by the lung's microstructure at various inflation volumes. Chen et al. (15) used a similar method to postulate the stresses experienced by the alveolar walls of subjects with Acute Respiratory Distress Syndrome (ARDS) when the lung was subjected to mechanical ventilation. They concluded that the magnitudes of stress depended mainly on the amount of fluid within the alveoli, the alveolar opening velocity, and the tension on alveolar walls exerted by neighbouring alveoli. Truncated polyhedron alveolar models were used by Denny and Schroter in several studies (21-24). The polyhedra were 'packed' in a space-filling manner, forming a cuboid block. Elastic moduli for the block were then calculated by simulating uniaxial extension on the structure. In particular, Denny and Schroter noted that the deformations of lung parenchyma are large, and that selecting a constitutive model that accurately simulates large, anisotropic, non-linear distortions is essential. The importance of selecting an appropriate material model was also emphasized by Dale et al. (20), who used similar polyhedra in their simulations. Karakaplan et al. (51) suggested a model that utilized polyhedron-shaped alveoli,

with the alveoli arranged around a central cylindrical duct. This simulated a lowest-level air duct, with alveoli branching off it.

Experimental data are necessary for parameterizing these models, and provide a basis for model validation, however it is extremely challenging to acquire data for the stress-strain relationship of intact alveolar tissue, and it is even more difficult to separate the contributions of tissue elasticity and surface forces. While the latter are extremely important in determining intact lung mechanics, current experimental methods can only provide information on the mechanics of tissue that has coupled elasticity and surface forces. Rausch et al. (87) provided a summary of lung tissue stress-strain tests acquired from a range of studies (from various mammalian species) along with a comparison of several constitutive laws and their relative advantages in simulating elastic material behaviour. It is interesting to note that the stress-strain relationships acquired from the different studies vary so greatly that characterising a 'typical' behaviour would be difficult.

The primary aim of this study is to determine whether age-dependent differences in the characteristic configuration of the alveoli and alveolar ducts contribute to the differences in lung tissue elastic recoil pressure and bulk and shear modulus that have been observed with age, using a structure-based model where the physical properties of the constituents of the alveolar wall and mouth are assumed to not change with age. A secondary aim is to understand how characteristic differences in the elastic properties of the alveolar mouth and septa with age contribute to the elastic behaviour of the lung tissue. Here we examine how these two phenomena independently affect the micromechanics of lung parenchymal tissue.

3.2 Methods

3.2.1 Model Geometries

Three model geometries were constructed for the purpose of analyzing their elastic behaviour under simulation of uniaxial tension and simple shear. The models were designed to represent small samples of excised parenchymal tissue. The scale of this micromechanical modelling encompasses alveolar walls (of the order of a few μm) and a few alveoli (each of which is a few hundred μm in length). That is, the individual constituents of the alveolar wall such as elastin and proteoglycans, and millimetre-scale terminal airways and blood vessels are not included. The first ('closed alveoli') model was completely filled with space-filling truncated octahedra (each representing a single alveolus); that is, this model was devoid of ducts, and the alveoli did not have openings between them. The second and third model geometries included alveolar ducts, such that each alveolus opened onto a duct. The second ('young alveolar/duct') and third ('old alveolar/duct') models had alveolar and duct dimensions appropriate for the 'young' and 'old' adult human lung, respectively. The dimensions of the models were 0.36 mm x 0.36 mm x 0.48 mm (closed alveoli), and 0.5 mm x 0.5 mm x 0.9 mm (young and old alveolar/duct).

To construct the space-filling and alveolar/duct models, finite element models of single alveoli as space-filling truncated octahedra were first constructed using SolidWorks 2013 (93) (Figure 3.1a and 3.1b). These were used as repeating units in the more complex models that comprised multiple alveoli. Each alveolus was modeled as a 12-sided polyhedron with edge length 40 μm , diameter 200 μm , and septal wall thickness 8 μm . For the closed alveoli model the repeating units were packed into the block with no gaps between adjacent units. All alveolar septa that

intersected the block surface were truncated at the surface, to assist in specifying boundary conditions. To create the alveolar/duct models, all of the faces along one row of adjacent alveolar units were removed (except for one face at the duct terminus). This resulted in a central duct geometry that was surrounded by alveoli with alveolar mouths opening on to the duct. The duct was open at one end and closed at its terminus. Only a single duct was created within the model geometry: alveolar units that were not adjacent to the duct remained closed. As in the closed alveoli model, the septal walls of the alveoli at the block surface were truncated to give planar surfaces at the extremities of the tissue block. Figure 3.1c shows the internal geometry of the young alveolar/duct model. For the old alveolar/duct model, the repeating alveolar unit was truncated orthogonally to the alveolar mouth opening, thus making the alveoli shallower than in the young alveolar/duct model, and resulting in a reduced surface area. Both the old and young alveolar/duct models comprised 25 non-truncated alveoli around a central duct. Mean linear intercept (L_m) (7, 112) for the young and old alveolar/duct models was $L_m = 236 \mu\text{m}$ and $342 \mu\text{m}$, respectively. Alveolar and duct dimensions, tissue volume as a proportion of model volume, and surface to volume ratios for all models are listed in Table 3.1. All dimensions correspond to an assumed (arbitrary) zero-stress (reference) state.

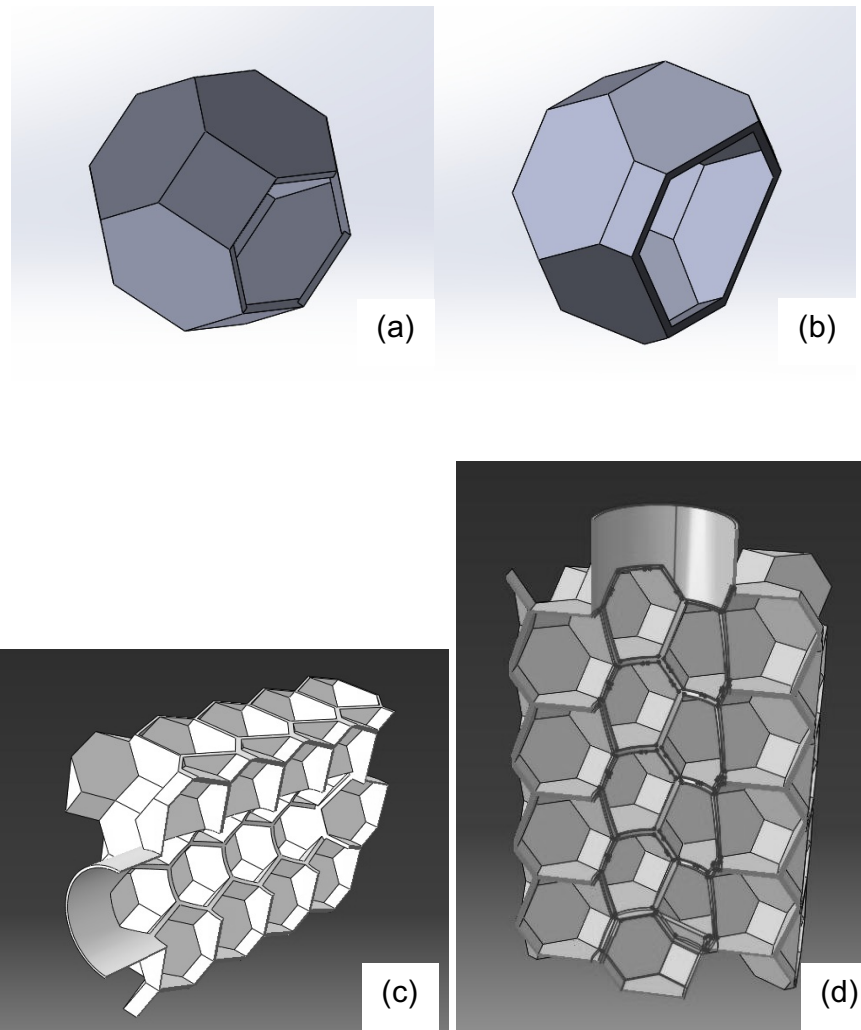


Figure 3.1. (a) A single truncated-octahedral alveolar unit constructed in SolidWorks, showing a ‘young’ alveolus geometry, and (b) the shallow ‘old’ alveolus geometry. (c) shows a cross-section of the finite element alveolar/duct model. The duct is completely enclosed by alveoli, with the only opening being the duct ‘mouth’. (d) highlights the alveolar mouth regions where material properties were altered to simulate non-uniform distribution of collagen and elastin.

Table 3.1. Dimensions of the models used for simulations. Dimensions are given for the models in their reference (undeformed) configuration.

Model	Alveolar diameter (μm)	Alveolar depth (μm)	Duct diameter (μm)	Tissue volume (%)	Surface area to volume ratio (mm^{-1})
Closed alveoli	200	200	N/A	9.0 %	52
Young alveolar/duct	200	200	250	6.3 %	42
Old alveolar/duct	200	166	364	4.6 %	32

Following construction in SolidWorks, the model geometries were imported into Abaqus (1) to generate computational meshes. All of the geometries were meshed using hybrid tetrahedral elements. Hybrid tetrahedral elements were used as these are recommended for complex geometries with large amounts of deformation, as well as to eliminate 'locking' issues. 'Locking', or 'shear locking' can occur due to too much elongation/bending of elements. Abaqus uses 'incompatible mode' elements to remedy this. This introduces elements with more degrees of freedom that are able to interpolate the large deformations. In order to determine the optimum level of mesh refinement, uniaxial extension tests were performed on the closed alveolar block

model with systematic reduction in element size. Mesh independence was assumed when there was < 0.1% difference in the stress and strain solutions. The mesh for the largest model (young alveolar/duct model) consisted of approximately 2 million elements.

3.2.2 Material Properties

The model was treated as an incompressible hyperelastic material. Average stress-strain data for excised human lung parenchymal tissue from Gao et al. (35) were used to parameterize a strain energy function. A standard third-order Ogden function was used as the strain energy function in the current study. The general form of the Ogden function that is used in Abaqus is:

$$U = \sum_{i=1}^N \frac{2\mu_i}{\alpha_i^2} (\lambda_1^{-\alpha_i} + \lambda_2^{-\alpha_i} + \lambda_3^{-\alpha_i} - 3) \quad (3.1)$$

where λ_j denotes stretch in the j^{th} direction, μ_i and α_i are material parameters, and N is the order of the function. Material law parameterization was performed using the interface provided by Abaqus, and data from Gao et al. (35) was used as input to the Abaqus optimiser, which fitted Equation 3.1 to the stress-strain data by converging on the optimum values for $\alpha_1.. \alpha_3$, and $\mu_1.. \mu_3$. Once these parameters were fitted to the stress-strain curve, they were substituted into Equation 3.1 by Abaqus and used for the simulations. The Ogden function was the function that best fit the material properties of the excised tissue. This was determined by testing various strain energy functions, whereby the Ogden function's response proved most stable for our material and the simulated deformations. The optimised values of the coefficients are given in Table 3.2.

The material properties of the closed alveoli model were assumed to be uniformly distributed. Mercer and Crapo (71) reported that a significantly higher proportion of collagen and elastin resides within 10 μm to 20 μm of the alveolar mouth opening, compared to parenchyma on average. The alveolar/duct models were therefore tested using uniform and non-uniform distributions of material properties. A 10 μm wide ring of tissue around each alveolar mouth was selected, and prescribed a 20% increase in stiffness relative to the original model stiffness (Figure 3.1d).

The remainder of the septal walls were prescribed a 20% decrease in stiffness relative to the original model. The altered coefficients for the non-uniform material stiffnesses are given in Table 3.3 (note that an increase in μ increases stiffness, whereas an increase in α decreases stiffness).

Table 3.2. Optimised values for a third order Ogden function representing the stress-strain relationship in excised lung alveolar tissue, with coefficients fitted to data from subjects aged 44-82 years (Gao et al. (35)).

i	μ_i	α_i
1	-6.15e-02	3.05
2	3.46e-02	4.84
3	2.82e-02	-0.22

Table 3.3. Altered coefficients for the Ogden function for the simulation of non-uniform material properties. Coefficients are given for stiffening the alveolar mouth by 20%, and decreasing stiffness in the remainder of the septal wall by 20%.

i	Coefficients for 20% increase in stiffness (Alveolar Mouths)		Coefficients for 20% decrease in stiffness (Septal Walls)	
	μ_i	α_i	μ_i	α_i
1	-7.39E-02	2.54	-5.13E-02	3.66
2	4.16E-02	4.03	2.89E-02	5.81
3	3.39E-02	-0.18	2.35E-02	-0.26

3.2.3 Simulation of Material Deformation

Material behaviour was tested by imposing deformations on the closed alveoli model, the young alveolar/duct model, and the old alveolar/duct model. The young and old alveolar/duct models each had two configurations: uniform and non-uniform material distributions. Thus, a total of five models were considered in the material tests. Three different deformations were used in the simulations: uniaxial extension, isotropic expansion of the model (for estimating the pressure-volume relationship), and simple shear.

Simulation of uniaxial extension was used for validation of the material parameterization, and was designed to simulate material testing of excised lung alveolar tissue (e.g. as described in Rausch et al. (87)). All five models were used in

the uniaxial simulations. Uniaxial stretch was applied by fixing all nodes on one face of the model to have zero displacement, the nodes on the opposite face to displace in the normal direction to the face, and nodes on all other faces to be unfixed (free to move in any direction). The alveolar models were stretched along their axis of greatest length. In the alveolar/duct models, the face with zero displacement also contained the duct opening. Each of the models was subjected to strains ranging from 10% ($\lambda=1.1$), to 40% ($\lambda=1.4$) in order to span the same range of strains as the experimental data (35).

Pressure-volume simulation was performed on all five models. The models were expanded isotropically by applying pressure to all the internal surfaces of the alveoli (simulating positive air pressure). Expansion began at the stress-free (reference) volume, and was incrementally increased until the pressure reached 2475 Pa (25 cmH₂O), which is considered approximately the expanding pressure to reach total lung capacity (TLC) in a healthy adult lung. Increment step sizes are dynamically handled by Abaqus depending on the amount of deformation experienced by the geometry – in later stages of the simulation step sizes are reduced by Abaqus due to the extremely large deformations.

Simple shear deformations were applied to the five models, following each incremental step in pressure inflation as described above. Shear was imposed by fixing all nodes on one of the faces (a face parallel to the longest dimension in the model), and applying uni-directional displacement (in the direction of the longest dimension) to all nodes on the opposite face. The magnitude of shear displacement was, in all cases, 1% of the length of the model in the direction of shear.

In all the simulations displacement boundary conditions were used to fix node locations at the end of each major step (e.g. inflation, extension, shear), in order to counter the material's tendency to 'spring back'.

In order to test the influence that each of the optimised coefficients for the Ogden function had on the stress-strain behaviour of the material, a sensitivity analysis was performed on μ and α following the approach of Reeve et al. (88). μ and α were varied independently (increased and decreased) from their original optimised values (Table 3.3) and uniaxial extension was simulated to assess the sensitivity of the simulated stress to the material law coefficient values.

3.3 Results

An expansion pressure of 495 Pa (5 cmH₂O) approximately doubled the alveolated model volume, and 2475 Pa (25 cmH₂O) approximately quadrupled it. Septal wall thickness decreased with inflation; at the maximum inflation pressure of 2475 Pa (25 cmH₂O) the wall thickness reduced from 8 to approximately 6 μm on average.

Figure 3.2 illustrates the stress-strain relationship for uniaxial extension of the closed alveoli model and the alveolar/duct model for the young adult lung with uniform material properties. Model data are compared with the uniaxial experimental data for human lung tissue that was used for material parameter optimisation. Uniaxial extension on the closed alveolar block simulated materials testing performed on excised lung parenchymal tissue. This acted as confirmation that the stress-strain relationship of the alveolar model was comparable to the stress-strain relationship of the experimental data that was used to parameterize the strain energy function. The

closed alveoli and alveolar/duct models had similar stress-strain relationships, although the alveolar/duct model showed slightly higher total compliance under uniaxial extension.

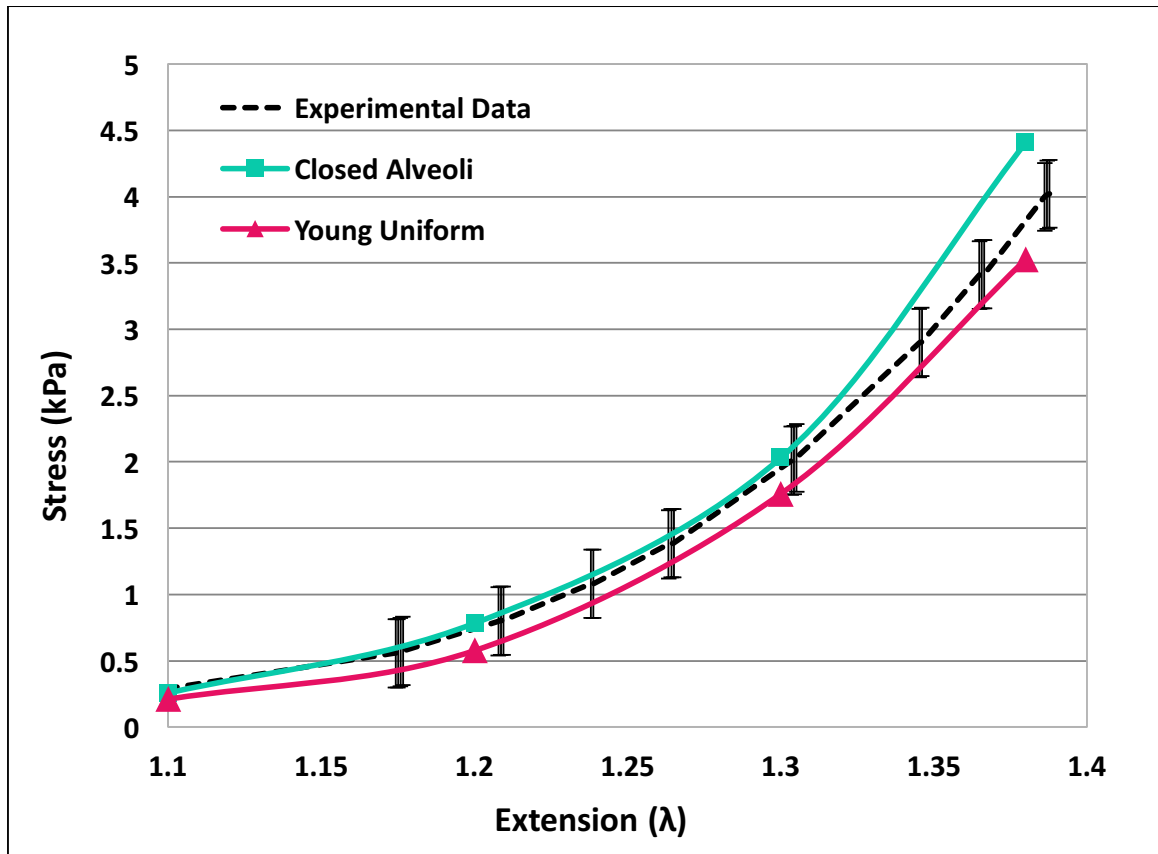


Figure 3.2. The stress-strain relationships for uniaxial extension of two geometric models of the alveolar tissue. Experimental data from Gao et al. (35) is compared with uniaxial extension of the closed alveoli model and the ‘young’ alveolar/duct model with uniform distribution of material properties. Simulations were performed without an initial inflation or internal air pressure, to represent the experimental protocol during materials testing on excised tissue.

Figure 3.3 compares the uniaxial stretch characteristics of the 'young' and 'old' alveolar/duct models. In this case uniaxial extension was simulated for both uniformly and non-uniformly distributed material properties. The models representing alveoli in younger lung tissue had approximately twice the magnitude of stress at each uniaxial strain compared with the older lung geometries. Introducing non-uniformity in the material properties of the septal wall (20% less stiff than baseline) and alveolar mouth (20% more stiff than baseline) increased the total tissue stress on the order of 300-500 Pa for both the young and old models.

The pressure-volume characteristics of the 'young' and 'old' geometries (for uniform and non-uniform material distributions) are given in Figure 3.4. The pressures reported are those for isotropic volume expansion. Expansion is shown relative to the reference/stress-free volume (which is scaled to 1 on the vertical axis). The dashed lines indicate the lower and upper bounds of the range pressure-volume curves can span. These correspond to pressure-volume curves for 20- and 60-year old lungs using the pressure-volume relationship given by Niewoehner et al. (80), and using their age-dependent functions for the parameters of the pressure-volume relationship. The models show an approximately linear rapid increase in volume with pressure over an initial pressure range (up to ~500 Pa for the old models, and ~1500 Pa for the young models), followed by a more gradual increase in volume with pressure. The old model geometries are more compliant than the young models over the initial pressure range. Consistent with Figure 3.3, non-uniform distribution of material properties between the alveolar mouth and wall decreases the compliance of the tissue block; this is apparent in both the young and old models.

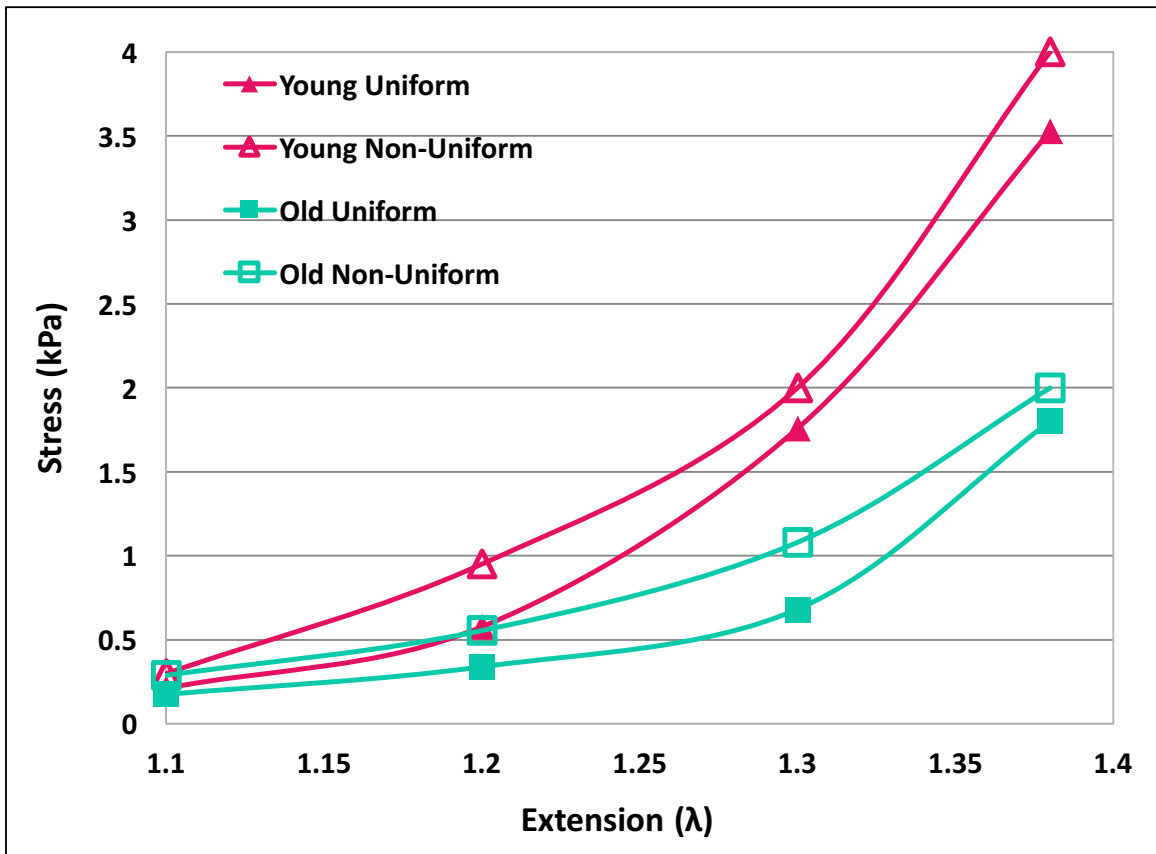


Figure 3.3. Comparison of uniaxial extension between the ‘young’ and ‘old’ alveolar/duct models. Results for both models are shown for uniform and non-uniform distributions of material properties.

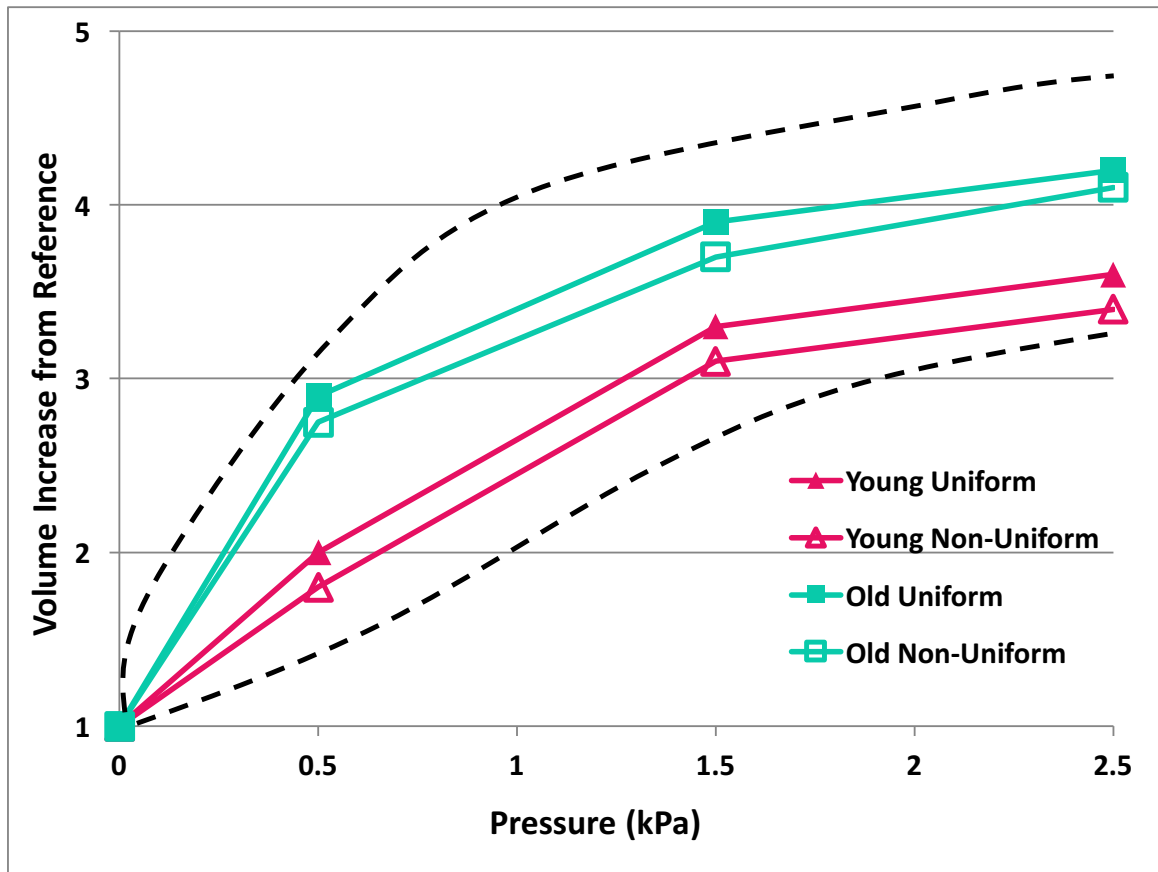


Figure 3.4. Pressure-volume characteristics for four alveolar/duct models: the ‘young’ and ‘old’ alveolar/duct geometries, with each model configured to have uniform and non-uniform material properties. The dashed lines show the upper and lower limits that the pressure-volume curves are expected to span based on the equation used by Niewoehner et al. (80). The vertical axis shows volume as a proportion of initial (reference) volume.

Model shear modulus increased with inflation pressure and older age, consistent with reported trends in the literature. Figure 3.5 compares the model-predicted shear responses with experimental data from Lai-Fook and Hyatt (55) for subjects aged 20 and 60 years. Non-uniform distribution of material properties caused a reduction in the shear moduli over the range of inflation pressures, for both model geometries.

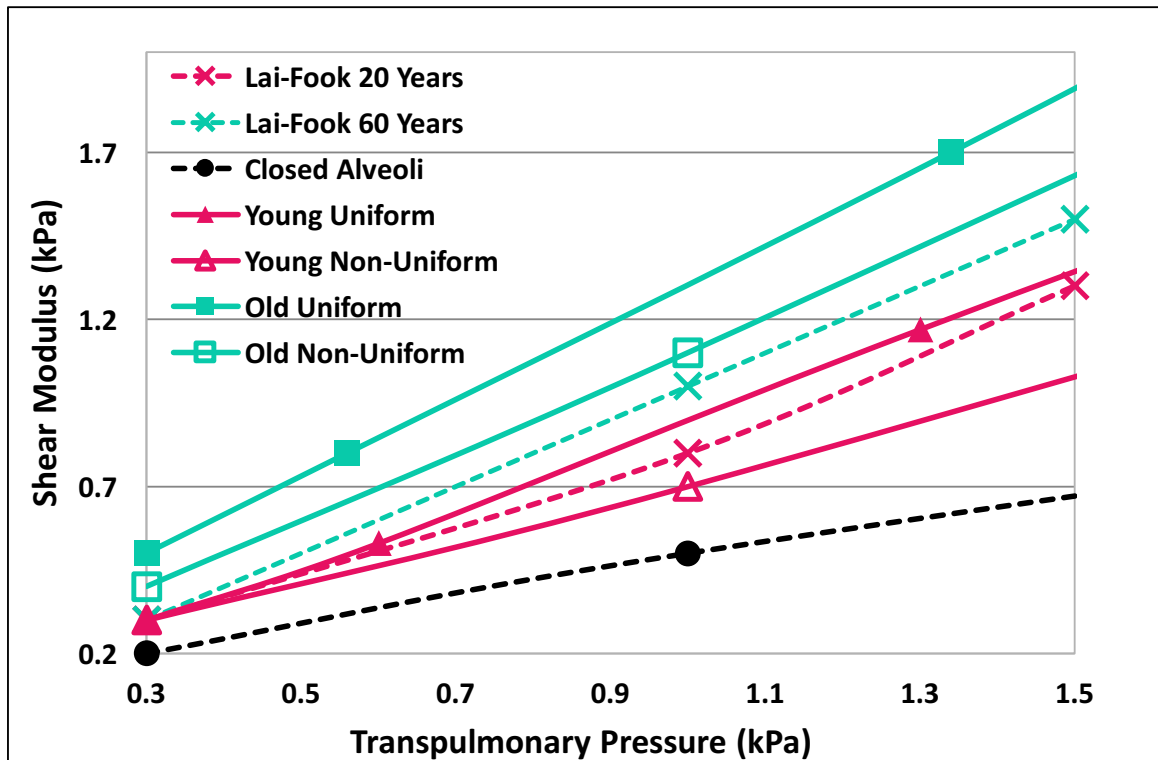


Figure 3.5. Shear modulus against pressure for alveolar tissue block models with tissue properties parameterised to human data (Gao (35)). Models include ‘young’ and ‘old’ alveolar/duct geometries, and each model was configured to have both uniform and non-uniform material property distributions. Experimental shear modulus data are reproduced from Lai-Fook (55) for 20 and 60 year old lungs.

Figure 3.6 illustrates the models’ bulk modulus (K) characteristics. K was calculated directly from the models’ P-V data. The results show an increase in K with age; this is consistent with the behaviour reported by Lai-Fook and Hyatt, however the magnitude of the difference is smaller, particularly at lower inflation pressures. For both model geometries, non-uniform distribution of material properties caused an increase in K . This effect, however, was very minor compared to the difference in K caused by morphometric differences.

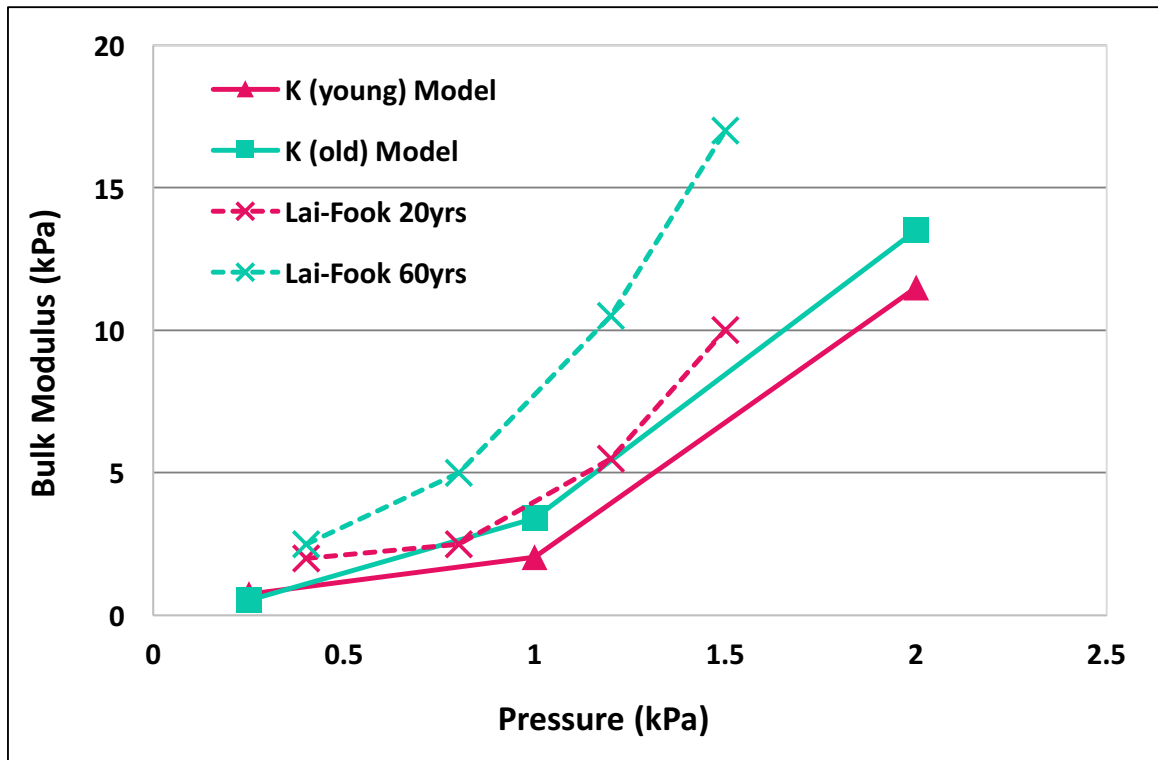


Figure 3.6. Bulk modulus against tissue recoil pressure. Data is shown for the models and the calculated values reported by Lai-Fook and Hyatt (55). Bulk modulus increased with age in the models, consistent with experimental results. In the models with non-uniform material property distributions bulk modulus increased slightly (not shown), although this effect was very minor compared to the changes caused by morphometric differences.

Figure 3.7 shows the stress distribution across the internal faces of several alveoli in the young and old alveolar/duct models, with uniform and non-uniform material property distributions, for pressure expansion to 495 Pa (5 cmH₂O). The stress distributions in the models with uniform distribution of material properties (left-hand panels, A and C) were more spatially uniform than in the models with non-uniform material property distributions (right-hand panels, B and D). For all four models, stress near the alveolar mouth was higher than in the septa. The difference between

septal and alveolar mouth stress was largest for the two models with non-uniform distribution of material properties, and largest overall for the old alveolar/duct model.

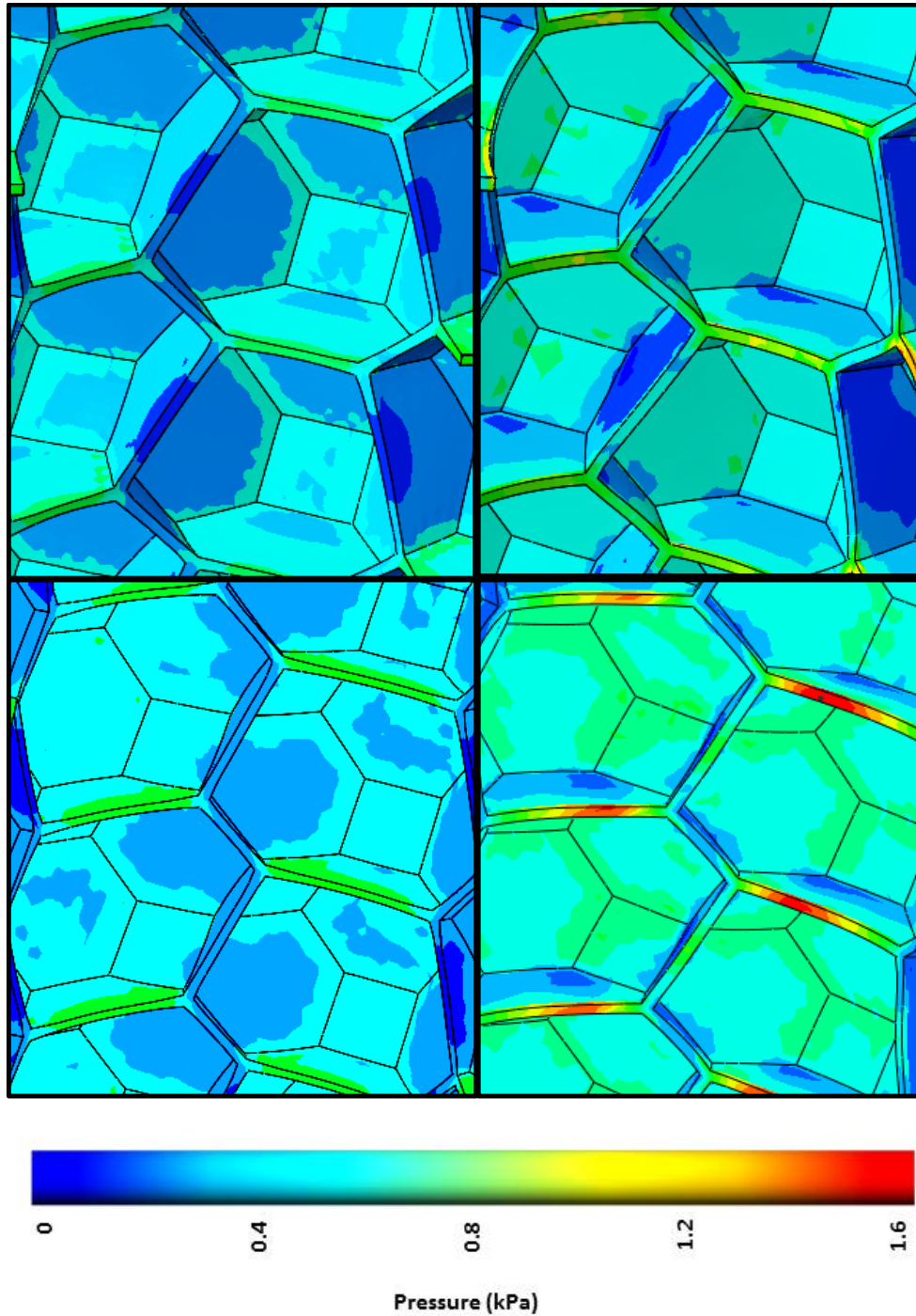


Figure 3.7. Internal views of the relative stress distributions of four alveolar/duct models at an inflation pressure of 495 Pa (5 cmH₂O). The models are: top left – young with uniform material distribution; top right – young with non-uniform material distribution; bottom left – old with uniform material distribution; and bottom right – old with non-uniform material distribution. The colour scale shows stress in kPa.

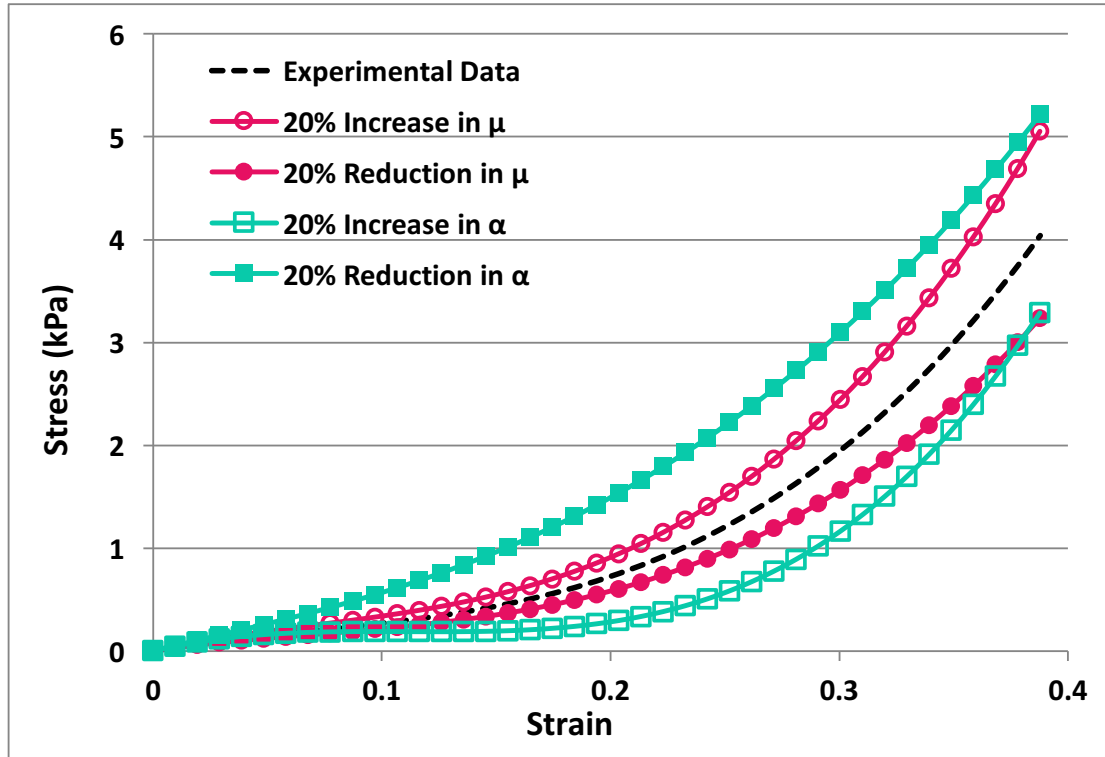


Figure 3.8. Sensitivity analysis for the 3rd order Ogden function. μ and α were varied by 20% above and below their optimised values to change the stiffness of the material in the young alveolar/duct geometric model with uniform material distribution. When each parameter was varied, all other parameters were kept at their baseline values.

Figure 3.8 shows the family of curves from the sensitivity analysis of the material law. The ‘Experimental Data’ line shows the Ogden function for the original coefficients from the optimization (Table 3.2). This behaviour was also exploited in prescribing the non-uniform material properties. The magnitudes of μ and α have opposite effects on the stress-strain behaviour of the material. At maximum strain a 20% reduction in μ resulted in an 18.3% decrease in stress (751 Pa; 7.58 cmH₂O), while 20% increase in μ gave an increase of 29.3% (1176 Pa; 11.98 cmH₂O). Conversely, increase in α of 20% resulted in a decrease in stress of 18.1% (741 Pa;

7.48 cmH₂O), and a decrease in α resulted in an increase in stress of 29.4% (1189 Pa; 12.1 cmH₂O).

3.4 Discussion

Alveolar airspace enlargement and loss of lung elastic recoil pressure are characteristic of the older lung, however the relationship between the two remains poorly understood. Previous micromechanical studies have typically compared the mechanics of normal tissue with pathology (15, 20-24, 36, 51, 97). In this study we used similar models to highlight the differences that age-related morphology and protein distribution could have on lung alveolar mechanics. The specific goals of this study were to determine whether lung tissue-level stress-strain behaviour is sensitive to the geometric changes to the lung's microstructure that typically accompany ageing, and/or to non-uniform distributions of the tissue's stress bearing components. The mechanics of composites of alveoli and alveolar ducts - representing 'young' and 'old' adult alveolar tissue - were compared under planar stretch, under volumetric expansion over a physiological range of inflation pressures, and under shear. Our results suggest that alveolar airspace enlargement can decrease the lung elastic recoil pressure (increase apparent lung compliance when calculated using the pressure-volume curve); and this can occur in the absence of any change to the elastic properties of the individual alveolar walls. Airspace enlargement in our study was also associated with increased shear and bulk moduli, which is consistent with literature descriptions of their age-dependent increase (55).

Alveolar airspace enlargement in our older model was represented by enlargement of the diameter of the alveolar duct, without enlargement of the outer diameter of the model (the duct plus alveolar sleeve). This assumption is consistent with literature

descriptions of dilatation of the ducts and flattening of alveoli in older humans (19) and rats (52, 74, 122). Weibel (116) observed that ducts increase disproportionately in size with old age, occupying a larger fraction of the overall lung volume in an old lung than in a young lung. Mizuuchi et al. (74) also reported definite ductectasia in old rats, with no significant alveolar wall destruction. They noted a statistically significant increase in duct volume in old-age, along with a statistically significant decrease in alveolar volume. Mean linear intercept (L_m) (7, 112) in the young and old alveolar/duct models was $L_m = 236 \mu\text{m}$ and $342 \mu\text{m}$, respectively. This increase in L_m with age is consistent with the literature (98).

The models used in this study represent one closed alveolar duct surrounded by alveoli that open onto the duct. Material test simulations presented here were performed by stretching along the long-axis of the duct, however an excised strip of tissue would contain many ducts oriented in seemingly random directions. Simulations were therefore also performed along the orthogonal axes (to the long-axis of the duct) in order to determine whether the orientation of the stretch with respect to the duct would need to be accounted for in the study. The resulting stresses (results not shown) did not differ significantly between the stretch orientations. The configuration (non-uniformity) of material properties and inflation volume of the alveoli influenced model behaviour to a much greater extent. This suggests that the conclusions from this study would be similar if we were to use a model with dimensions of a tissue strip that was constructed from many randomly oriented alveolar/duct 'base units'; however, this remains to be confirmed.

We first tested the model by comparing its behaviour with the stress-strain data from which it was parameterised. While the outcome of this might at first seem to be pre-

determined, in fact it was not clear: the data was for biaxial stretch of a tissue strip, whereas the model used this data to parameterize the mechanics of the individual alveolar septae. The response of the model tissue to stretch therefore also depended on its geometry, which comprised interdependent alveoli and a high proportion of air. The different model geometries for the 'young' alveolar tissue (closed, and alveolar/duct) gave different stress-strain results (Figure 3.2), but both were within a standard deviation of the mean of the experimental data. This difference in stretch behaviour highlights the sensitivity of the composite tissue to the geometric structure of the alveoli and ducts. This was further apparent in the 'old' lung tissue models, where alveolar duct dilation and shallowing of the alveoli resulted in lower stress at all strains, compared with the 'young' tissue models (Figure 3.3). That is, at any given stress the old alveolar/duct models were stretched considerably more than the young alveolar/duct models. This supports the notion that the geometric changes associated with alveolar airspace enlargement contribute to the decline of lung elastic recoil pressure. That there is a direct relationship between alveolar/duct geometry lung elastic recoil pressure has previously been proposed based on experimental studies. For example, Simon et al. (92) proposed that loss of recoil pressure is secondary to differences in structure of alveolar ducts rather than changes in surfactant function or elastin or collagen content, based on their studies in mice with airspace enlargement.

We also confirmed that the pressure-volume behaviour of the models was consistent with the literature, with the models showing a rapid initial increase in volume with pressure, and a decline in the rate of expansion as pressure increased. The old alveolar/duct model was considerably more compliant in the initial inflation (up to 0.5 kPa) than the young alveolar/duct model, when compliance was calculated from the

pressure-volume curve. If we simplistically assume that functional residual capacity (FRC) is at a recoil pressure of approximately 5 cmH₂O (about 0.5 kPa) then the old tissue was on the order of 1.5 times larger in volume than the young tissue at the FRC pressure. Of course this neglects any interaction with the chest wall, which can also be affected by age. Neglect of the chest wall will also contribute to the large difference in volume of the young and old models as they approach the highest inflation pressure. We note that we do not expect that this model will accurately predict the entire pressure-volume curve as the tissue model does not account for other phenomena that are important in whole lung mechanics, such as airway and/or tissue recruitment and derecruitment, and surfactant dynamics.

Lai-Fook and Hyatt (55) measured increased shear modulus (G) with age, finding that as the lung ages it becomes more resistant to shear. This behaviour was also demonstrated in the models considered here; the old alveolar/duct model had higher G than the young model, and both showed increase in G with inflation pressure. Lai-Fook and Hyatt postulated that in the absence of age-related changes to surfactant, the increase in G could be due to a change in alveolar configuration. Our study's findings support this. Lai-Fook and Hyatt (55) also reported an increase in bulk modulus (K) with age, implying a stiffer lung with respect to the current volume. Our model also shows this behaviour (Figure 3.6), however with a far smaller magnitude of difference between the models than was seen in the data.

The models therefore show the same general age-related differences as experimental data: a more compliant older lung tissue over the full range of inflation, along with higher G and K. The differences in K and G emerge in the absence of a change in the material properties of the alveolar wall, therefore the differences are

attributable to the specific topology of the age-dependent models. We do reiterate though that the difference in K with age is small in our model. As shown by Suki and Bartolák-Suki (98), cross-linking of elastic proteins would further stiffen the alveolar wall of the older tissue, hence increasing the difference in K. It is also likely (and expected) that the model does not capture all of the important mechanisms – such as interaction with the chest wall and tethering to non-alveolar structures - that contribute to the age-dependent differences that are measured experimentally.

In each test (planar stretch, volume expansion) a non-uniform distribution of material stiffness resulted in an overall stiffer tissue in comparison to the uniform case. For the non-uniform distribution only a 10 μm 'ring' at the alveolar mouth was stiffened by 20%, and the remainder of the surface was 20% less stiff. The stiffer alveolar mouths resulted in higher stress in that region during pressure inflation (Figure 3.7), with highest stress in the old alveolar/duct model. Increasing elasticity in this very small region of tissue while making the rest of the alveolar septa less elastic resulted in an overall small increase in the elastic recoil pressure of the tissue, and decrease in resistance to shear. It appears that the normally high density of elastic proteins (elastin in particular) around the alveolar mouths ensures high elastic recoil, whereas the lower density in the alveolar wall gives a tissue that is less resistant to shear (in comparison to a tissue with uniformly distributed elastin and collagen).

The size of the alveolar mouth region for the non-uniform elasticity study was chosen for consistency with Mercer and Crapo (71), whereas the 20% change in stiffness values was arbitrary. The total 40% difference in stiffness between the alveolar mouth and septal wall stiffness is probably conservative, when considering the distribution of elastic fibre density in Mercer and Crapo's study of rat and human

lungs. The authors showed on the order of 15-20% of the elastic fibres within the first 10 μm from the alveolar duct, and the remainder distributed approximately evenly across the rest of the septal wall. Our results suggest that redistribution of elastin and collagen fibres in older age - away from the alveolar mouth and towards the septal wall - while maintaining their total content, would result in a reduction in tissue elastic recoil. The specific distributions of elastin and collagen in the alveolar tissue are therefore key information for understanding how age-dependent pathology that impacts on tissue elastic recoil - such as emphysema - differs from normal ageing.

Redistribution of elastic proteins away from the alveolar mouth (adjacent to the duct) in older age has been proposed to cause dilation of the alveolar duct and shallowing of the alveoli. Our results suggest that this airspace enlargement contributes to loss of tissue elastic recoil in the older lung. Tissue elastic recoil is also lower when the stiffness of the alveolar walls and mouths is the same, as would be the case if the elastic proteins redistributed from the alveolar duct wall to the septae. That is, our study supports that both the cause (redistribution of elastin and collagen) and the structural effect (alveolar airspace enlargement) contribute to decline in lung tissue elastic recoil in older age.

3.4.1 Study Limitations

Total lung elasticity comprises contributions from tissue elasticity and surface forces (with their modification by surfactant). The interaction of tissue elasticity, surface forces, and geometry is essential for a comprehensive understanding of alveolar tissue micromechanics. However, correctly modeling the surface forces and tissue mechanics within a three-dimensional modeling framework remains a challenge that

neither we nor others have yet resolved. In the current study we ignored the distinct contributions of tissue elasticity and surface forces, by assuming a single material law that lumped these components together. This simplification would only impact on the interpretation of our studies if the surface forces were significantly different between the young and old alveolus. The radius of curvature of alveoli in both models was the same, hence the surface forces per unit area were the same. Although experimental studies have noted changes in the immunological composition of the alveolar lining liquid (76), there is no current evidence that supports a difference in surfactant function as it relates to tissue elasticity. These two points support the use of a lumped phenomenological material law as an approximation in the current study. However, we note that if the radius of curvature is significantly different with age then this would support the development of a model that differentiates the surface forces from tissue elasticity.

The material law was parameterized to the average stress-strain relationship measured for excised slices of lung tissue. Gao et al. (35) included tissue from males and females, with an age range of 44 – 82 years. In the experimental study tissue samples were submerged in saline, after which they were frozen and cut into strips with an average dimension of 5 cm x 5 cm x 0.4 cm. Only samples without large airways or blood vessels were used. The method of tissue preparation in this study means that the measured tissue mechanics does not represent the normal contribution of surface forces (including surfactant dynamics). This limitation is typical of lung tissue strip experiments, and will contribute to the variability of experimental data as highlighted by Rausch et al. (87). It is also not clear whether the tissue strip preparations should be more compliant than *in vivo* tissue (surface forces abnormally low, e.g. as in saline filled) or less compliant (e.g. air-surface liquid

interface present, but without decrease in surface tension by surfactant). Our parameterization of the mechanics of the individual alveolar septal wall to the stress-strain behaviour of a tissue preparation is also less than ideal as the tissue preparation mechanics represents the interaction of tissue elasticity with alveolar geometry. Ideally we would model the detail of the distribution of elastin and collagen fibres and their stress-strain behaviour.

We parameterised the material law to the average of the Gao et al. (35) data. We could have parameterized the young and old models to age-specific data from this study, however as noted previously, the composite behaviour of the tissue is a result of interaction between tissue elasticity and geometry; using the same material law for all of our models allowed us to separate the role of geometry from other mechanisms.

The relatively complex geometry of the models required a third order Ogden function in order to ensure convergence of the simulations. First and second order Ogden functions were also tested (results not shown). These were found to be adequate to fit the experimental data but inadequate for simulation purposes. Adequacy of the different order functions was evaluated using the optimiser tools provided by Abaqus, whereby the first and second order functions were deemed unstable (i.e. did not guarantee convergence for uniaxial and shear deformations). When the first and second order functions were used to simulate tissue deformation, no solution could be reached as some parts of the models proved too geometrically complex for numerical convergence.

To summarize the study limitations, the current method uses a pragmatic approximation for the material law with parameterization to tissue strip experiments,

in lieu of a detailed model of the interaction between tissue elasticity and surface forces (along with the data that would be required to parameterize this model). Therefore, despite the quantitative consistency of the model results with data from the literature, the models presented in this study should primarily be considered for their relative behaviour; i.e. qualitatively rather than quantitatively.

CHAPTER 4

THE IMPACT OF AGE-RELATED CHANGES ON LUNG MECHANICS: LINKING PRESSURE-VOLUME AND PARENCHYMAL PROPERTIES TO TISSUE DEFORMATION

4.1 Introduction

Altered density and heterogeneity of lung soft tissue often accompany physiological changes. This may occur as a normal part of ageing, or may be an indicator of disease. In both scenarios the lung's mechanical behaviour is affected. At the whole-organ scale the quasi-static pressure-volume (P-V) curve can be used to infer the elastic properties of the lungs (114), however this does not provide sufficient information to distinguish between the changes that occur purely as a result of ageing, and early changes associated with pathology.

As a step towards linking the micro- and macro-scale mechanics of the lung, Denny and Schroter developed an alveolar model using closed truncated octahedra to form a space-filling 'cube' on which non-isotropic distortions could be simulated (22). They confirmed that a linear constitutive model is only suitable for analysing small isotropic deformations of the microstructure, and when considering lung parenchyma on a whole-lung scale the deformations must be considered large and non-linear. Thus

they and others conclude that simply 'scaling up' an alveolar model is not adequate to describe the P-V behaviour of a full lung. Linking the lung's macroscopic behaviour to its microscopic constituent components has therefore proven difficult (94, 101), and as a result current understanding of the complex interactions between lung tissue structure and function is incomplete. Studies that seek to predict lung tissue displacement during breathing (26) or during gravitational deformation due to posture (104) therefore rely on fitting linear elastic models or use phenomenological models for the stress-strain relationship of the lung tissue, respectively.

A number of phenomenological models have previously been used to describe lung mechanics, such as Fung's exponential law (33) and the polynomial strain energy density function (SEDF) parameterised by Lee and Frankus (61) to data from uniform expansion of excised dog lung tissue. Such models treat lung parenchymal tissue as a continuum and do not attempt to relate to the tissue microstructure. They do, however, present the advantage of being able to simulate tissue deformation at the whole-organ scale, and they can potentially be parameterized using data from 4D-CT (computed tomography) (26), measured whole-lung P-V curves, and supplemented with microstructural data. The primary goal here is to determine whether a phenomenological model that is informed by measured quasi-static whole lung mechanics (the P-V curve) and experimental data (separately acquired material shear test data) can be predictive of imaged regional tissue deformation. If successful, this would provide a convenient approach for predicting tissue displacement during postural change and lung inflation, without requiring invasive measurements. A secondary goal is to evaluate whether this approach can be used to derive a SEDF that reflects age-dependent changes to shear modulus and the P-V relationship.

4.2 Methods

A non-linear multiple-optimization algorithm was derived to parameterize the coefficients in a polynomial SEDF. In the current study lung pressure-volume (P-V) data from mechanically ventilated animals and published shear modulus data for adult human lung tissue (55) were used as inputs to the optimization method. The parameterized SEDF was used to simulate lung tissue deformation under gravity loading (104). Multi-detector row (MDCT) imaging was used to define the model geometries and to validate the tissue deformation results. Figure 4.1 provides a summary of the optimization and validation process, and further detail is given in the following sections.

4.2.1 Subject Data

Imaging and P-V data from pigs were used for this study. The study protocol was approved by the University of Iowa Institutional Review Board and Animal Ethics Committees. The subjects were four healthy young adult pigs of both genders (2 male, 2 female), with weights ranging from 20 kg – 40 kg. This data was used in a prior study, which provides further detail on the animal preparation and imaging protocol (62). The lungs were imaged *in vivo*, in the prone position. Imaging was acquired during breath-hold, with the lungs held at fixed positive end-expiratory pressure (PEEP), at three different PEEP levels: 'low' (490 Pa/ 5 cmH₂O to 920 Pa/ 9.4 cmH₂O), 'medium' (1470 Pa/ 15 cmH₂O), and 'high' (2450 Pa/ 25 cmH₂O). The variation in low PEEP values was because this was set at the lowest level that avoided development of atelectasis, and this was variable between subjects.

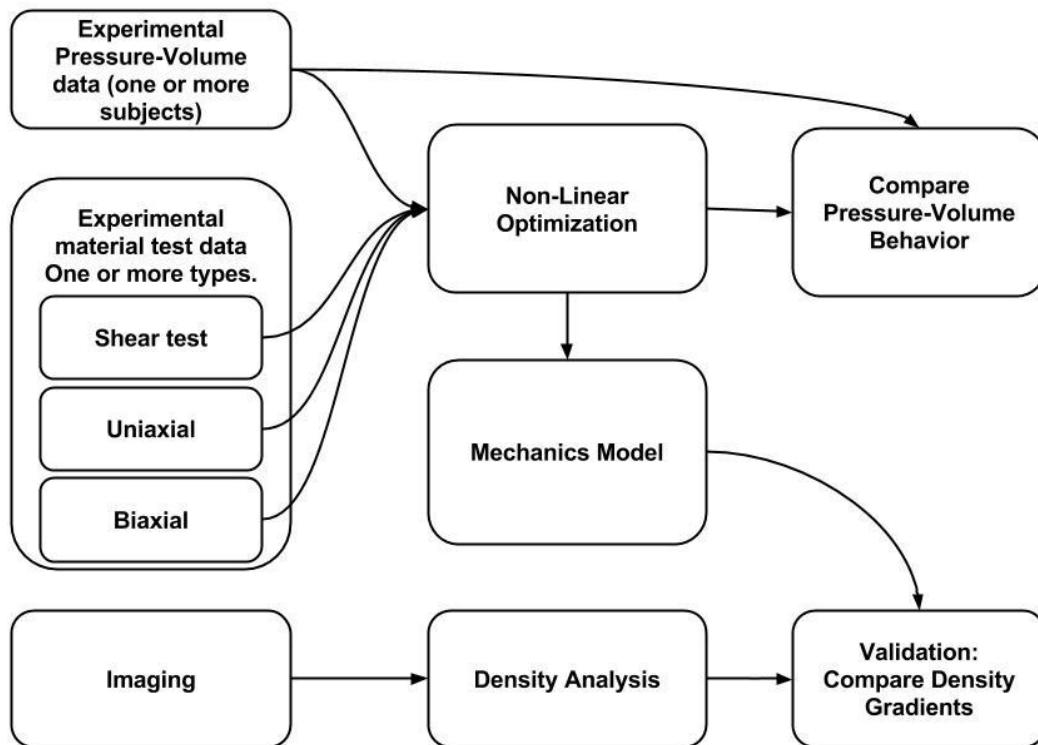


Figure 4.1: Schematic summarizing the method for parameterizing a stress-strain relationship, and simulating tissue displacement. Material properties (shear modulus) and pressure-volume data were used as inputs to a non-linear optimization method. The tissue density gradient from the mechanics model was compared to the density distribution from imaging for validation.

A dual x-ray source spiral MDCT scanner (Siemens Medical Systems, Erlangen, Germany) was used to image the lungs at each of the inflation pressures. Image slice spacing was 0.5 mm, resulting in 500-800 slices per volumetric image. Each slice image had physical in-plane resolution ranging from 0.50 mm/pixel to 0.70 mm/pixel. Table 4.1 lists each animal's inflation pressures along with the corresponding lung volumes that were reconstructed from the volumetric imaging.

Table 4.1: Pig lung positive end-expiratory pressures and corresponding lung volumes (air plus tissue), for animals oriented prone.

Subject	Inflation pressure kPa (cmH₂O)	Volume litres	Mean density g/cm³
1	0.92 (9.4)	1.41	0.26
1	1.47 (15)	1.67	0.22
1	2.45 (25)	1.93	0.18
2	0.49 (5)	1.24	0.31
2	1.47 (15)	1.89	0.24
2	2.45 (25)	2.14	0.21
3	0.74 (7.5)	1.78	0.43
3	1.47 (15)	2.29	0.29
3	2.45 (25)	2.50	0.22
4	0.49 (5)	1.55	0.39
4	1.47 (15)	2.18	0.33
4	2.45 (25)	2.51	0.21

4.2.2 Parameterization of the SEDF

The P-V data from Table 4.1 and published shear modulus data for lung tissue from human adults (55) were used as material property constraints in a parameter estimation for a polynomial SEDF of the form used by Lee and Frankus (61). In the absence of material test data on young or old pigs, human data was used. The initial set of parameterizations used P-V and shear modulus values for a young adult lung (20 years). Further parameterizations were then performed to investigate the effects on tissue deformation of changes to P-V curve and shear modulus by using values that reflected an older lung (60 years old). Parameterizations were therefore performed for four combinations: P-V(20 year old)+shear(20 year old), P-V(20 year old)+shear(60 year old), P-V(60 year old)+shear(20 year old), and P-V(60 year old)+shear(60 year old).

The general form of the polynomial SEDF is

$$W = a_1 I_1 + a_2 (I_1^2 - 2I_2) + a_3 (I_1^3 - 3I_1 I_2 + 3I_3) + a_4 (I_1^4 - 4I_1^2 I_2 + 2I_2^2 + 4I_1 I_3) + b_1 I_2 + b_2 (I_2^2 - 2I_1 I_3) + c_1 I_3 + c_2 (I_1 I_2 - 3I_3) + c_3 (I_1^2 I_2 - 2I_2^2 - I_1 I_3), \quad (4.1)$$

where the coefficients a_i , b_i , c_i , ($i=1..4$) have units of pressure, and I_i ($i=1..3$) are the invariants of the right Cauchy-Green deformation tensor. A double optimization process was designed for estimating values of a_i , b_i , c_i , using multidimensional unconstrained nonlinear minimization (82). The method was implemented in MATLAB (version 2010a, The MathWorks Inc.). The optimization process was designed to estimate values for the coefficients in equation (4.1), however we note that the method is not restricted to this SEDF: other functions can readily be substituted.

The optimization process sought to concurrently minimize two objective functions. The first was the absolute error between experimental P-V data and a derived expression for the relationship between pressure and volume in the model. The second was the absolute error between shear modulus data and a derived expression for shear modulus from the model. The objective functions used input data that expressed the elastic recoil pressure as a function of strain, and shear modulus as a function of elastic recoil pressure.

Analytic expressions for the P-V relationship during isotropic expansion and the pressure-dependent shear modulus can be derived from the finite deformation elasticity tensors. The expressions were derived as follows. Taking F as the deformation gradient tensor, C as the right Cauchy-Green deformation tensor, and λ as the stretch relative to the reference volume, then for an isotropic expansion, F and C are given by:

$$F = \begin{bmatrix} \lambda & 0 & 0 \\ 0 & \lambda & 0 \\ 0 & 0 & \lambda \end{bmatrix} \quad (4.2)$$

$$\text{and } C = F^T F = \begin{bmatrix} \lambda^2 & 0 & 0 \\ 0 & \lambda^2 & 0 \\ 0 & 0 & \lambda^2 \end{bmatrix} \quad (4.3)$$

The invariants of C become:

$$I_1 = \text{tr}(C) = 3\lambda^2, \quad (4.4)$$

$$I_2 = \frac{1}{2}[(\text{tr}C)^2 - \text{tr}(C^2)] = 3\lambda^4, \quad (4.5)$$

$$\text{and } I_3 = \det(C) = \lambda^6; \quad (4.6)$$

and their derivatives with respect to C are:

$$\frac{\partial I_1}{\partial C} = 1, \quad (4.7)$$

$$\frac{\partial I_2}{\partial C} = \frac{1}{2}(I_1 I - C^T), \quad (4.8)$$

$$\text{and } \frac{\partial I_3}{\partial C} = I_3 C^{-1}. \quad (4.9)$$

An elastic recoil pressure (P) for isotropic expansion can be estimated as:

$$P = \frac{S_{ii}}{\lambda} \quad (4.10)$$

where S_{ii} is the Cauchy stress, given by:

$$S_{ii} = 2 \frac{\partial W}{\partial C} = 2 \left[\frac{\partial W}{\partial I_1} \frac{\partial I_1}{\partial C} + \frac{\partial W}{\partial I_2} \frac{\partial I_2}{\partial C} + \frac{\partial W}{\partial I_3} \frac{\partial I_3}{\partial C} \right]. \quad (4.11)$$

The partial derivatives of W (equation 4.1) are:

$$\begin{aligned} \frac{\partial W}{\partial I_2} = & a_1 + 2a_2 I_1 + 3a_3 I_1^2 - 3a_3 I_2 + 4a_4 I_1^3 - 8a_4 I_1 I_2 \\ & + 4a_4 I_3 + 2b_2 I_3 + c_2 I_2 + 2c_3 I_1 I_2 - c_3 I_3 \end{aligned} \quad (4.12)$$

$$\frac{\partial W}{\partial I_2} = -2a_2 - 3a_3 I_1 - 4a_4 I_1^2 + 4a_4 I_2 + b_1 + 2b_2 I_2 + c_2 I_1 + c_3 I_1^2 - 4c_3 I_2 \quad (4.13)$$

$$\frac{\partial W}{\partial I_3} = 3a_3 + 4a_4 I_1 - 2b_2 I_1 + c_1 - 3c_2 - c_3 I_1 \quad (4.14)$$

Substituting equations (4.7 - 4.9) and (4.11 - 4.14) into equation (4.10) provides an expression for pressure in terms of λ :

$$P = a_1 \frac{2}{\lambda} + 4a_2\lambda + 6a_3\lambda^3 + 8a_4\lambda^5 + 4b_1\lambda + 8b_2\lambda^5 + 2c_1\lambda^3 + 12c_2\lambda^3 + 16c_3\lambda^5 \quad (4.15)$$

noting that $Volume \propto \lambda^3$. Equation 4.15 was used directly in the optimization process; this is the first of the two equations in the double-optimization problem. An expression for the relationship between simple shear and elastic recoil pressure can also be derived from the finite deformation elasticity tensors. For a simple shear of magnitude μ , F and C are:

$$F = \begin{bmatrix} \lambda & \mu & 0 \\ 0 & \lambda & 0 \\ 0 & 0 & \lambda \end{bmatrix} \quad (4.16)$$

$$\text{and } C = \begin{bmatrix} \lambda^2 & \mu\lambda & 0 \\ \mu\lambda & \lambda^2 + \mu^2 & 0 \\ 0 & 0 & \lambda^2 \end{bmatrix}. \quad (4.17)$$

The invariants of C are therefore:

$$I_1 = 3\lambda^2 + \mu^2, \quad (4.18)$$

$$I_2 = 3\lambda^4 + \mu^2\lambda^2, \quad (4.19)$$

$$\text{and } I_3 = \lambda^6; \quad (4.20)$$

Substituting equations (4.18 – 4.20) into equation 4.1, and differentiating with respect to I_1 , I_2 , and I_3 gives:

$$\frac{\partial W}{\partial I_1} = a_1 + 2a_2I_1 + 3a_3I_1^2 + I_2(c_2 - 3a_3) + 4a_4I_1^3 + 2I_1I_2(c_3 - 4a_4) + I_3(4a_4 - c_3 - 2b_2), \quad (4.21)$$

$$\text{and } \frac{\partial W}{\partial I_2} = (b_1 - 2a_2) + I_1(c_2 - 3a_3) + I_1^2(c_3 - 4a_4) + I_2(4a_4 + 2b_2 - 4c_3) \quad (4.22)$$

Substituting equations (4.8 – 4.9, 4.21 – 4.22) into equation (4.11) gives:

$$S_{12} = \frac{\partial W}{\partial I_2}(-\mu\lambda) + \frac{\partial W}{\partial I_3}(-\mu\lambda^3), \quad (4.23)$$

$$\text{and } S_{22} = \frac{\partial W}{\partial I_1} + \frac{\partial W}{\partial I_2}(2\lambda^2) + \frac{\partial W}{\partial I_3}(\lambda^4) \quad (4.24)$$

Using the relationship:

$$J\sigma_{12} = \lambda^2 S_{12} + \mu\lambda S_{22} \quad (\text{where } J = \lambda^3) \quad (4.25)$$

we get:

$$J\sigma_{12} = \frac{\partial W}{\partial I_2}(\mu\lambda^3) + \mu\lambda \frac{\partial W}{\partial I_1} \quad (4.26)$$

To calculate strain we use the relationship:

$$E_{12} = \frac{1}{2}(\mu + (\lambda - 1)\mu) = \frac{\mu\lambda}{2}, \quad (4.27)$$

$$\text{where if } \mu \ll 1 \text{ then } E_{12} \approx \varepsilon_{12} \approx \frac{\mu}{2} \quad (4.28)$$

Equations (4.27) and (4.28) provide an expression for shear modulus (G):

$$G = \frac{\sigma_{12}}{2\varepsilon_{12}} = \frac{\partial W}{\partial I_2} + \frac{1}{\lambda^2} \frac{\partial W}{\partial I_1}. \quad (4.29)$$

For each subject, a unique set of coefficients for W was optimised to fit that subject's P-V data and to fit shear modulus data as given for a young human adult lung (55). Therefore, the double-optimization sought to minimize the sum of the root mean square errors for G and P. That is,

$$\text{Error} = \sqrt{\sum (P(\lambda)_* - P(\lambda))^2} + \sqrt{\sum (G(\lambda)_* - G(\lambda))^2} \quad (4.30)$$

where $P(\lambda)_*$ and $G(\lambda)_*$ are pressure and shear modulus data, respectively, and $P(\lambda)$ and $G(\lambda)$ are pressure and shear modulus from the model, respectively.

The coefficient values from Lee and Frankus (61) for dog lung tissue were treated as a baseline, and used to initialize the coefficients for the optimization. Lower and upper bounds for the magnitudes of the coefficients were set at zero and twice the magnitude of the baseline values. For example, the parameter a_1 was assigned an initial value of -210 , with a lower bound of -420 and an upper bound of zero. This approach allowed the coefficients to have a wide range over which to converge, while at the same time not allowing a change in sign of the coefficients from the baseline values. To ensure that each error function was converging to a local minimum, the code was run repeatedly with the range between the upper and lower bound constraints varied for each coefficient, and with the initial values varied for each coefficient in turn. In all cases the optimization converged for all of the coefficients.

4.2.3 Finite Element Models and Simulation

Finite element analysis was used to test the performance of the SEDF in predicting the displacement of the lung tissue under gravity loading. A finite element model of the left lung was constructed for each animal. The models consisted of 114 nodes and 78 elements. The lungs were automatically segmented from the volumetric imaging using the custom-built software package PASS (Pulmonary Analysis Software Suite, University of Iowa) (45). A finite element mesh was geometry-fitted to each segmented left lung, using previously described methods (28, 105). Finite strain methods were used to simulate parenchymal tissue deformation under the influence of gravity (104) at each imaged volume. Boundary conditions were prescribed to allow sliding of the lung relative to the chest wall. The chest wall was assumed to have constant shape for simulation at a specific volume. Mesh nodes located along the length of the most posterior and anterior borders were fixed in the gravitational direction only. Figure 4.2 shows finite element meshes for one representative subject left lung at three different volumes.

Soft tissue deformation (104) in the prone posture at successively larger PEEP was simulated in two steps. In the first step the mesh was isotropically expanded from an arbitrary zero-stress reference volume (V_0 - taken as 12.5% of the lung volume at 2.45 kPa (25 cmH₂O)) to the volume corresponding to the desired PEEP as listed in Table 4.1 for each animal. The surface forces required to maintain this configuration were then calculated. Gravity was added incrementally in a second step. The animals were oriented in the prone posture, so gravity was applied in the posterior-anterior direction.

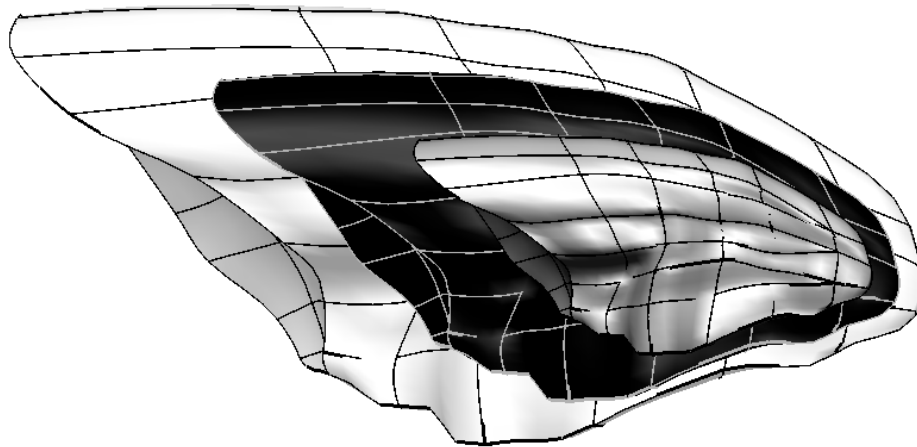


Figure 4.2: Finite element meshes for one representative pig lung at three different levels of PEEP (three different lung volumes); zero pressure at the reference volume (grey), low pressure/low volume (black), and high-pressure/high volume (white). The grey reference volume does not represent a physiological state – it is necessary for the purposes of simulating mechanics.

For comparison with the experimental P-V data, simulation of tissue expansion/deformation was performed for eight incremental volumes (V) per animal, from V_0 to the maximal volume at 2.45 kPa (by definition $8 \times V_0$). For validation of the gravitational deformation of the model, simulations were performed at three PEEP levels per animal (as per Table 4.1) for comparison with the corresponding density distributions from CT imaging (95). Code to calculate the density distributions from imaging was written in MATLAB (version 2010a, The MathWorks Inc.) (96).

Shear modulus was calculated for a model block of tissue at each of the eight incremental volumes as above, for comparison with experimental data from Lai-Fook (55). A finite element model tissue block comprising 128 equal sized elements ($8 \times 4 \times 4$) with tri-cubic Hermite basis functions was first expanded to the required

volume, and the tissue elastic recoil pressure for the expanded volume was calculated. Simple shear was applied to the expanded block by prescribing a tangential displacement of all nodes on one surface of the block. The nodes on the opposite surface were kept fixed, while the nodes on the remaining four faces were allowed to move freely. The resulting stress on the displaced surface nodes in the direction of shear was used to calculate the shear modulus. The magnitude of the prescribed shear was 1% of the total length of the block, along the axis of shear displacement.

4.2.4 Sensitivity to Parameters

A sensitivity analysis was conducted to test each coefficient of the SEDF individually, in order to determine its contribution to the overall stiffness of the material. The same tissue block as was used for the shear modulus simulations was used here. For each test, the block was first expanded isotropically from its reference configuration to a volume at which the recoil pressure was 490 Pa (5cmH₂O). This expansion corresponds to the approximate tissue elastic recoil pressure for a normal intact lung in a young adult at end expiration. Uniaxial extension was simulated following the expansion step. The deformation was implemented by prescribing displacement to all the nodes on one surface at the end of the longest axis of the block, and zero displacement to all nodes at the opposite surface. The nodes on the remaining four surfaces were allowed to move freely. Only one displacement was used in the sensitivity analysis since the intention of this test was to establish the relative influence of each of the coefficients, rather than investigate the relationship between stress and extension.

To provide a baseline for comparison, expansion and uniaxial extension were first simulated using the SEDF with the original coefficients from Lee and Frankus (61) (labeled 'Original coefficients (polynomial)' in Table 4.2). Each of the nine coefficients in the polynomial was then perturbed by +/-10%, while holding the other coefficients constant. For each coefficient change, isotropic expansion and uniaxial extension were simulated, and this process was repeated for each of the nine coefficients.

Following uniaxial stretch, the stress in the direction of stretch was calculated and compared to the stress at the end of isotropic expansion. The fractional difference in stress between the perturbed and baseline SEDF was defined as

$$F_{\sigma} = \frac{\sigma_{22}^* - \sigma_{22}^b}{\sigma_{22}^b}, \quad (4.31)$$

where the superscript '*' denotes the perturbed coefficients, superscript 'b' is for baseline coefficients, and σ_{22} is the stress in the direction of uniaxial extension for each case. The ratio of stresses before and after uniaxial extension for the perturbed SEDF was defined as

$$R_{\sigma} = \frac{\sigma_{22}^*}{\sigma_e}, \quad (4.32)$$

where σ_e is stress in any principal direction following uniform expansion for the perturbed SEDF.

The influence of the extension ratio, λ , on each of the coefficients was evaluated by calculating the power to which λ was raised for that coefficient. For example, the

term involving a_1 is $a_1 I_1$. Using Equation (4), $I_1 = tr(C) = 3\lambda^2$. Thus, the highest power of λ encountered by a_1 is 2.

4.2.5 Grouping Analysis

To determine whether a polynomial SEDF with a reduced number of terms would be effective in simulating lung stress and strain, the terms in the SEDF were grouped by their power of λ . Grouping was performed using the MATLAB symbolic toolbox and resulted in four groups:

$$\begin{aligned}
 & [a_4[\dots] + b_2[\dots] + c_3[\dots]]\lambda_s^6 && \text{(Group 1)} \\
 & + [a_3[\dots] + c_2[\dots] + c_1[\dots]]\lambda_s^4 && \text{(Group 2)} \\
 & + [a_2[\dots] + b_1[\dots]]\lambda_s^2 && \text{(Group 3)} \\
 & + a_1[\dots] && \text{(Group 4)}
 \end{aligned}
 \tag{4.33}$$

Uniaxial extension was then simulated for each group, with the other groups suppressed. That is, when simulating for group 1, a_4 , b_2 , and c_3 retained their optimised values, while the other coefficients were set to zero. This process was repeated four times to isolate and test each group. Uniaxial extension was once again simulated on the cube geometry to quantify the stresses produced using the reduced SEDF expressions. For this test the simulation was repeated for a range of strains in order to make a direct comparison with the stress-strain relationship of the original Lee and Frankus SEDF. Strain was increased to a maximum of 1.4x the original length of the cube.

4.3 Results

The parameterized coefficients resulting from the optimization process for one representative animal are given in Table 4.2. The coefficients converged to similar values for all of the animals (results not shown). The similarity between the experimental and modelled P-V behaviour for each of the four animals is shown in Figure 4.3. RMS errors between the data and model results in Figure 4.3 were <4% for each of the four animals, for data in the range between 500-2500 Pa.

Table 4.2: The optimised coefficients for the polynomial SEDF for one representative animal. The baseline coefficients (from Lee and Frankus) are included for comparison in parentheses.

$a_1 = -100.6$ (-210.6)	$b_1 = 50.1$ (26.7)	$c_1 = 3.8$ (13.2)
$a_2 = 251.4$ (197.6)	$b_2 = -6.9$ (-3.5)	$c_2 = -40.0$ (-19.4)
$a_3 = -74.8$ (-78.8)		$c_3 = 13.1$ (9.4)
$a_4 = 8.8$ (10.6)		

Figure 4.4 compares shear modulus, G , over a range of recoil pressures for the optimised SEDF from the four animals with the experimental data that was used for the optimization (G data for young adult). The figure compares G that was estimated from imposing shear deformation on a finite element ‘tissue block’ model over a range of inflation pressures. The RMS errors in G were <3% for each of the four animals.

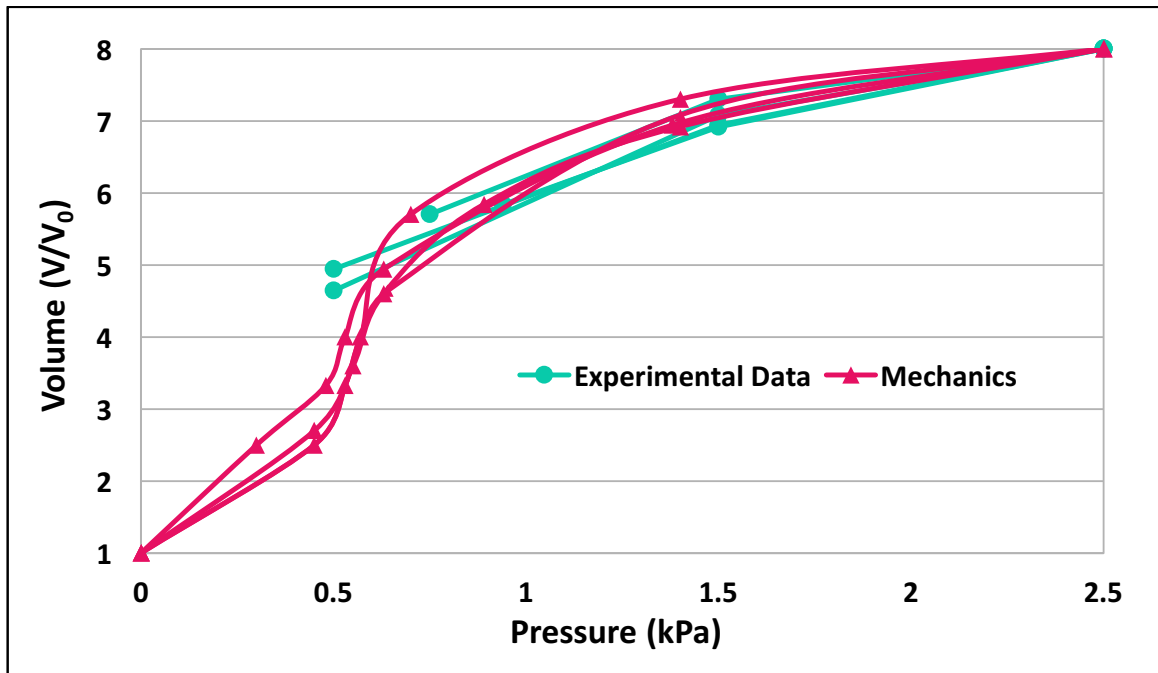


Figure 4.3: Model and experimental P-V curves for all animals. The models used a unique set of coefficients for each animal. Volume is shown as a ratio of the reference volume (assumed to be 12.5% of lung volume at maximum inflation).

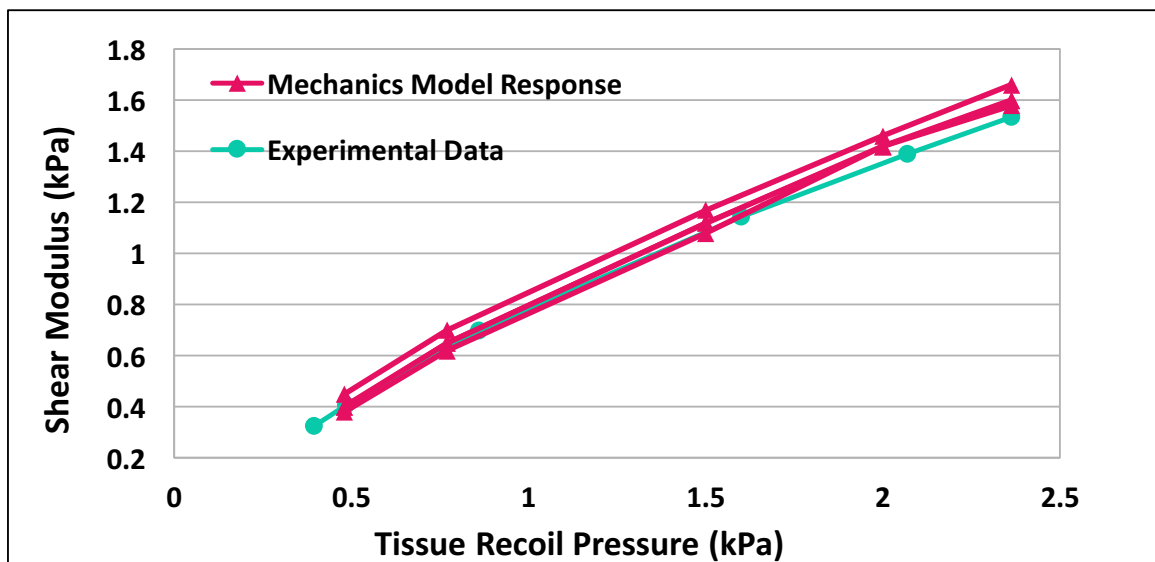


Figure 4.4: Shear modulus calculated from a finite element 'tissue block' model following optimization of SEDF coefficients to each of four animals, compared with data from Lai Fook (55).

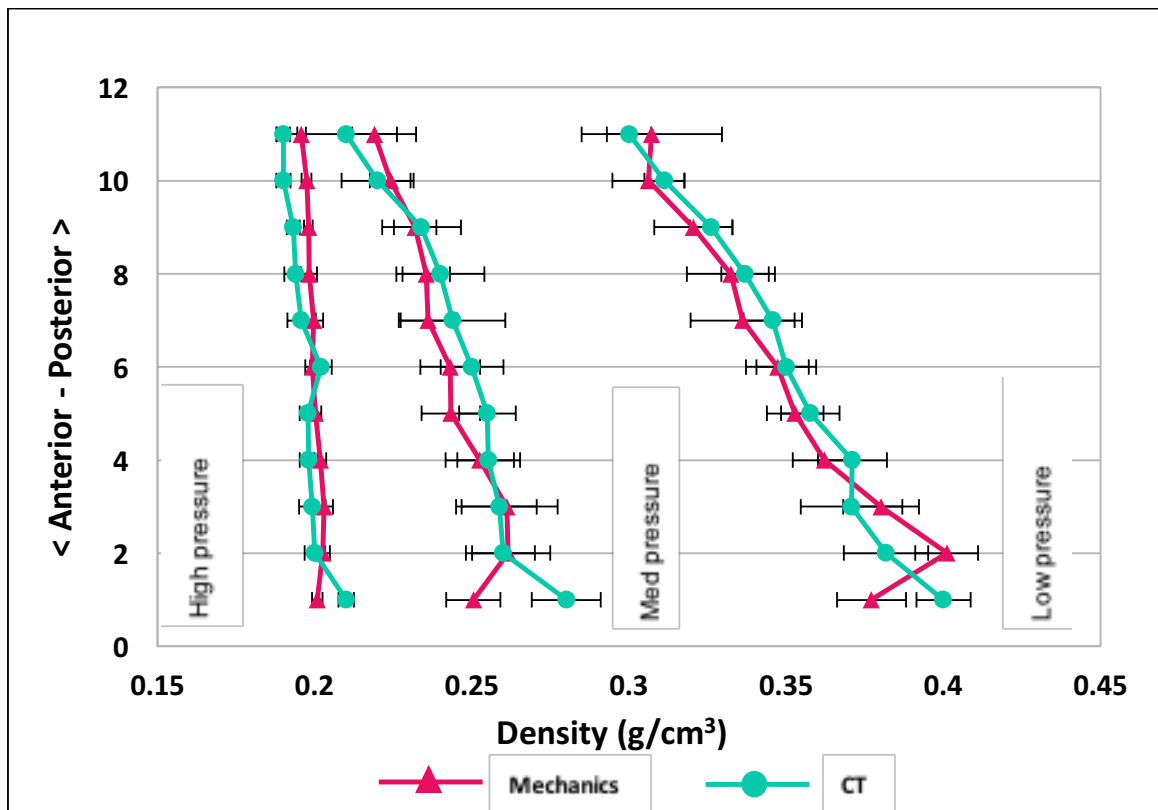


Figure 4.5: Gravitational density profiles for CT imaging and the tissue mechanics model, for each of the inflation pressures. Each line represents the mean of all the subjects for that particular inflation pressure.

Figure 4.5 shows the density distribution along the gravitational (anterior-posterior) axis for all three levels of PEEP. The graph shows the average results from simulation of gravitational deformation of the lung tissue in the four animal models over the range of PEEP, as well as the corresponding density distributions extracted from the CT imaging. As expected, the density of the models decreased with PEEP (i.e. with increased lung volume). The rate of increase of density with distance from the posterior surface decreased with lung inflation, and was consistent between the

model and CT data. T-tests performed for the density gradients gave p-values > 0.05 for all of the subjects at all inflation pressures, suggesting no statistically significant differences between the model and the imaging data.

Table 4.3 lists the difference between model and data for density and pressure in the four animals, summarized as mean \pm S.D. for each inflation volume. The difference in density and pressure both decrease with increasing inflation volume. Table 4.3 also lists the minimum p-value calculated for any subject for a t-test comparing the imaging and model tissue density gradients. In all cases, there was no statistically significant difference between model prediction and imaging.

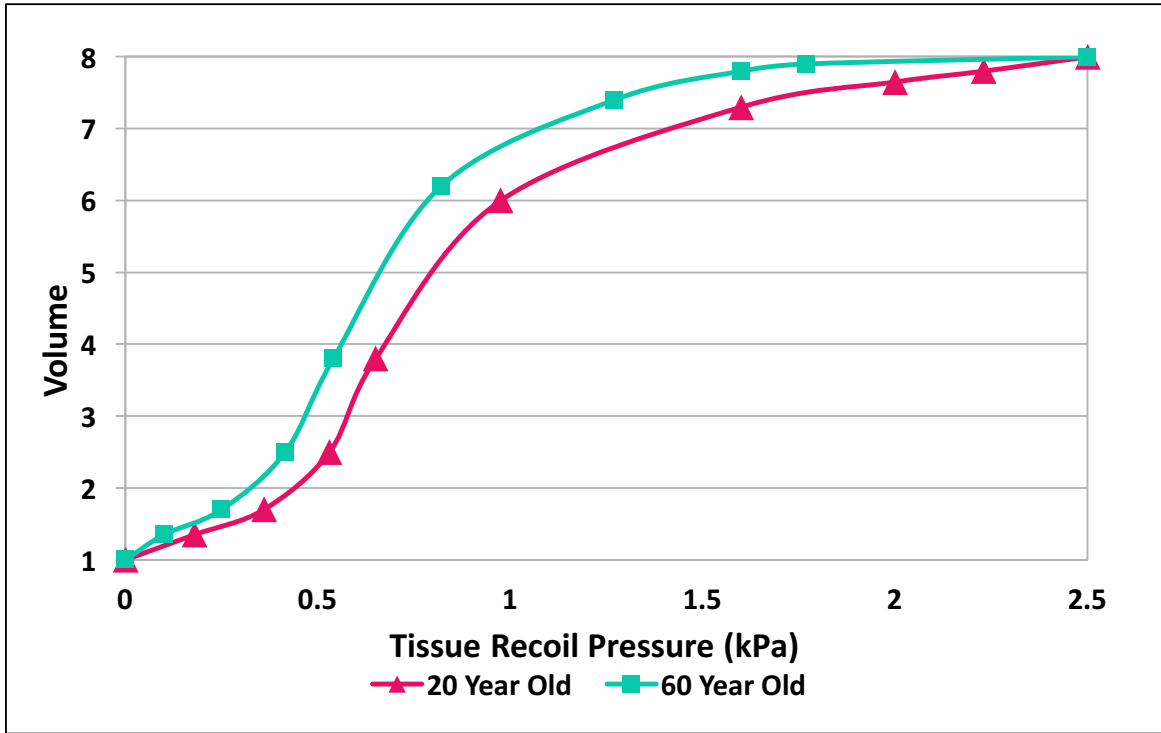
Table 4.3: Difference in mean density, pressure, and density gradient between experimental data and model simulations. Results are the means \pm S.D. across the four animals (for density and pressure), and the minimum calculated p-value (for t-test on imaging and model density gradients for four animals).

Volume	Difference in ρ (mean \pmS.D.) (g/cm³)	Difference in pressure (mean \pmS.D.) (cmH₂O)	Minimum p-value for density gradient
low	0.0106 \pm 0.0114	0.2 \pm 0.56	p>0.1773
med	0.0058 \pm 0.0093	1.2 \pm 0.54	p>0.1692
high	0.0019 \pm 0.0014	Approx. 0 \pm 0.41	p>0.1701

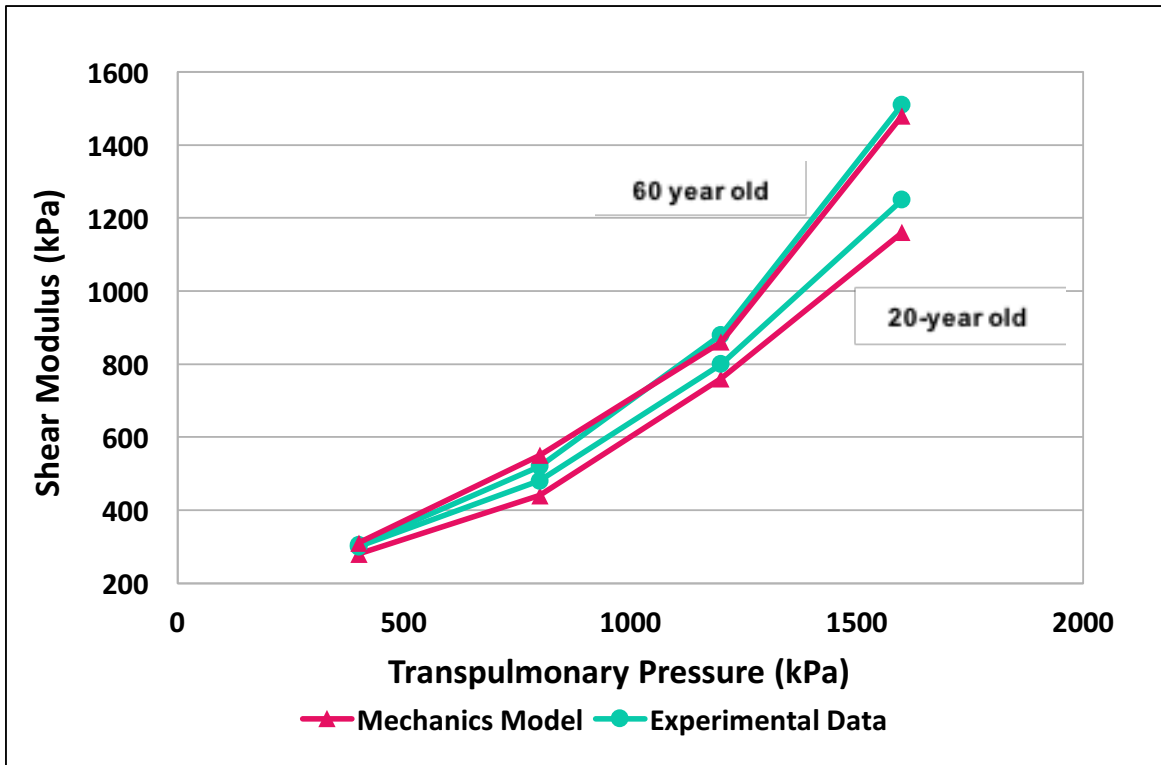
Figure 4.6 shows the effect of modifying the P-V relationship or G in an age-appropriate way on the gradient in tissue density with gravity at $V = 4xV_0$. P-V curves (Figure 4.6a) and G (Figure 4.6b) used as input for SEDF parameterization were selected for young (20 year old) and older (60 year old) lungs. Figure 4.6b includes comparison of G data with G computed from shear deformation in a tissue block, showing close comparison over a range of transpulmonary pressures.

Tissue density gradients for parameterization to each of the four combinations of P-V (20 or 60 years) and G (20 or 60 years) are given in Figure 4.6c. The rate of increase in density with distance from the dorsal surface was reduced (from the young case) by modifying either P-V or G, however the gradient was most sensitive to P-V. Using an SEDF parameterized to both P-V and G for the 60 year old data resulted in a decrease/increase in density of approximately $0.04\text{-}0.05 \text{ g/cm}^3$ in the most gravitationally dependent/non-dependent tissue.

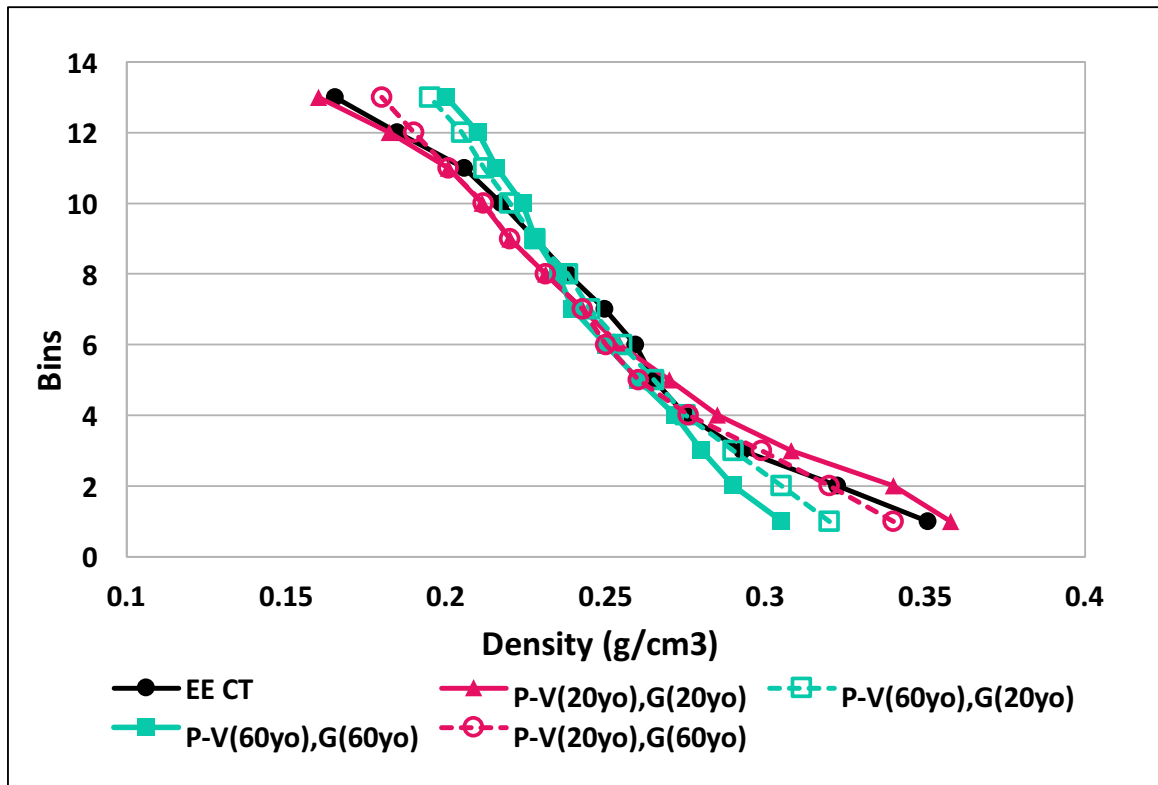
Table 4.4 shows the results of the sensitivity analysis performed to individually test each parameter. The stress change factors in Table 4.4 indicate the proportional change in stress (for each perturbed coefficient) relative to the average stress on the material surface at the end of isotropic expansion (using the original coefficients from Lee and Frankus). Note that this is the average of the two stresses from increasing and decreasing (in all cases increasing and decreasing produced similar proportional changes in stress). The results show that all the coefficients contribute to the stress-strain relationship of the material to varying degrees, with a_3 and c_3 being particularly dominant.



(a)



(b)



(c)

Figure 4.6: (This page and preceding). Model inputs to SEDF parameterization for ‘young’ and ‘old’ tissue, and tissue density distribution simulated at a single volume following parameterization. The top graph shows assumed P-V curves for a 20 and a 60 year old lung. The middle graph shows shear modulus at age 20, 40, and 60 years, with data from Lai-Fook (55) compared with model simulations. The bottom graph shows density distribution simulated for different combinations of G and P-V, where P-V(20yo),G(20yo) denotes P-V for a 20 year-old, and shear modulus for a 20 year-old. Results are shown for all four variations of young and old P-V and shear modulus compared with CT imaging.

Table 4.4: Stress change after isotropic expansion and uniaxial extension. The fractional changes in stress are the stresses for each coefficient, relative to the stress on the cube's surface after isotropic expansion.

Perturbed coefficient	Percentage change of coefficient	Stress change factor after isotropic expansion $(\sigma_{22} - \sigma_i)/\sigma_i$	Stress change factor after uniaxial extension σ_{22}/σ_k	Power of λ for coefficient
Original polynomial coefficients	0%	σ_i	± 3.59	
Polynomial:		σ_k		
a₁	$\pm 10\%$	± 0.18	± 2.80	2
a₂	$\pm 10\%$	± 0.12	± 3.12	4
a₃	$\pm 10\%$	± 0.21	± 3.27	6
a₄	$\pm 10\%$	± 0.15	± 2.38	8
b₁	$\pm 10\%$	± 0.16	± 3.02	4
b₂	$\pm 10\%$	± 0.18	± 2.85	8
c₁	$\pm 10\%$	± 0.16	± 3.11	6
c₂	$\pm 10\%$	± 0.21	± 2.63	6
c₃	$\pm 10\%$	± 0.11	± 3.66	8

Figure 4.7 shows the uniaxial stress-strain behaviour resulting from grouping the coefficients using the MATLAB Symbolic toolbox. When using only the coefficients of group 2 (coefficients a_3 , c_1 , and c_2), this does not result in a material that is physically realistic, as we can see from the negative stresses produced by uniaxial extension. So too is the result when using only group 4 (coefficient a_1) where an SEDF with one coefficient, as expected, does not behave like a physical material. In this case there is only a negligible negative stress which remains constant regardless of extension.

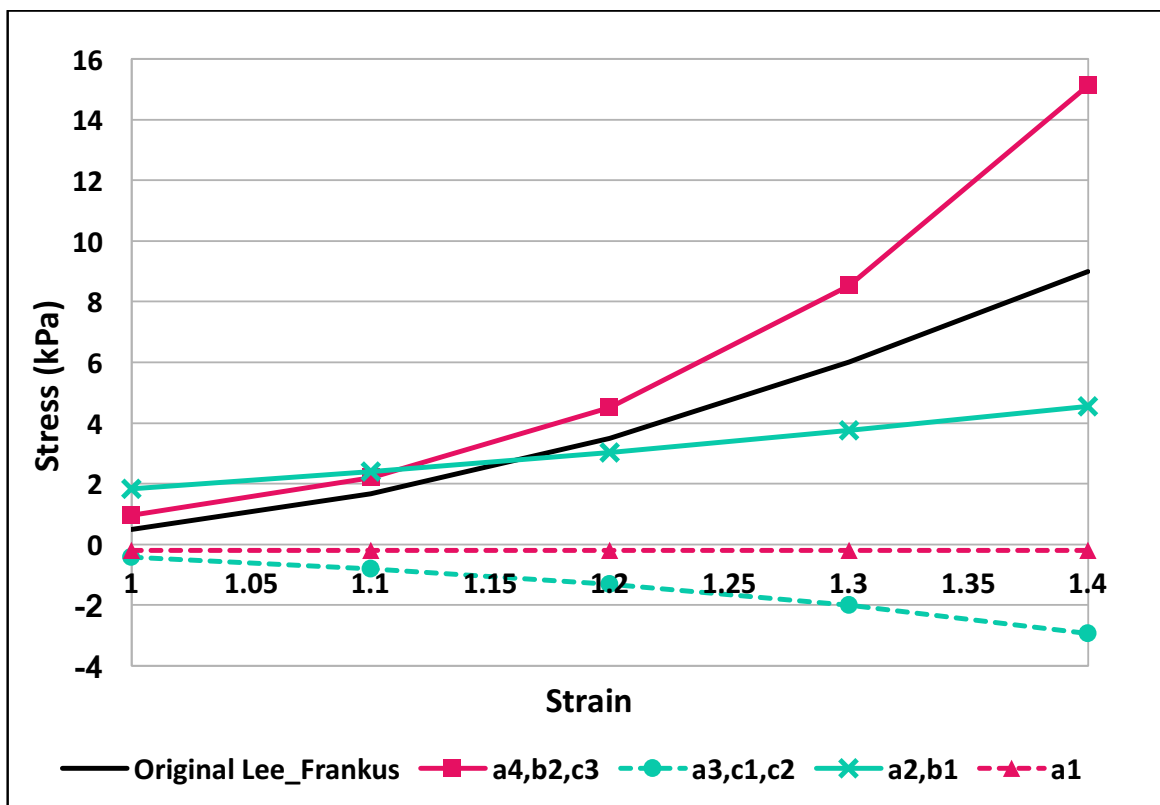


Figure 4.7: Model sensitivity tested by grouping of coefficients based on their power of lambda. Uniaxial extension was simulated using each group of coefficients in the SEDF, while setting the other coefficients to zero. Group 1: a_4 , b_2 , c_3 ; Group 2: a_3 , c_1 , c_2 ; Group 3: a_2 , b_1 ; Group 4: a_1 .

Groups 1 and 3 do produce reasonable stress-strain behaviours compared to the baseline curve (labelled Original Lee_Frankus), especially at extensions of up to 1.2. At larger extensions both the groups' behaviours diverge considerably from the baseline and no longer resemble the material that is being modelled.

4.4 Discussion

Acquiring accurate and robust data with which to parameterize a comprehensive stress-strain relationship for lung tissue remains an unresolved challenge. Therefore

- in the absence of a rigorous microstructure-based model for lung tissue mechanics
- there is still a current need for phenomenological models that can approximate the stress-strain behaviour of lung tissue (70).

The intention of this study was to determine whether minimal information that is readily measurable for the intact lung can be used to parameterize a phenomenological model for its material behaviour, using a general optimization process. We have demonstrated that a polynomial SEDF can be parameterized by optimizing its isotropic pressure-volume and shear behaviour to measured data; and that simulation of tissue displacement using the optimised SEDF provides good prediction of deformation under gravity loading for healthy young adult porcine lung. The study further shows that age-appropriate changes to shear modulus or the pressure-volume relationship can be included.

Predictive models for simulating lung tissue mechanics are used in a range of applications, including predicting the motion of lung tumours during radiation treatment (26, 70, 106) and as a component of integrative models that simulate complete respiratory function (102). For example, models for lung motion typically

use data from multiple imaged volumes or 4D-CT (computed tomography) to fit a distribution of local linear tissue elastic moduli that are specific to the patient, using image registration methods. However, because of radiation dose, 4D-CT is not routinely acquired in patients with other conditions, and the fitted elastic moduli are specific to the imaged volumes, posture, and respiratory status of the patient at the time of imaging.

In contrast, biophysically-based models seek to represent the mechanical behaviour of lung tissue such that any posture or lung volume can be simulated. Current published models of this type either rely on fitting a stress-strain relationship to excised tissue strip data (which provides a limited representation of the intact lung), or use simple assumptions for the expected relationship between lung volume and elastic recoil pressure (104). Alternative methods for prescribing a subject-specific material law would therefore be useful. Ideally such relationships would be established by understanding how lung tissue microstructure can be interpreted in the context of a continuum model. However this approach is limited by lack of experimental data that captures the microstructural behaviour of intact lung tissue, as well as the conclusion of modeling studies that the lung's behaviour on a macro-scale bears little resemblance to its micro-scale behaviour (23, 100).

In the current study we used P-V data acquired under controlled conditions in anaesthetized animals, supplemented with G data that characterizes the shear behaviour of the lung tissue at incremental recoil pressures. This data set is clearly limited to describing only gross tissue response; however, its advantage is that the data represents the mechanics of the intact lung, and acquisition of lung volume under static PEEP allows us to assume the values for P. The optimization method

could be applied to any other combination of experimental data, for example G could be replaced with uniaxial or biaxial tissue strip data. However, it is unlikely that data from such studies would be consistent with intact lung P-V. For example, tissue strip studies on animal and human lung tissue, e.g. (35, 43, 87, 97), are affected by distortion of the alveoli and disruption to the normal air-liquid interface. The stresses experienced by alveolar walls would be considerably different in the presence of normal concentrations of surfactant, whereas surfactant is lost once the tissue is treated prior to slicing.

The top graph in Figure 4.6 shows an inflection point near the closing volume. This detail is not seen in the experimental results, however we have chosen to include this feature simply to illustrate the model's capability in simulating changes to closing volume. This is possible due to the large number of coefficients in the strain energy function used, and can be removed if necessary. How airway closure can be included in a whole-lung mechanics model and how the closing volume changes with respect to age and BMI are issues that were not investigated in detail in this study. These would prove valuable investigations in future, and we simply show that our model can accommodate this.

It has been suggested that most pulmonary diseases result in altered lung tissue mechanics (99, 100), and this can occur via a range of mechanisms. Change in tissue mechanics can arise from a variety of pathological conditions such as abnormal surfactant production (2, 66, 85) or pulmonary fibrosis (123) which both increase total lung elastic recoil, and emphysema (39) which decreases lung elastic recoil. These pathological changes will also be reflected in change in local shear moduli. In addition to disease, the ageing lung also experiences changes in its

mechanical properties. The effects on the older lung caused by environmental factors such as air pollutants and cigarette smoke have been documented in a host of studies (3, 4, 47). However, several changes in lung structure and function are associated purely with the ageing process. Alveoli tend to become more 'shallow' (72) with a wider alveolar duct, resulting in a loss of surface area and capillary blood volume. There is also a loss in alveolar elastic recoil and a decrease in the strength of respiratory muscles. This can cause decreased driving pressure for airflow, and airway closure can occur far more readily in elderly lungs than in those of the younger population (5, 42). These changes may act singularly, but more likely in combination, to alter the mechanical properties of the respiratory system in the older individual, and consequently the pressure-volume characteristics of the individual. The current study shows preliminary results for including two of the typical measured changes to lung mechanics that accompany older age: a change in the pressure-volume curve, and increase in shear modulus. As we have noted, the intact lung pressure-volume relationship is due to the interaction of several mechanisms, however in our study we did not include airway closure or chest wall mechanics.

4.4.1 Study Limitations

This study used a single SEDF to describe the behaviour of the entire lung volume. The polynomial SEDF chosen for optimization used nine coefficients. While it is possible for the optimization to converge to a solution with fewer coefficients, the original number of coefficients was retained in order to avoid altering the interdependence of material parameter coefficients (the expression is also a legacy formulation and was therefore kept intact). In fact, the choice of SEDF is arbitrary, and it is theoretically possible to use any function.

Shear modulus data was used as input to the optimization. This is not readily available for the intact lung. Indentation testing (54, 55) requires access to whole, intact lungs that can be inflated and deflated repeatedly. In the case of Lai-Fook and Hyatt, this necessitated using cadaver lungs. Other microstructural data could be substituted for shear modulus, however as previously discussed, there are limitations on data from excised tissue.

By its nature, the model lumps together the contributions of tissue elasticity and surface tension into a single 'tissue system' elasticity. In reality, surface tension makes a distinguishable, dynamic contribution to lung mechanics. Fung (34) and Kowalczyk and Kleiber (53) showed how an exponential SEDF can be combined with mathematical expressions for the contribution of surface tension to total tissue system elasticity. This approach addresses the underlying mechanisms that contribute to lung mechanics and hysteresis, however it is not possible to acquire experimental data that would allow separate parameterization of the tissue and surface tension components of such a model. Related to this, the P-V data represents the deflation limb of the quasi-static P-V loop, and therefore does not address the hysteresivity seen between the inflation and deflation limbs. It is possible to model each limb individually, however both cannot be modeled using one SEDF parameterization.

The model's performance has only been validated through comparing the distribution of simulated tissue density against imaged distributions. More extensive validation could be performed by tracking the displacement of branching points in the airway or blood vessel trees (as material points) over several volumes. This remains as future work.

CHAPTER 5

CONCLUSIONS AND FUTURE WORK

Redistribution of elastic proteins away from the alveolar mouth in older age has been proposed to cause dilation of the alveolar duct and shallowing of the alveoli. We created duct/alveoli models reflecting young- and old-age morphometric geometries that enabled us to separate the effects of alveolar dilation and redistribution of proteins. Our results suggest that airspace enlargement alone could contribute to loss of tissue elastic recoil in the older lung. Tissue elastic recoil was also lower when the stiffness of the alveolar walls and mouths was the same, and increased as the stiffness of the wall and mouth differed (representing a change in the protein distribution). Our study supports that both the cause (redistribution of elastin and collagen) and the structural effect (alveolar airspace enlargement) contribute to decline in lung tissue elastic recoil in older age. The interactions of alveolar geometry, protein distribution, and surface tension form the key components of duct/alveolar micromechanics. In our model surface tension and protein distribution were combined into a single phenomenological 'material property'. Separating surface tension and protein interactions presents many challenges in 3D geometric modelling, and a model such as this has yet to be implemented successfully, to our knowledge. Developing a 3D alveolar model with configurable surface tension would provide a valuable addition to the field of alveolar mechanics.

To model whole-lung mechanics we used one strain energy density function that described the behaviour of the entire lung volume. We developed a framework whereby experimental data of different kinds can be used to parameterise a phenomenological model of whole-lung deformation. The framework is robust and configurable, and provides flexibility even in terms of the strain energy density function used for simulations. In the mechanics model, gravity was applied to the finite element mesh by treating the lung tissue as a continuous homogeneous material. Therefore, tissue heterogeneity was not treated as a localised phenomenon. This is an avenue for future development since increased heterogeneity is often considered to be an indicator of disease, and would certainly alter the mechanics of the tissue at an alveolar, as well as whole-organ, level. Including the phenomenon of heterogeneity would allow the investigation of restrictive pulmonary diseases such as idiopathic pulmonary fibrosis (IPF), as well as respiratory distress syndrome (RDS), cystic fibrosis, and emphysema, all of which are characterised by localised changes in parenchymal mechanical properties.

The lung undergoes changes to its tissue microstructure with age that are reflected in an age-related decline in most standard measurements of lung function. Studies based on thoracic CT agree that the normal older lung's appearance exhibits features that would be considered abnormal (and indicative of disease) if present in the younger adult lung. What has not been clear is whether there are subtle age-related changes to the CT appearance of the lung tissue that could be detected using quantitative methods. We trialled, for the first time on thoracic CT, image-analysis algorithms aimed at identifying these subtle changes. The techniques employed provided a level of sophistication that was not available in previously used statistical methods, in terms of identifying areas of non-homogeneous tissue

degradation. Our technique was able to classify young- and old-age CT images from healthy non-smokers with normal BMIs as 'healthy', suggesting that there are differences between what may be considered 'healthy' old age, and the subtle early signs of pathology. A useful extension of this study would be to conduct the same analysis on a larger cohort of subjects, once again including a range of ages and BMIs. A highly valuable subsequent study would be to conduct this analysis on patients for whom imaging is available at multiple time points, therefore at various stages of disease. This would provide the means to 'tune' the image analysis algorithms, and give the validation required to potentially develop the framework into a clinical tool.

REFERENCES

1. **Abaqus.** <http://www.3ds.com/products-services/simulia/products/abaqus/>.
2. **Adams FH, Towers B, Osher AB, Ikegami M, Fujiwara T, and Nozaki M.** Effects of tracheal instillation of natural surfactant in premature lambs. I. Clinical and autopsy findings. *Pediatric Research* 12: 841-848, 1978.
3. **Aga, Samoli, and Touloumi.** Short-term effects of ambient particles on mortality in the elderly: results from 28 cities in the APHEA2 project. *The European Respiratory Journal* 40: 28-33, 2003.
4. **Anderson HR AR, Bremner SA, Marston L.** Particulate air pollution and hospital admissions for cardiorespiratory diseases: are the elderly at greater risk? *The European Respiratory Journal* 40: 39-46, 2003.
5. **Anthonisen N, Danson J, Robertson P, and Ross W.** Airway closure as a function of age. *Respiration Physiology* 8: 58-65, 1969.
6. **Arias E. AR.** National Vital Statistics Reports. *National Center for Health Statistics* 2003.
7. **ATS.** An Official Research Policy Statement of the American Thoracic Society/European Respiratory Society: Standards for Quantitative Assessment of Lung Structure. <http://www.atsjournal.org/doi/pdf/10.1164/rccm.200809-1522ST>.
8. **Bar-Yishay E, Hyatt RE, and Rodarte JR.** Effect of heart weight on distribution of lung surface pressures in vertical dogs. *Journal of Applied Physiology* 61: 712-718, 1986.

9. **Bassingthwaighte J.** Physiological heterogeneity: fractals link determinism and randomness in structures and functions. *News Physiol Sci* 3: 5-10, 1988.
10. **Biring MS, Lewis, M. I., Liu, J. T., Mohsenifar, Z.** Pulmonary physiologic changes of morbid obesity. *The American Journal of the Medical Sciences* 318: 293, 1999.
11. **Bottai M, Pistelli, F., Di Pede, F., Carrozzi, L., Baldacci, S., Matteelli, G., Viegi, G.** Longitudinal changes of body mass index, spirometry and diffusion in a general population. *European Respiratory Journal* 20: 665-673, 2002.
12. **Brusasco V, R Crapo, and Viegi G.** Standardisation of the measurement of lung volumes. *ATS/ERS Task Force* 3: 511-522, 2005.
13. **Carey IM, Cook, D. G., & Strachan, D. P.** The effects of adiposity and weight change on forced expiratory volume decline in a longitudinal study of adults. *International Journal of Obesity and Related Metabolic Disorders* 23: 979-985, 1999.
14. **Caro CG, Butler, J., DuBois, A. B.** Some effects of restriction of chest cage expansion on pulmonary function in man: an experimental study. *Journal of Clinical Investigation* 39: 573, 1960.
15. **Chen Z-l, Song Y-l, Hu Z-y, Zhang S, and Chen Y-z.** An Estimation of Mechanical Stress on Alveolar Walls during Repetitive Alveolar Reopening and Closure. *Journal of Applied Physiology* jap. 00112.02015, 2015.
16. **Coates A.L. RP, D. Rodenstein, J. Stocks.** Measurement of lung volumes by plethysmography. *Eur Respir J*, 10: 1415–1427, 1997.
17. **Cook NR, Hebert, P. R., Satterfield, S., Taylor, J. O., Buring, J. E., Hennekens, C. H.** Height, lung function, and mortality from cardiovascular

- disease among the elderly. *American Journal of Epidemiology* 139: 1066-1076, 1994.
18. **Copley S, Stamatia, Volker, David, Wells, and Yang.** Effect of Aging on Lung Structure In Vivo: Assessment With Densitometric and Fractal Analysis of High-resolution Computed Tomography Data. *Journal of Thoracic Imaging* 27: 366-371, 2012.
 19. **D'Errico A, Scarani P, Colosimo E, Spina M, Grigioni WF, and Mancini AM.** Changes in the alveolar connective tissue of the ageing lung. *Virchows Archiv A* 415: 137-144, 1989.
 20. **Dale PJ, Matthews FL, and Schroter RC.** Finite element analysis of lung alveolus. *Journal of Biomechanics* 13: 865-873, 1980.
 21. **Denny E, and Schroter R.** A mathematical model for the morphology of the pulmonary acinus. *Journal of Biomechanical Engineering* 118: 210-215, 1996.
 22. **Denny E, and Schroter R.** The mechanical behavior of a mammalian lung alveolar duct model. *Journal of Biomechanical Engineering* 117: 254-261, 1995.
 23. **Denny E, and Schroter R.** A model of non-uniform lung parenchyma distortion. *Journal of Biomechanics* 39: 652-663, 2006.
 24. **Denny E, and Schroter R.** Relationships between alveolar size and fibre distribution in a mammalian lung alveolar duct model. *Journal of Biomechanical Engineering* 119: 289-297, 1997.
 25. **DuBois Arthur B. SYB, George N. Bedell, Robert Marshall, and Julius H. Comroe, Jr.** A rapid plethysmographic method for measuring thoracic gas volume: a comparison with a nitrogen washout method for measuring functional residual capacity in normal subjects. *J Clin Invest* 35: 322–326, 1956.

26. **Eom J, Xu XG, De S, and Shi C.** Predictive modeling of lung motion over the entire respiratory cycle using measured pressure-volume data, 4DCT images, and finite-element analysis. *Medical Physics* 37: 4389-4400, 2010.
27. **Faloutsos C.** Analytical results on the quadtree decomposition of arbitrary rectangles. *Pattern Recognition Letters* 13: 31–40, 1992.
28. **Fernandez J, Mithraratne P, Thrupp S, Tawhai M, and Hunter P.** Anatomically based geometric modelling of the musculo-skeletal system and other organs. *Biomechanics and Modeling in Mechanobiology* 2: 139-155, 2004.
29. **Formiguera X, Cantón, A.** Obesity: epidemiology and clinical aspects. *Best practice and Research clinical gastroenterology* 18: 1125-1146, 2004.
30. **Fowler RW.** Ageing and lung function. *Age and Ageing* 14: 209-215, 1985.
31. **Friedman GD, Klatsky, A. L., Siegelau, A. B.** Lung function and outcome of myocardial infarction. *The New England Journal of Medicine* 295: 1323-1323, 1976.
32. **Fryar CD, Gu Q, and Ogden CL.** Anthropometric reference data for children and adults: United States, 2007-2010. *Vital and health statistics Series 11, Data from the national health survey* 1-48, 2012.
33. **Fung Y-C.** A theory of elasticity of the lung. *Journal of Applied Mechanics* 41: 8-14, 1974.
34. **Fung Y.** Biomechanics: motion, flow, stress, and growth. 1990. Springer-Verlag, New York, 2000.
35. **Gao J, Huang W, and Yen R.** Mechanical properties of human lung parenchyma. *Biomedical Sciences Instrumentation* 42: 172-180, 2005.

36. **Gefen A, Elad D, and Shiner R.** Analysis of stress distribution in the alveolar septa of normal and simulated emphysematic lungs. *Journal of Biomechanics* 32: 891-897, 1999.
37. **Gevenois P-A, Scillia P, De Maertelaer V, Michils A, De Vuyst P, and Yernault JC.** The effects of age, sex, lung size, and hyperinflation on CT lung densitometry. *American Journal of Roentgenology* 167: 1169-1173, 1996.
38. **Glenny R, and Robertson T.** Fractal properties of pulmonary blood flow: characterization of spatial heterogeneity. *Journal of Applied Physiology* 69: 532–545, 1990.
39. **Greaves I, and Colebatch H.** Elastic behavior and structure of normal and emphysematous lungs post mortem. *The American Review of Respiratory Disease* 121: 127-136, 1980.
40. **Hoffman E, Clough, Christensen, Lin, McLennan, Reinhardt, Simon, Sonka, Tawhai, Beek v, and Wang.** The comprehensive imaging-based analysis of the lung: A forum for team science. *Academic Radiology* 11: 1370–1380, 2004.
41. **Hole DJ, Watt, G. C. M., Davey-Smith, G., Hart, C. L., Gillis, C. R., Hawthorne, V. M.** Impaired lung function and mortality risk in men and women: findings from the Renfrew and Paisley prospective population study. *Bmj* 313: 711-715, 1996.
42. **Holland J, Milic-Emili J, Macklem P, and Bates D.** Regional distribution of pulmonary ventilation and perfusion in elderly subjects. *Journal of Clinical Investigation* 47: 81, 1968.
43. **Hoppin F, Lee G, and Dawson S.** Properties of lung parenchyma in distortion. *Journal of Applied Physiology* 39: 742-751, 1975.

44. **Hosokawa M, Kurozumi, Matsushita, and Takeda.** Age-related changes in lung structure and function in the senescence-accelerated mouse (sam): Samp/1 as a new murine model of senile hyperinflation of lung. *American Journal of Respiratory and Critical Care Medicine* 149: 776–782, 1994.
45. **Hu S, EA Hoffman, and JM Reinhardt.** Automatic lung segmentation for accurate quantitation of volumetric X-ray CT images. *IEEE Trans Med Imag* 490-498, 2001.
46. **Huda W, Scalzetti EM, and Levin G.** Technique factors and image quality as functions of patient weight at abdominal CT 1. *Radiology* 217: 430-435, 2000.
47. **Jaakkola MS.** Environmental tobacco smoke and health in the elderly. *The European Respiratory Journal* 19: 172-181, 2002.
48. **Janssens.** Aging of the Respiratory System: Impacts on Pulmonary Function Tests. *Clinics in Chest Medicine* 26: 469-484, 2005.
49. **Janssens J, Pache, and Nicod L.** Physiological changes in respiratory function associated with ageing. *European Respiratory Journal* 13: 197-205, 1999.
50. **Janssens JP KK.** Pneumonia in the very old. *Lancet Infectious Diseases* 4: 112-124, 2004.
51. **Karakaplan A, Bieniek M, and Skalak R.** A mathematical model of lung parenchyma. *Journal of Biomechanical Engineering* 102: 124-136, 1980.
52. **Kerr JS, Shiu YY, and Riley DJ.** Strain specific respiratory air space enlargement in aged rats. *Experimental gerontology* 25: 563-574, 1990.
53. **Kowalczyk P, and Kleiber M.** Modelling and numerical analysis of stresses and strains in the human lung including tissue-gas interaction. *European Journal of Mechanics* 13: 367-393, 1994.

54. **Lai-Fook S. J. TAW, R. E. Hyatt , J. R. Rodarte.** Elastic constants of inflated lobes of dog lungs. *Journal of Applied Physiology* 40: 508-513, 1976.
55. **Lai-Fook SJ HR.** Effects of age on elastic moduli of human lungs. *Journal of Applied Physiology* 89: 163-168, 2000.
56. **Lalley PM.** The aging respiratory system: pulmonary structure, function and neural control. *Respiratory Physiology and Neurobiology* 187: 199–210, 2013.
57. **Lamb, and Gillooly.** Airspace size in lungs of lifelong non-smokers: effect of age and sex. *Thorax* 48: 1993.
58. **Lang MR, Fiaux, G. W., Gillooly, M., Stewart, J. A., Hulmes, D. J., Lamb, D.** . Collagen content of alveolar wall tissue in emphysematous and non-emphysematous lungs. *Thorax* 49: 319-326, 1994.
59. **Lean M, Lara, J., Hill, J. O.** Strategies for preventing obesity. *Bmj* 333: 959-962, 2006.
60. **Lee G, Tseng N, and Yuan Y.** Finite element modeling of lungs including interlobar fissures and the heart cavity. *Journal of Biomechanics* 16: 679-690, 1983.
61. **Lee GC, and Frankus A.** Elasticity properties of lung parenchyma derived from experimental distortion data. *Biophysical Journal* 15: 481-493, 1975.
62. **Lee YC, Clark AR, Fuld MK, Haynes S, Divekar AA, Hoffman EA, and Tawhai MH.** MDCT-based quantification of porcine pulmonary arterial morphometry and self-similarity of arterial branching geometry. *Journal of Applied Physiology* 114: 1191-1201, 2013.
63. **Levitzky MG.** Pulmonary Physiology. *McGraw-Hill Companies* 2007.

64. **Li B, Christensen G, Hoffman E, McLennan G, and Reinhardt J.** Establishing a Normative Atlas of the Human Lung: Intersubject Warping and Registration of Volumetric CT Images. *Academic Radiology* 10: 255-265, 2003.
65. **Martin, Macklem G, Bode, and Dosman.** Age and sex differences in lung elasticity, and in closing capacity in nonsmokers. *Journal of Applied Physiology* 41: 129–135, 1976.
66. **Massaro D, Clerch L, Temple D, and Baier H.** Surfactant deficiency in rats without a decreased amount of extracellular surfactant. *Journal of Clinical Investigation* 71: 1536, 1983.
67. **Mazumder P.** Planar decomposition for quadtree data structure. *Computer Vision, Graphics, and Image Processing* 38: 258–274, 1987.
68. **McCabe L, Petsonk E, Hankinson J, Banks D, and Wang M.** Weight gain and longitudinal changes in lung function in steel workers. *CHEST Journal* 111: 1526–1532, 1997.
69. **McClellan KM, Kee, F., Young, I. S., & Elborn, J. S.** Obesity and the lung: 1. Epidemiology. *Thorax* 63: 649-654, 2008.
70. **McClelland JR, Hawkes DJ, Schaeffter T, and King AP.** Respiratory motion models: a review. *Medical Image Analysis* 17: 19-42, 2013.
71. **Mercer RR, and Crapo J.** Spatial distribution of collagen and elastin fibers in the lungs. *Journal of Applied Physiology* 69: 756-765, 1990.
72. **Mertens I, Clement J, Lauweryns J, Van de Woestijne K, Verbeken E, and Cauberghe M.** The senile lung. comparison with normal and emphysematous lungs. 1. structural aspects. *CHEST Journal* 101: 793–799, 1992.

73. **Mertens I, Clement J, Lauweryns J, Van de Woestijne K, Verbeken E, and Cauberghe M.** The senile lung. comparison with normal and emphysematous lungs. 2. functional aspects. *CHEST Journal* 101: 800–809, 1992.
74. **Mizuuchi T, Kida K, and Fujino Y.** Morphological studies of growth and aging in the lungs of Fischer 344 male rats. *Experimental gerontology* 29: 553-567, 1994.
75. **Modica MJ, Kanal KM, and Gunn ML.** The obese emergency patient: imaging challenges and solutions. *Radiographics* 31: 811-823, 2011.
76. **Moliva JI, Rajaram MV, Sidiki S, Sasindran SJ, Guirado E, Pan XJ, Wang S-H, Ross Jr P, Lafuse WP, and Schlesinger LS.** Molecular composition of the alveolar lining fluid in the aging lung. *Age* 36: 1187-1199, 2014.
77. **Morgan WKC, Reger, R. B.** Rise and fall of the FEV1. *CHEST Journal* 118: 1639-1644, 2000.
78. **Naimark A, Cherniack, R. M.** Compliance of the respiratory system and its components in health and obesity. *Journal of Applied Physiology* 15: 377-382, 1960.
79. **Neas LM, Schwartz, J.** Pulmonary function levels as predictors of mortality in a national sample of US adults. *American Journal of Epidemiology* 147: 1011-1018, 1998.
80. **Niewoehner DE, Kleinerman J, and Liotta L.** Elastic behavior of postmortem human lungs: effects of aging and mild emphysema. *Journal of Applied Physiology* 39: 943-949, 1975.
81. **Oelsner EC, Carr JJ, Enright PL, Hoffman EA, Folsom AR, Kawut SM, Kronmal RA, Lederer DJ, Lima JA, and Lovasi GS.** Per cent emphysema is

associated with respiratory and lung cancer mortality in the general population: a cohort study. *Thorax* thoraxjnl-2015-207822, 2016.

82. **Olsson DM, and Nelson LS.** The Nelder-Mead simplex procedure for function minimization. *Technometrics* 17: 45-51, 1975.
83. **Organisation WH.** *World Health Report 2004* 2004.
84. **Petersson J, Rohdin M, Sánchez-Crespo A, Nyrén S, Jacobsson H, Larsson SA, Lindahl SG, Linnarsson D, Neradilek B, and Polissar NL.** Posture primarily affects lung tissue distribution with minor effect on blood flow and ventilation. *Respiratory physiology & neurobiology* 156: 293-303, 2007.
85. **Petty T, Silvers G, Paul G, and Stanford R.** Abnormalities in lung elastic properties and surfactant function in adult respiratory distress syndrome. *CHEST Journal* 75: 571-574, 1979.
86. **Prisk GK, Yamada K, Henderson AC, Arai TJ, Levin DL, Buxton RB, and Hopkins SR.** Pulmonary perfusion in the prone and supine postures in the normal human lung. *Journal of Applied Physiology* 103: 883-894, 2007.
87. **Rausch S, Martin C, Bornemann P, Uhlig S, and Wall W.** Material model of lung parenchyma based on living precision-cut lung slice testing. *Journal of the Mechanical Behavior of Biomedical Materials* 4: 583-592, 2011.
88. **Reeve AM, Nash MP, Taberner AJ, and Nielsen PM.** Constitutive Relations for Pressure-Driven Stiffening in Poroelastic Tissues. *Journal of Biomechanical Engineering* 136: 081011, 2014.
89. **Rennie D, Cormier Y, Dosman J, and Chen Y.** Waist circumference is associated with pulmonary function in normal-weight, overweight, and obese subjects. *The American Journal of Clinical Nutrition* 85: 35–39, 2007.

90. **Samet H.** The Quadtree and Related Hierarchical Data Structures. *ACM Computing Surveys (CSUR)* 16: 188-194, 1984.
91. **Schunemann HJ, Dorn, J., Grant, B. J., Winkelstein, W., Trevisan, M.** Pulmonary Function Is a Long-term Predictor of Mortality in the General Population 29-Year Follow-up of the Buffalo Health Study. *CHEST Journal* 118: 656-664, 2000.
92. **Simon DM, Tsai LW, Ingenito EP, Starcher BC, and Mariani TJ.** PPAR γ deficiency results in reduced lung elastic recoil and abnormalities in airspace distribution. *Respiratory Research* 11: 69, 2010.
93. **SolidWorks.** <http://www.solidworks.com/>.
94. **Stamenovic D.** Micromechanical foundations of pulmonary elasticity. *Physiol Rev* 70: 1117-1134, 1990.
95. **Subramaniam K, Hoffman E, and Tawhai M.** Quantifying Tissue Heterogeneity using Quadtree Decomposition. *Proc IEEE EMBC* 2012.
96. **Subramaniam K, Hoffman E, and Tawhai M.** Using CT imaging to quantify differences between young and elderly healthy lungs. In: *SPIE Medical Imaging* International Society for Optics and Photonics, 2013, p. 86720Z-86720Z-86726.
97. **Sugihara T, Martin C, and Hildebrandt J.** Length-tension properties of alveolar wall in man. *Journal of Applied Physiology* 30: 874-878, 1971.
98. **Suki B, and Bartolák-Suki E.** Biomechanics of the Aging Lung Parenchyma. In: *Mechanical Properties of Aging Soft Tissues* Springer, 2015, p. 95-133.
99. **Suki B, and Bates JH.** Extracellular matrix mechanics in lung parenchymal diseases. *Respiratory Physiology & Neurobiology* 163: 33-43, 2008.

100. **Suki B, and Bates JH.** Lung tissue mechanics as an emergent phenomenon. *Journal of Applied Physiology* 110: 1111-1118, 2011.
101. **Suki B, Ito S, Stamenović D, Lutchen KR, and Ingenito EP.** Biomechanics of the lung parenchyma: critical roles of collagen and mechanical forces. *Journal of Applied Physiology* 98: 1892-1899, 2005.
102. **Swan AJ, Clark AR, and Tawhai MH.** A computational model of the topographic distribution of ventilation in healthy human lungs. *Journal of Theoretical Biology* 300: 222-231, 2012.
103. **Tawhai M, Hoffman E, and Lin C.** The Lung Physiome: merging imaging-based measures with predictive computational models of structure and function. *Wiley Interdiscip Rev Syst Biol Med* 1: 61-72, 2009.
104. **Tawhai M, Nash M, Lin C-L, and Hoffman E.** Supine and prone differences in regional lung density and pleural pressure gradients in the human lung with constant shape. *Journal of Applied Physiology* 107: 912–920, 2009.
105. **Tawhai MH, et al.** CT-based geometry analysis and finite element models of the human and ovine bronchial tree. *Journal of Applied Physiology* 97: 2310-2321, 2004.
106. **Tehrani JN, Yang Y, Werner R, Lu W, Low D, Guo X, and Wang J.** Sensitivity of tumor motion simulation accuracy to lung biomechanical modeling approaches and parameters. *Physics in Medicine and Biology* 60: 8833, 2015.
107. **Thurlbeck WM.** The internal surface area of nonemphysematous lungs. *The American Review of Respiratory Disease* 95: 765-773, 1967.
108. **Todd D, Soth M, and Parameswaran K.** Altered respiratory physiology in obesity. *Canadian Respiratory Journal* 13: 203, 2006.

109. **Toshima M, Ohtani Y, and Ohtani O.** Three-dimensional architecture of elastin and collagen fiber networks in the human and rat lung. *Archives of Histology and Cytology* 67: 31-40, 2004.
110. **Tsutsumi M, Nakata H, Tsunenari T, Maeda H, Yokoyama M, and Nishimura Y.** Relationship between respiratory muscle strength and lean body mass in men with COPD. *CHEST Journal* 107: 1232–1236, 1995.
111. **Turner JM, Mead, J. E. R. E., & Wohl, M. E.** Elasticity of human lungs in relation to age. *Journal of Applied Physiology* 25: 664-671, 1968.
112. **Uejima Y, Teramoto K, Oka T, Orimo H, Teramoto S, and Fukuchi Y.** A novel model of senile lung: senescence-accelerated mouse (sam). *American Journal of Respiratory and Critical Care Medicine* 150: 238–244, 1994.
113. **Uppot RN, Sahani DV, Hahn PF, Gervais D, and Mueller PR.** Impact of obesity on medical imaging and image-guided intervention. *American Journal of Roentgenology* 188: 433-440, 2007.
114. **Venegas JG, Harris RS, and Simon BA.** A comprehensive equation for the pulmonary pressure-volume curve. *Journal of Applied Physiology* 84: 389-395, 1998.
115. **Wahba WM.** Influence of aging on lung function-clinical significance of changes from age twenty. *Anesthesia & Analgesia* 62: 764-776, 1983.
116. **Weibel ER.** *Morphometry of the human lung.* Springer, 1965.
117. **Well D, Meier J, and Mahne A.** Detection of age-related changes in thoracic structure and function by computed tomography, magnetic resonance imaging, and positron emission tomography. *Semin Nuclear Medicine* 103–119, 2007.

118. **Winter DH, Manzini M, Salge JM, Busse A, Jaluul O, Jacob Filho W, Mathias W, and Terra-Filho M.** Aging of the Lungs in Asymptomatic Lifelong Nonsmokers: Findings on HRCT. *Lung* 193: 283-290, 2015.
119. **Wohl, Turner, and Mead.** Elasticity of human lungs in relation to age. *Journal of Applied Physiology* 25: 664–671, 1968.
120. **Womack CJ, Harris, D. L., Katzel, L. I., Hagberg, J. M., Bleecker, E. R., Goldberg, A. P.** Weight loss, not aerobic exercise, improves pulmonary function in older obese men. *The Journals of Gerontology Series A* 55: M453-M457, 2000.
121. www.thoracic.org/adobe/lungvolume.pdf. Consensus statement on measurement of lung volumes in humans. *NHLBI Workshop* 2003.
122. **Yamamoto Y, Tanaka A, Kanamaru A, Tanaka S, Tsubone H, Atoji Y, and Suzuki Y.** Morphology of aging lung in F344/N rat: alveolar size, connective tissue, and smooth muscle cell markers. *The Anatomical Record Part A: Discoveries in Molecular, Cellular, and Evolutionary Biology* 272: 538-547, 2003.
123. **Yernault J, De Jonghe M, De Coster A, and Englert M.** Pulmonary mechanics in diffuse fibrosing alveolitis. *Bulletin de Physio-Pathologie Respiratoire* 11: 231-244, 1974.

Appendix A

Quantifying Tissue Heterogeneity using Quadtree Decomposition

K. Subramaniam¹, E.A. Hoffman², M.H. Tawhai¹,

1. Auckland Bioengineering Institute, University of Auckland, Auckland, New Zealand

2. Departments of Radiology and Bioengineering, University of Iowa, Iowa City, IA

Abstract— Volumetric computed tomography (CT) imaging provides a three-dimensional map of image intensities from which lung soft tissue density distribution can be estimated. The information gained from analyzing these images can prove valuable in diagnosis of conditions where lung tissue is damaged or has degenerated, and it is also necessary for modeling lung tissue mechanics. This paper presents a new technique for quantifying heterogeneity based on individual CT images, and investigates the heterogeneity of lung tissue in a group of healthy young subjects. It is intended that development of this technique leads to a standard model of classifying heterogeneity in lung tissue, while taking into account variables such as different imaging platforms and resolutions, and the position of the patient during imaging.

I. INTRODUCTION

Heterogeneity in lung tissue density and vascular perfusion have been suggested as early markers of lung disease [1]. However, the normal lung also exhibits significant heterogeneity hence separating physiology from pathophysiology is difficult. Several methods exist for quantifying pulmonary heterogeneity, however the values reported are dependent on image resolution, and they do not take into account the spatial distribution of heterogeneity [2, 3]. Here we consider an alternative method for quantifying heterogeneity that has the potential to resolve these issues. The method has not previously been applied to lungs.

The quadtree decomposition is a commonly used algorithm in computer science and image processing, for applications such as data partitioning and texture analysis [4]. The technique works in a 2-dimensional image-space by recursively partitioning an image into boxes until all the pixels in each box are considered similar, based on some comparison. The form of comparison used is often a test of homogeneity, such as testing whether all the pixels in a box fall into a given intensity range. If this condition is satisfied, the box is not decomposed any further. Fig. 1 illustrates a quadtree decomposition on a simple shape. We present a method for determining tissue heterogeneity in lung images using the quadtree decomposition algorithm (QTD), and discuss the challenges in developing a general model that can be used for characterizing heterogeneity.

II. METHODS

Volumetric multi-detector row computed tomography (MDCT) imaging of the lung was acquired from the University of Iowa Comprehensive Lung Imaging Centre (I-Clic), as part of the Human Lung Atlas initiative [5, 6].

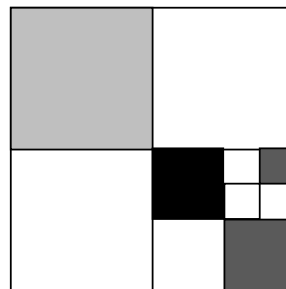


Fig. 1: A quadtree decomposition of a simple heterogeneous shape. 10 distinct boxes are formed.

Imaging of subjects for this study has been approved by the University of Iowa Institutional Review Board and Radiation Safety Committees. Imaging was acquired supine, from 8 healthy ‘normal’ subjects (4 male and 4 female), all under the age of 40. Imaging was acquired at end expiration (volume-controlled at 55 % vital capacity) and end inspiration (80 % vital capacity).

A. Lung Segmentation

For each subject, the lungs, major airways, and vessels were automatically segmented (Fig. 2b) using the custom-built software package PASS (Pulmonary Analysis Software Suite, University of Iowa) [6, 7].

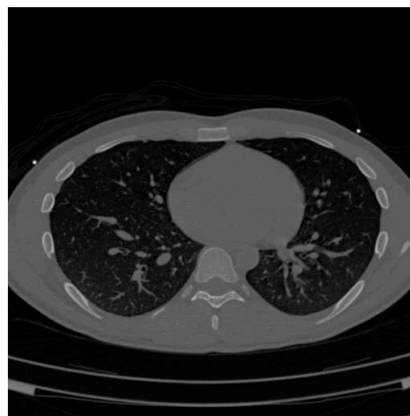


Fig. 2a: An original lung MDCT image

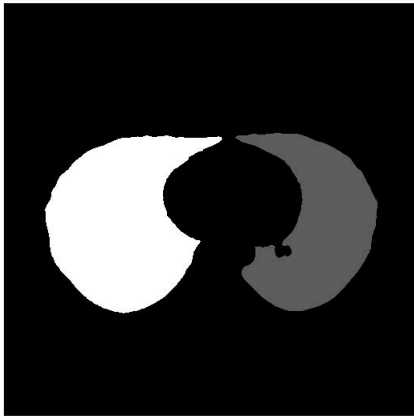


Fig. 2b: The segmented lung image's mask

The original DICOM images and resultant masks from segmentation were then loaded into MATLAB (version 2010a, The MathWorks Inc.). The masks were applied to the raw images and all non-lung data in the images was subtracted. An erosion filter was used to remove noise from the edges of the resultant lung tissue images. These images were then used as the basis for further analysis.

B. Heterogeneity Analysis

A new metric for lung tissue heterogeneity was calculated by selecting individual MDCT images and processing them with the QTD using MATLAB. Images were selected at locations along the cranial-caudal axis at positions of 25%, 50%, and 75% of the height of the lung (incrementing from cranial to caudal) (Fig. 3).

The pixel intensity values in a typical lung image correspond to density in Hounsfield units (HU), with values of approximately -1000 (for air density) and zero (for water density) [7]. Blood, bone, and other tissue are calibrated to have intensities of 40 and above. The QTD was programmed to exclude regions of high pixel values corresponding to blood and tissue, so as to avoid boxes being created due to edge effects between vessels and lung tissue. Box decomposition was performed based on the range of pixel intensities within a box, so that boxes were decomposed if the intensity range of a given box exceeded 100 (corresponding to approximately 10 % of the useful range of HU values present in an MDCT image). Fig. 4a shows a standard segmented lung image, and Fig. 4b illustrates its QTD result.

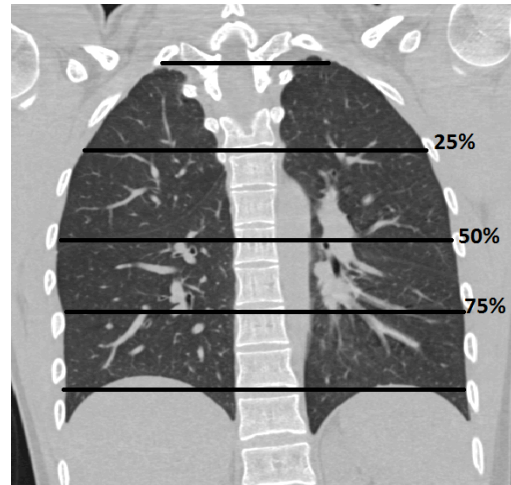


Fig. 3: Slices taken in the cranial-caudal axis for heterogeneity measurements

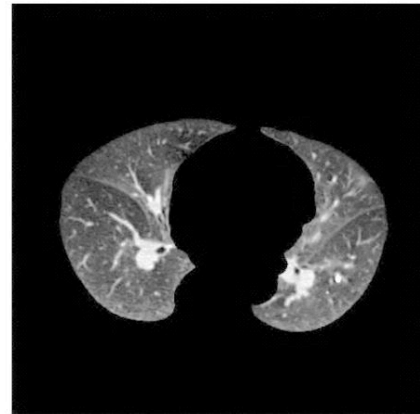


Fig. 4a: A masked lung MDCT image

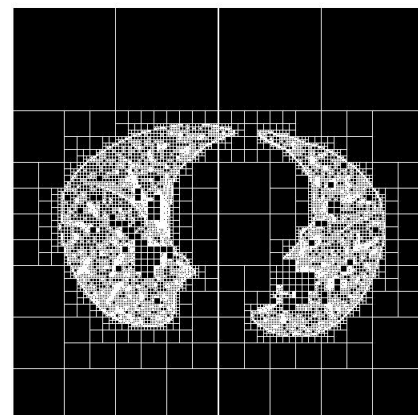


Fig. 4b: The lung image's Quadtree Decomposition

The number of boxes (N) created in this manner ranges from 10,000 to 20,000, so the boxes outside the lung tissue area need not be removed as the quantity is negligible. The total number of boxes was calculated from the QTD's resultant matrix, and this value was normalized by the lung's area. Area was calculated by summing the number of pixels in the lung image's footprint. The time taken for a single image to be processed by the QTD is 1 to 2 seconds. The initial heterogeneity metric is therefore $h_{QTD} = N/Area$.

We hypothesized that h_{QTD} would decrease with lung inflation. To test this hypothesis, heterogeneity was calculated using the QTDs for the three equally spaced images at end inspiration and end expiration. h_{QTD} values are plotted in Fig. 5, illustrating a reduction in heterogeneity from end expiration to end inspiration. A paired student's t -test performed for each subject on the mean values for the two volumes yields a p -value of 0.0001, indicating that h_{QTD} is statistically different for the two volumes, for each individual. An unpaired test between the groups yields a p -value of 0.0018, indicating that the means of the two groups are also statistically different, and the groups are distinct.

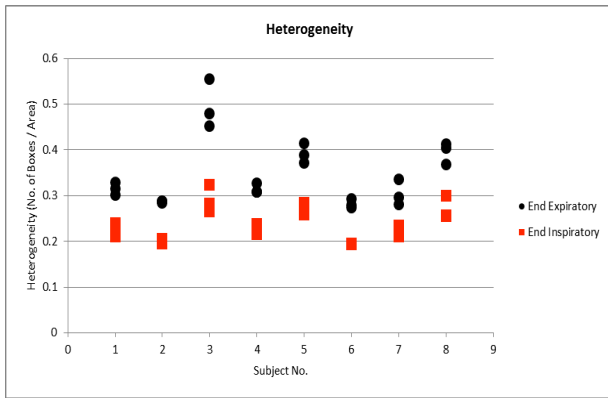


Fig. 5: Subject heterogeneities at end expiration and end inspiration.

C. Image Resolution Analysis

The heterogeneity values reported in Fig. 5 were calculated when the technique was performed on MDCT images of size 512x512, however different imaging modalities have different typical resolutions. For this algorithm to be used with other imaging methods, we therefore need to understand how resolution affects the calculated h_{QTD} . To simulate the effect of scaling an image to a different resolution, the 512x512 images were reduced to 256x256, 128x128, and 64x64 pixels, after which they were scaled up to 512x512 again, in order to produce a blurred image (presumably with lower heterogeneity). The resultant values for h_{QTD} are plotted against the sizes to which the 512x512 image was reduced in Fig. 6.

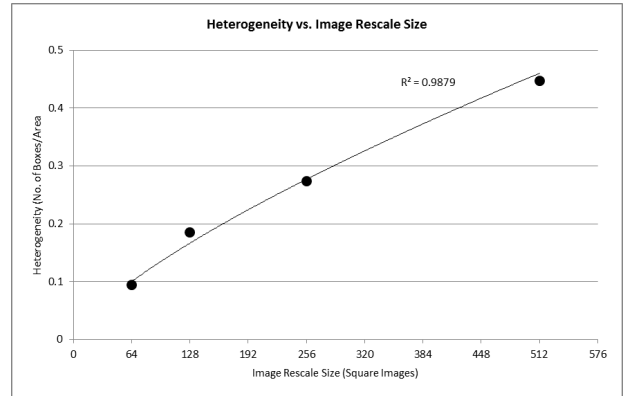


Fig. 6: Resultant heterogeneity of blurred images

C. Box Decomposition Parameters

The Quadtree technique was used with the condition that boxes were divided if the pixel intensity range was greater than 10% of the full intensity range of the image. Boxes were excluded from decomposition if the pixel intensity range within a box was less than 10% of the full intensity range, or the pixels had the high intensity values associated with blood/tissue only. To determine how the threshold influences the calculation of heterogeneity, the threshold was increased as a proportion of the full intensity range of the image, and plotted against the resultant h_{QTD} values. The characteristic curve of the results is shown in Fig. 7, illustrating the non-linear relationship between threshold parameters and heterogeneity.

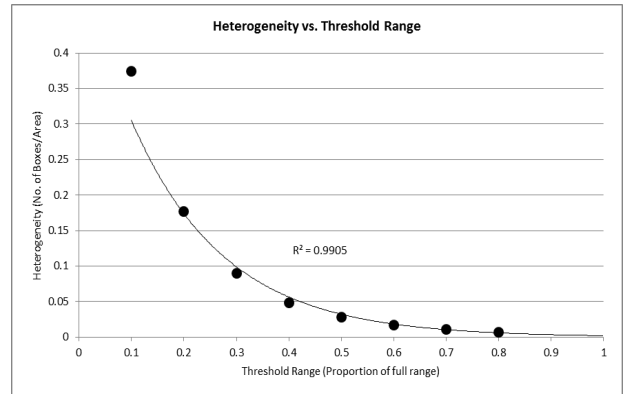


Fig. 7: Resultant heterogeneity values with different threshold bracket sizes

III. DISCUSSION

Quadtree decomposition appears to be a useful method for quantifying lung tissue density heterogeneity. This type of analysis has benefit over existing coefficient of variation or fractal-based methods because it explicitly accounts for the size of regions through which the tissue has similar density. This initial study has shown that end-inspiratory and end-expiratory heterogeneities can be distinguished from each other, across 8 subjects.

In order to make the current methodology more robust in its application across different imaging techniques, it would

be ideal to incorporate the effects of the threshold proportion and imaging resolution into the calculation of heterogeneity. Exactly how this should be done remains to be determined, however the approximately linear relationship between image resolution and heterogeneity (Fig. 6) provides reassurance that heterogeneity scales with image resolution in a reasonable and predictable manner. Furthermore, the relationship between heterogeneity and threshold follows a nonlinear relationship that could potentially be used to relate analyses of subjects that are performed using different threshold criteria.

We have not yet systematically addressed the manner in which heterogeneity changes throughout the lung volume. Although heterogeneity does vary within a lung slice, it has not yet been investigated whether there is a pattern of variation along any of the axes through the lung. The QTD is most likely to reveal differences in heterogeneity in the gravity-dependent axis, because of differences in the extent of tissue expansion due to gravitational deformation of the tissue.

ACKNOWLEDGMENT

This work was supported by NZ Ministry of Science and Technology grant 20959-NMTS-UOA.

REFERENCES

- [1] Sara K. Alford, E.J.R.v.B., Geoffrey McLennan, and Eric A. Hoffman, *Heterogeneity of pulmonary perfusion as a mechanistic image-based phenotype in emphysema susceptible smokers*. Proc Natl Acad Sci U S A., 2010. **107**(16): p. 7485–7490.
- [2] JB., B., *Physiological heterogeneity: fractals link determinism and randomness in structures and functions*. News Physiol Sci, 1988. **3**: p. 5-10.
- [3] Glenny RW, R.T., *Fractal properties of pulmonary blood flow: characterization of spatial heterogeneity*. J Appl Physiol, 1990. **69**: p. 532–545.
- [4] Samet, H., *The Quadtree and Related Hierarchical Data Structures*. ACM Computing Surveys (CSUR), 1984. **16**(2): p. 188-194.
- [5] Baojun Li, G.E.C., Eric A. Hoffman, Geoffrey McLennan, Joseph M. Reinhardt, *Establishing a Normative Atlas of the Human Lung: Intersubject Warping and Registration of Volumetric CT Images*. Academic Radiology, 2003. **10**(3): p. 255-265.
- [6] Eric A. Hoffman, P., Anne V. Clough, PhD, Gary E. Christensen, PhD, Ching-long Lin, PhD, Geoffrey McLennan, MD, PhD, Joseph M. Reinhardt, PhD, Brett A. Simon, MD, PhD, Milan Sonka, PhD, Merryn H. Tawhai, PhD, Edwin J.R. van Beek, MD, PhD, Ge Wang, PhD, *The comprehensive imaging-based analysis of the lung: A forum for team science*. Academic Radiology, 2004. **11**(12): p. 1370–1380.
- [7] S Hu, J.R., EA Hoffman, *Automatic lung segmentation for accurate quantitation of volumetric x-ray CT images*. IEEE Trans Med Imaging, 2001. **20**: p. 490–498.

Using CT imaging to quantify differences between young and elderly healthy lungs

K. Subramaniam^a, E.A. Hoffman^b, M.H. Tawhai^c,
^{a,c}Auckland Bioengineering Institute, University of Auckland, Auckland, New Zealand
^bDepartments of Radiology and Bioengineering, University of Iowa, Iowa City, IA

ABSTRACT

Volumetric computed tomography (CT) imaging provides a method of acquiring a 3-Dimensional view of lung soft tissue. The data captured in these images allows several methods of assessing the state of health of the lung. This information can prove valuable in early diagnosis of conditions where lung tissue is damaged, before external symptoms are expressed. The imaging data is also necessary for modeling lung tissue mechanics. This paper presents some analysis techniques for lung soft tissue, and uses these techniques to compare healthy lungs of young and elderly subjects.

Keywords: Volumetric CT, Lung Tissue, Elderly Care, Soft-Tissue

1. INTRODUCTION

A reduction in density and increased heterogeneity in lung soft tissue and vascular perfusion have been suggested as early markers of lung disease^[1]. However, the normal lung also exhibits significant changes in density associated with aging and obesity. Hence, separating expected physiological changes from pathophysiology is difficult. In general, a decrease in overall tissue density is suspected in the elderly lung, and microstructural changes that occur with age could reasonably be expected to increase tissue heterogeneity. In obese subjects, lung volume can be reduced due to the mass of the chest wall and abdomen, particularly in the supine position. This would directly affect the mean tissue density, and potentially the gravitationally-dependent density gradient due to operating at a lower lung volume. It would be useful to identify the differences between a lung exhibiting lung disease, and a lung that is healthy, but simply shows the expected changes arising from aging or excess body fat.

Here we examine lung tissue density distribution and heterogeneity^[2, 3]. Healthy lungs from young and elderly subjects are compared on the bases of age and BMI. Tissue density gradients are calculated directly from the CT images, while heterogeneity is calculated using a spatial quadtree decomposition algorithm^[4].

2. METHODS

Volumetric multi-detector row computed tomography (MDCT) imaging of the lung was acquired from the University of Iowa Comprehensive Lung Imaging Centre (I-Clic), as part of the Human Lung Atlas initiative^[5, 6].

Imaging of subjects for this study has been approved by the University of Iowa Institutional Review Board and Radiation Safety Committees. Imaging was acquired supine, from 16 healthy 'normal' subjects (8 male and 8 female). Half of the subjects (4 males and 4 females) were under the age of 30, while the other half were all over 60. Young and elderly subjects were paired according to gender and BMI (Body Mass Index). The range of BMI figures was between 21 and 32. Subjects were never-smokers, with normal lung function, and with no radiologically identified lung abnormalities. Imaging was acquired at end expiration (volume-controlled at 55 % vital capacity) and end inspiration (80 % vital capacity). Table 1 shows the relevant subject data. EE and EI denote End Expiratory and End Inspiratory, respectively, and density values are given in g/cm³. The eight subject pairs are numbered 1 to 8, and 1E and 1Y denote 'Subject 1 Elderly' and 'Subject 1 Young', respectively.

2.1 Lung Segmentation

For each subject, the lungs, major airways, and vessels were automatically segmented (Fig. 1) using the custom-built software package PASS (Pulmonary Analysis Software Suite, University of Iowa)^[6, 7].

The original DICOM images and resultant masks from segmentation were then loaded into MATLAB (version 2010a, The MathWorks Inc.), where the masks were applied to the raw images and all data in the images not considered to be soft tissue was subtracted. An erosion filter was used to remove noise from the edges of the resultant lung tissue images. A despeckling filter was also applied, after which the images were used in our analysis techniques.

Subject	Gender	BMI	Mean EE ρ	Mean EI ρ
1E	M	26	0.244	0.119
1Y	M	26	0.244	0.112
2E	F	22	0.179	0.116
2Y	F	22	0.256	0.117
3E	M	31	0.245	0.121
3Y	M	32	0.277	0.112
4E	M	32	0.216	0.114
4Y	M	31	0.246	0.116
5E	F	26	0.226	0.112
5Y	F	27	0.329	0.125
6E	F	21	0.192	0.120
6Y	F	21	0.219	0.102
7E	M	25	0.187	0.091
7Y	M	25	0.237	0.127
8E	F	32	0.236	0.129
8Y	F	31	0.259	0.123

Table 1. Young and Elderly subject pairs used in this study. EE denotes End Expiratory lung volume, and EI denotes End Inspiratory. Subjects with 'E' denote elderly, and subjects with 'Y' denote young.

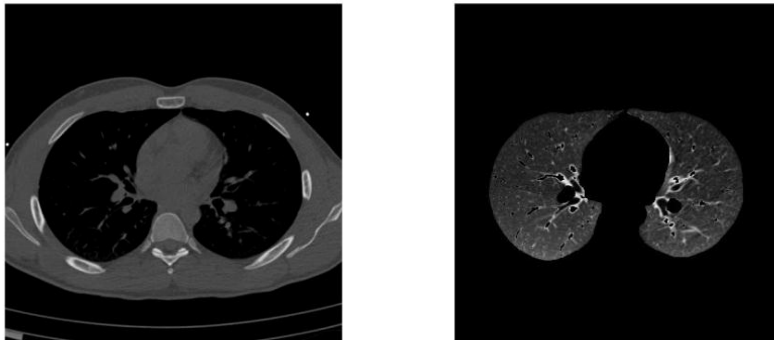


Figure 1. A raw lung MDCT image (left) and the segmented lung (right).

2.2 Density Analysis

The pixel intensity values in a typical CT image correspond linearly to the actual density of the imaged tissue. Density is measured in Hounsfield units (HU), with our segmentation software calibrated to values of approximately -1000 for air density, zero for water density^[7], and over 40 for blood, bone, and other non-parenchymal tissue.

Our density analysis seeks to create a profile of the lung tissue density. This was done using MATLAB. The average density for each slice is calculated, after which slices are grouped into bins, and the density of each bin plotted. Fig. 2 shows tissue density gradients for young and elderly subjects at both lung inflations. The axis presented here is the dorso-ventral axis. Since imaging is in the supine position, this is also the axis that is subject to gravity.

We hypothesized that the absolute densities of the elderly lungs would be lower in general than those of the younger subjects. Table 2 shows the mean densities for the young and elderly lungs, at both inflation volumes. Densities at EI were not statistically significantly different between the two groups ($p=0.7632$); however densities at EE did show a statistically significant difference ($p=0.0125$).

	Mean EE ρ	Mean EI ρ
Elderly Group	0.215	0.115
Young Group	0.258	0.117

Table 2. Mean densities for the Elderly and Young groups, at End Expiratory and End Inspiratory inflations, in g/cm^3 .

In Fig. 2 the young and elderly lung gradients are normalized by their respective means, showing that the density distributions within each group are qualitatively similar at both volumes. A paired Student's t-test performed on the plotted points, comparing the young and old subjects, yields a p-value of 0.8646 for the End Expiratory curves, indicating that they are not significantly different. For End Inspiratory, the p-value is 0.9205, indicating that these curves are also not significantly different.

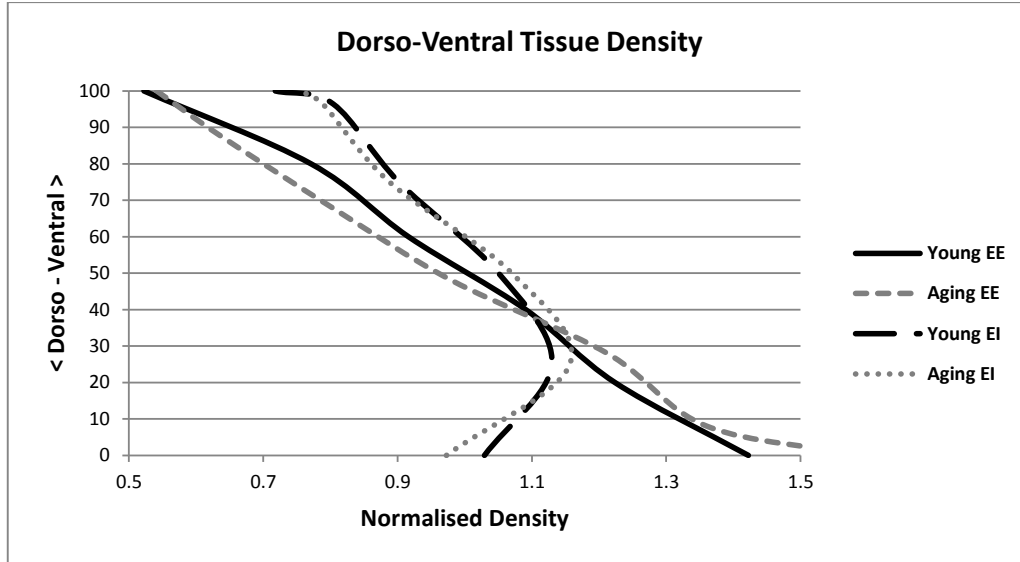


Figure 2. Density profile for young and elderly lungs in the dorso-ventral (gravity-dependent) axis.

2.3 Heterogeneity Analysis

To investigate heterogeneity of the soft tissue, we used a Quadtree Decomposition algorithm^[4]. The technique is commonly used in image processing and texture analysis^[8], and works by dividing an image into quarters, and then recursively partitioning the image into regions of similar pixel intensity. The algorithm was programmed to exclude regions of high pixel values corresponding to blood and tissue that may not have been removed in the masking process. This avoided boxes being created due to edge effects between vessels and lung tissue.

Images were selected at locations along the cranial-caudal axis at positions of 25%, 50%, and 75% of the height of the lungs. The Quadtree algorithm was then run on these images. Heterogeneity was calculated as the sum of the boxes created, divided by the area of the image occupied by soft tissue (the area of the segmentation mask).

We hypothesized that heterogeneity would increase with age at both lung volumes. To test this, heterogeneity was calculated for three slice locations along the cranial-caudal axis, and the mean of these three values plotted against age. Fig. 3 illustrates these results. R^2 values were calculated for each inflation volume. The R^2 values indicate that at both inflation volumes, there is no relationship between heterogeneity and age.

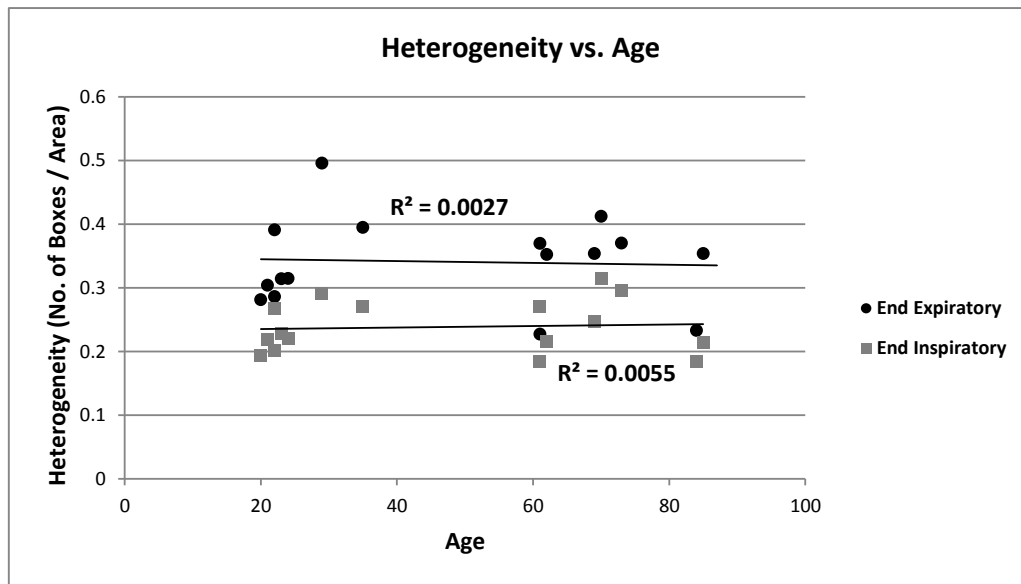


Figure 3: Heterogeneity correlation with age for End Expiratory and End Inspiratory.

We also hypothesized that heterogeneity would increase with BMI, regardless of age, for both lung inflation volumes. The mean heterogeneity values were plotted against BMI, and the results shown in Fig. 4. R^2 values were calculated once again for both inflation volumes, and indicate a stronger correlation between heterogeneity and BMI, than the correlation between heterogeneity and age.

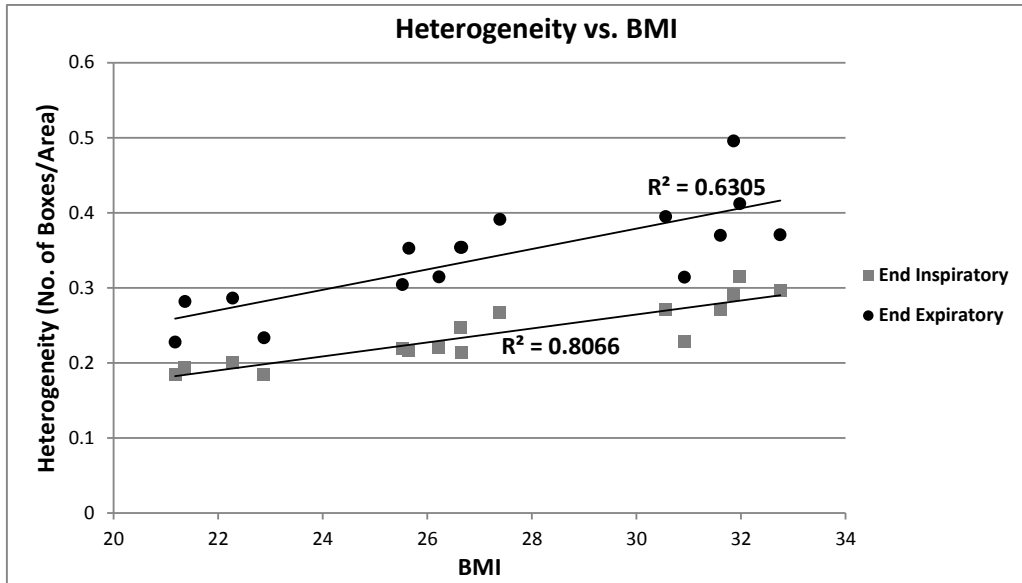


Figure 4: Heterogeneity correlation with BMI for End Expiratory and End Inspiratory.

3. DISCUSSION

The lung experiences loss of elastic recoil, increased airspace enlargement, and interstitial fibrosis with advancing age. These changes are most marked over the age of 50. We hypothesized that analysis of tissue density in normal, healthy, gender- and BMI-matched young (< 30 years) and older (> 60 years) subjects would reveal differences in gravitationally-dependent tissue gradient, and increased tissue heterogeneity in the older group. Our findings in these subjects are not consistent with either hypothesis. We also hypothesized that tissue heterogeneity would increase with BMI due to decreased lung volume. Our results demonstrate a linear relationship between density and BMI, for both age groups, and at two lung volumes.

Our older cohort had a lower mean lung density than the younger group. This was not statistically significant at the EI volume, but showed statistical significance at the EE volume. Previous studies have identified decreased mean lung attenuation with age^[9]. A difference between the current and previous studies is that we excluded subjects with any parenchymal abnormalities or respiratory symptoms, whereas previous studies have included more diverse subjects (often acquiring data from subjects imaged consecutively for routine clinical diagnosis). Our older cohort therefore might not be representative of the ‘typical’ older lung.

The quadtree analysis illustrates variation in heterogeneity of soft tissue density between subjects, but no significant variation between the old and young subjects. This finding is somewhat surprising considering that the older lung is considered to be characterized by microstructural changes (airspace enlargement, and interstitial fibrosis) that would imply increased parenchymal heterogeneity. This could again relate to our selection of an ‘abnormally normal’ cohort for the older subjects.

4. ACKNOWLEDGEMENTS

This work was supported by NZ Ministry of Science and Technology grant 20959-NMTS-UOA.

5. REFERENCES

- [1] Sara K. Alford, E.J.R.v.B., Geoffrey McLennan, and Eric A. Hoffman, *Heterogeneity of pulmonary perfusion as a mechanistic image-based phenotype in emphysema susceptible smokers*. Proc Natl Acad Sci U S A., 2010. **107**(16): p. 7485–7490.
- [2] JB., B., *Physiological heterogeneity: fractals link determinism and randomness in structures and functions*. News Physiol Sci, 1988. **3**: p. 5-10.
- [3] Glenny RW, R.T., *Fractal properties of pulmonary blood flow: characterization of spatial heterogeneity*. J Appl Physiol, 1990. **69**: p. 532–545.
- [4] Subramaniam, K., Eric A. Hoffman, M.H. Tawhai, *Quantifying Tissue Heterogeneity using Quadtree Decomposition*. Proc IEEE EMBC, 2012.
- [5] Baojun Li, G.E.C., Eric A. Hoffman, Geoffrey McLennan, Joseph M. Reinhardt, *Establishing a Normative Atlas of the Human Lung: Intersubject Warping and Registration of Volumetric CT Images*. Academic Radiology, 2003. **10**(3): p. 255-265.
- [6] Eric A. Hoffman, P., Anne V. Clough, PhD, Gary E. Christensen, PhD, Ching-long Lin, PhD, Geoffrey McLennan, MD, PhD, Joseph M. Reinhardt, PhD, Brett A. Simon, MD, PhD, Milan Sonka, PhD, Merryn H. Tawhai, PhD, Edwin J.R. van Beek, MD, PhD, Ge Wang, PhD, *The comprehensive imaging-based analysis of the lung: A forum for team science*. Academic Radiology, 2004. **11**(12): p. 1370–1380.
- [7] S Hu, J.R., EA Hoffman, *Automatic lung segmentation for accurate quantitation of volumetric x-ray CT images*. IEEE Trans Med Imaging, 2001. **20**: p. 490–498.
- [8] Samet, H., *The Quadtree and Related Hierarchical Data Structures*. ACM Computing Surveys (CSUR), 1984. **16**(2): p. 188-194.
- [9] Well DS, Meier JM, Mahne A, et al., *Detection of age-related changes in thoracic structure and function by computed tomography, magnetic resonance imaging, and positron emission tomography*. Semin Nucl Med. 2007. **37**: p. 103–119.

Appendix B

Work from this thesis has resulted in the following articles and presentations:

Journal papers:

The dependence of multiple metrics of lung tissue density on age and BMI

K. Subramaniam, A. R. Clark, E.A Hoffman, M.H. Tawhai

(Manuscript submitted to Journal of Applied Physiology)

Student's contribution: Design and conception of image analysis algorithms, research, analysis of images, data analysis, and written work resulting in paper.

Supervisors' contribution: Supervision, imaging, and feedback on paper writing.

Evidence for age-dependent air-space enlargement contributing to loss of lung tissue elastic recoil and increased shear modulus in older age

K. Subramaniam, H. Kumar, M.H. Tawhai

(Manuscript submitted to Journal of Applied Physiology)

Student's contribution: Design and conception of experimental work, development of models, simulation of models, data analysis, and written work resulting in paper.

Supervisors' and colleagues' contribution: Supervision for model development, feedback on paper writing.

The Impact of Age-Related Changes on Lung Mechanics: Linking Pressure-Volume and Parenchymal Properties to Tissue Deformation

K. Subramaniam, H. Kumar, A. Clark, E.A Hoffman, M.H. Tawhai

(Manuscript submitted to Journal of Biomechanics and Modeling in Mechanobiology)

Student's contribution: Design and conception of parameterization process, simulation, data analysis, and written work resulting in paper.

Supervisors' contribution: Imaging, and feedback on paper writing.

Conference papers:

Quantifying Tissue Heterogeneity using Quadtree Decomposition

K. Subramaniam, E.A. Hoffman, M.H. Tawhai

IEEE Engineering in Medicine and Biology Society, 2012

Using CT imaging to quantify differences between young and elderly healthy lungs

K. Subramaniam, E.A. Hoffman, M.H. Tawhai

SPIE Imaging Conference 2012

Conference posters:

Changes in Lung Tissue Density and Heterogeneity Arising from Aging and Obesity

Karthik Subramaniam, Eric Hoffman, Merryn Tawhai

American Thoracic Society, 2013

Developing Subject-Specific Lung Tissue Mechanics Models

Karthik Subramaniam, Hari Kumar, Eric Hoffman, Merryn Tawhai

American Thoracic Society, 2014

Co-authored papers:

Spatial redistribution of perfusion and gas exchange in patient-specific models of pulmonary embolism

MH Tawhai, AR Clark, ML Wilsher, DG Milne, K Subramaniam, KS Burrowes

9th IEEE International Symposium on Biomedical Imaging (ISBI), 2012

Appendix C

The dependence of multiple metrics of lung tissue density on age and BMI

K. Subramaniam¹, A. R. Clark¹, E.A Hoffman², M.H. Tawhai¹

¹Auckland Bioengineering Institute, University of Auckland, Auckland, New Zealand

²Departments of Radiology and Bioengineering, University of Iowa, Iowa City, IA

ABSTRACT

With advancing age, the lung experiences a reduction in elastic recoil and an increase in airspace enlargement and interstitial fibrosis. The relationship between these structural and functional changes in older age remains poorly defined. An objective quantitative analysis of computed tomography (CT) imaging was conducted to compare mean lung density (MLD), tissue density distributions, and tissue heterogeneity in subjects aged >60 years with gender- and BMI-matched subjects aged <30 years. Subjects were never-smoking, with no prior respiratory disease, and no radiologically-identified abnormalities on CT. Volume-controlled breath-hold imaging acquired at 80% vital capacity ('end inspiration') and 55% vital capacity ('end expiration') were used for analysis. MLD was not different between the age groups at end inspiration ($p=0.806$), but was larger in the younger group at end expiration (0.258 ± 0.033 vs. 0.216 ± 0.026 , $p=0.008$). Gravitational gradients of tissue density did not differ with age; the only difference in distribution of tissue density between the two age groups was a lower density in the apices of the older group at end expiration. The complexity of the lung tissue assessed using a fractal dimension and a Quadtree Decomposition showed no dependence on age, but both had strong relationships with BMI.

Keywords: heterogeneity analysis, lung densitometry, image processing, age differences

Evidence for age-dependent air-space enlargement contributing to loss of lung tissue elastic recoil and increased shear modulus in older age

K. Subramaniam, H. Kumar, M.H. Tawhai

Auckland Bioengineering Institute, University of Auckland, Auckland, New Zealand

ABSTRACT

As a normal part of mature ageing, lung tissue undergoes microstructural changes such as alveolar airspace enlargement and redistribution of collagen and elastin away from the alveolar duct. The older lung also experiences an associated decrease in tissue elastic recoil, but how this relates mechanistically to microstructural remodeling is not well understood. In this study we use a structure-based mechanics analysis to elucidate the contributions of age-related airspace enlargement and redistribution of elastin and collagen to loss of tissue elastic recoil. Our results show that age-related geometric changes can result in reduction of tissue elastic recoil and increase in shear and bulk moduli, consistent with published experimental data. All elastic moduli were sensitive to the distribution of stiffness (representing elastic fiber density) in the alveolar wall, with homogenous stiffness near the duct and through the septae resulting in a more compliant tissue. The preferential distribution of elastic proteins around the alveolar duct in the healthy young adult lung therefore provides for a more elastic tissue.

Keywords: Parenchymal tissue, Mechanics, Age, Alveoli

The Impact of Age-Related Changes on Lung Mechanics: Linking Pressure-Volume and Parenchymal Properties to Tissue Deformation

K. Subramaniam¹, H. Kumar¹, A. Clark¹, E.A Hoffman², M.H. Tawhai¹

¹*Auckland Bioengineering Institute, University of Auckland, Auckland, New Zealand*

²*Departments of Radiology and Bioengineering, University of Iowa, Iowa City, IA*

Abstract

Altered density and heterogeneity of lung soft tissue often accompany physiological changes. This may occur as a normal part of ageing, or may be an indicator of disease. In both scenarios the lung's mechanical behavior is affected. In the current study a double optimization method was used to fit coefficients in a strain energy density function as a phenomenological model for the stress-strain relationship of the intact porcine lung, using pressure-volume data from four pigs and supplemented with published pressure-dependent shear modulus data from humans. Finite deformation elasticity simulation of gravitational deformation of a finite element model for each of the four animals at three inflation pressures gave gravitationally-directed density gradients that matched density gradients measured on imaging. The study further shows that the shear modulus and tissue pressure-volume relationship can be modified independently to reflect age-dependent changes to the lung, and this impacts on the density gradient.

Keywords: Lung Tissue Mechanics, Optimization, Lung Model, Pulmonary Function Test

